



HAL
open science

Improvement of liquid clouds short-wave optical properties parameterization

Erfan Jahangir

► **To cite this version:**

Erfan Jahangir. Improvement of liquid clouds short-wave optical properties parameterization. Climatology. Université Paul Sabatier - Toulouse III, 2022. English. NNT : 2022TOU30107 . tel-03813598

HAL Id: tel-03813598

<https://theses.hal.science/tel-03813598v1>

Submitted on 13 Oct 2022

HAL is a multi-disciplinary open access archive for the deposit and dissemination of scientific research documents, whether they are published or not. The documents may come from teaching and research institutions in France or abroad, or from public or private research centers.

L'archive ouverte pluridisciplinaire **HAL**, est destinée au dépôt et à la diffusion de documents scientifiques de niveau recherche, publiés ou non, émanant des établissements d'enseignement et de recherche français ou étrangers, des laboratoires publics ou privés.



THÈSE

**En vue de l'obtention du
DOCTORAT DE L'UNIVERSITÉ DE TOULOUSE
Délivré par l'Université Toulouse 3 - Paul Sabatier**

**Présentée et soutenue par
Erfan JAHANGIR**

Le 14 avril 2022

**Amélioration de la paramétrisation des propriétés optiques des
nuages d'eau liquide dans le spectre solaire**

Ecole doctorale : **SDU2E - Sciences de l'Univers, de l'Environnement et de
l'Espace**

Spécialité : **Océan, Atmosphère, Climat**

Unité de recherche :
CNRM - Centre National de Recherches Météorologiques

Thèse dirigée par
Fleur COUVREUX et Quentin LIBOIS

Jury

M. Jean-Louis DUFRESNE, Rapporteur
M. KRISTIAN PAGH NIELSEN, Rapporteur
Mme Danahé PAQUIN-RICARD, Examinatrice
Mme Celine PLANCHE, Examinatrice
M. Benoit Vié, Examinateur
Mme Fleur COUVREUX, Directrice de thèse
M. Quentin LIBOIS, Co-directeur de thèse
M. Jean-pierre CHABOUREAU, Président

Amélioration de la paramétrisation des propriétés optiques des nuages d'eau liquide dans le spectre solaire

Improvement of liquid clouds short-wave optical properties parameterization

Résumé

Représenter correctement l'impact radiatif des nuages est un vrai défi pour les modèles atmosphériques, du fait que les interactions rayonnement-nuages sont contrôlées par les propriétés optiques des particules nuageuses. Ces propriétés dépendent de la taille des particules, et de la longueur d'onde du rayonnement, deux éléments qui ne sont pas bien résolus dans les modèles atmosphériques, si bien que les propriétés optiques doivent être paramétrisées. Dans ce manuscrit nous nous efforçons de quantifier les incertitudes sur l'impact radiatif des nuages dans le spectre solaire (SW) liées à la paramétrisation des propriétés optiques des nuages liquides. Les incertitudes proviennent en premier lieu de l'hypothèse faite sur la forme de la distribution de taille des gouttelettes (DSD), qui intervient dans: 1- l'estimation du rayon effectif des gouttelettes (r_{eff}) à partir du contenu en eau (LWC) et de la concentration en nombre des gouttelettes (N); 2- le calcul des propriétés de diffusion simple (SSPs) à partir de r_{eff} . Des incertitudes sont également liées au moyennage spectral nécessaire pour calculer les SSPs sur des bandes larges. Pour rendre compte de ces incertitudes, un nouveau jeu de paramétrisations des SSPs est développé et implémenté dans le code radiatif ecRad, couvrant un grand nombre de formes de DSD et de méthodes de moyennage spectral. Cette version améliorée d'ecRad est utilisée pour simuler les propriétés radiatives (transmittance, réflectance, absorption) d'une grande variété de nuages définis en termes de LWC et N , comprenant un nuage homogène idéalisé, des cas d'étude plus réalistes, et des sorties d'un modèle de climat. Ces simulations montrent que la transmittance/réflectance d'un nuage peut varier de 20 % en changeant simplement la forme de la DSD. Des différences de l'ordre de 20 % sont également obtenues pour les taux de chauffage atmosphérique. L'impact de la forme de la DSD sur l'estimation de r_{eff} contribue pour 80 % à l'incertitude totale, le reste étant lié à l'impact sur les SSPs. Le moyennage spectral a moins d'influence, si ce n'est sur l'absorption au sein du nuage. A l'échelle globale nous estimons que le forçage radiatif des nuages peut varier de 6 W m^{-2} selon la forme de DSD supposée, ce qui correspond à environ 13 % du forçage radiatif SW des nuages. Afin de compléter ces simulations de transfert radiatif hors-ligne, et d'étudier comment des différences de forçage radiatif se répercutent sur l'évolution des nuages, la version améliorée d'ecRad a été implémentée dans le modèle atmosphérique Mésos-NH. Par ailleurs, la forme de la DSD utilisée dans le code radiatif est rendue cohérente avec celle supposée dans le schéma microphysique à deux moments de Mésos-NH, LIMA. Des simulations 1D de stratocumulus sont réalisées en supposant différentes formes de DSD, à la fois dans LIMA et pour l'estimation de r_{eff} et des SSPs. L'impact direct de la DSD sur le forçage radiatif est évalué, et les effets indirects qui résultent des rétroactions du rayonnement sur les autres caractéristiques physiques sont également abordés. Dans ces simulations interactives, l'estimation de r_{eff} reste la principale source des différences, et les effets directs obtenus sont en accord avec les simulations hors-ligne. Au cours de la simulation les différences de flux radiatifs et de taux de réchauffement modifient progressivement les profils verticaux de température, de LWC et de N , ce qui entretient les différences liées à r_{eff} , puisqu'il dépend de ces quantités. Cette étude de cas souligne la complexité des interactions nuage-rayonnement, dont les processus physiques sous-jacents mériteraient d'être

étudiés plus en détail et pour d'autres cas. Enfin, ces simulations Mésos-NH mettent aussi en évidence la sensibilité aux propriétés optiques des nuages dans le LW, qui devraient à l'avenir être traitées avec autant d'attention que dans le SW.

Abstract

Simulating the radiative impact of clouds is challenging in atmospheric models, because cloud-radiation interactions are driven by the optical properties of individual cloud particles. These properties depend on the size of the particle and the frequency of light, two quantities not fully resolved in atmospheric models, implying that cloud optical properties need to be parameterized. In this thesis we focus on quantifying the uncertainties in shortwave (SW) cloud radiative impact due to the SW optical properties parameterization of liquid clouds. Uncertainties are first due to the Droplet Size Distribution (DSD) shape assumption required in two steps: 1- to estimate the cloud droplets effective radius (r_{eff}) from liquid water content (LWC) and droplet number concentration (N); 2- to compute the single scattering properties (SSPs) as a function of r_{eff} . Uncertainties also arise from averaging SSPs over wide spectral bands. To assess these uncertainties, a set of new parameterizations corresponding to various DSD shapes and spectral averaging methods are designed and implemented in the radiative code ecRad. Using this updated version of ecRad, we perform offline simulations to compute the bulk radiative properties (reflectance, transmittance, absorptance) of various clouds (defined in terms of LWC and N), including a homogeneous cloud, more realistic case studies, and outputs of a climate model. The results show that the transmittance/reflectance of the cloud can vary up to 20 % depending on the assumed DSD. Likewise, differences up to 20 % are obtained for atmospheric heating rates. The impact of the DSD shape assumption on r_{eff} (resp. SSPs) estimation contributes to around 80 % (resp. 20 %) of the total uncertainty. Spectral averaging is less an issue, except for atmospheric absorption. Overall, global shortwave cloud radiative effect can vary by 6 W m^{-2} depending on the assumed DSD shape, which is about 13 % of the best observational estimate. To complement these offline simulations and investigate how differences in radiative forcing feed back on cloud evolution, the updated version of ecRad is implemented in the atmospheric model Meso-NH. In addition, the DSD shape assumed in ecRad is made consistent with the DSD shape assumed in the 2-moment microphysics scheme of Meso-NH, LIMA. 1D simulations of a stratocumulus cloud are performed with various DSD shapes affecting simultaneously LIMA, the r_{eff} estimation and the SSPs parameterization. The direct impact of the DSD on the simulated radiative forcing is assessed, and the indirect effects that results from interactions of radiation with other components of the model are discussed as well. In these interactive simulations, the estimation of r_{eff} remains the main source of differences, and the obtained direct effects are in line with the offline simulations. Throughout the simulation, the differences in radiative fluxes and heating rates progressively impact the vertical profiles of temperature, LWC and N , enhancing the feedback since r_{eff} depends on these two quantities. This case study highlights the complexity of the cloud-radiation interactions, which deserve further investigation to fully understand the primary physical mechanisms at stake. Finally, these Meso-NH simulations point out the sensitivity to the LW cloud properties, that should in the future be treated as carefully as the SW.

Contents

Introduction Francaise	1
Introduction	1
1 Representing cloud-radiation interactions in atmospheric models	7
1.1 Droplet-scale interactions	7
1.1.1 Electromagnetic standpoint	7
1.1.2 Mie Theory	8
1.2 Cloud-scale interactions	9
1.2.1 From single to multiple scattering	9
1.2.2 Radiative transfer equation	10
1.3 Gas absorption and overlapping issue	12
1.3.1 Quantum standpoint in the light energy partition: Photons	12
1.3.2 Absorption computation in atmospheric models	13
1.3.3 Water vapor-Droplet absorption overlapping	14
2 Tools and models	17
2.1 Radiative codes	17
2.1.1 Two-stream method	17
2.1.2 Structure of ecRad radiative code	21
2.1.3 ARTDECO	24
2.2 Meso-NH model description	24
2.2.1 Turbulence scheme	25
2.2.2 Radiation scheme	25
2.2.3 Microphysics scheme	26
2.2.4 Communication between the radiation and microphysical schemes	28
3 Uncertainties in climate models due to the parameterization of liquid cloud optical properties	29
3.1 Introduction	29
3.2 Article:Uncertainty of SW Cloud Radiative Effect in Atmospheric Models Due to the Parameterization of Liquid Cloud Optical Properties	31
3.3 Supplementary material of the article	55
3.3.1 Impact of the discretization of the droplet size distribution for SSP computation	55
3.3.2 Curve Fitting validation	56
3.4 Discussion	57
3.4.1 Evaluation of two-stream and Spectral averaging methods	57
3.4.2 Sensitivity to the Number concentration	59

3.4.3	Sensitivity to spectral band resolution	60
3.5	Conclusion	63
4	Sensitivity of Meso-NH simulations to cloud optical properties	69
4.1	Introduction	69
4.2	FIRE stratocumulus case	69
4.3	1D Simulation Configurations	71
4.3.1	Common setup of the simulations	71
4.3.2	Varying part of the setups	71
4.4	Results	72
4.4.1	Impact on LW r_{eff} estimation excluded	72
4.4.2	Impact on LW r_{eff} estimation included	76
4.4.3	Perspective: Impact on microphysics activated	80
4.5	Conclusion	82
5	Conclusion and perspectives	87
	Bibliographie	95

List of Figures

1	The incoming solar radiation at the top of atmosphere and the fraction that reaches the surface. A graph copied from Kim et al. (2019).	2
2	The incoming solar radiation at the top of atmosphere and the fraction that reaches the surface. A graph copied from Kim et al. (2019).	2
1.1	Extinction efficiency calculated using Mie theory for three spherical particles with radii of 1, 10 and 50 μm . The Mie computations are performed for a range of size parameter ($2\pi r/\lambda$), where λ varies in the shortwave wavelength range of 0.2-4 μm	9
1.2	Schematic of incoming beams from the solid angle $d\Omega$ around Ω direction, and crossing the volume element of $dAdz$ of the atmosphere.	10
1.3	Absorption coefficient spectrum for the 1510-1520 cm^{-1} portion of the water vapor absorption band. a) Line-by-line absorption coefficients for a pressure of 10 mbar and temperature of 240 K. b) Ordered absorption coefficients of a) and frequency distributions function fitted on them. c) The inverse of cumulative distribution function or the k-distribution values of the absorption coefficient spectra of a . The figure is reproduced from Lacis and Oinas (1991)	14
1.4	The transmission of the AFGL atmosphere (explained in the text) with and without the cloud, the water vapor being the only present gas.	15
3.1	Figure adapted from Rockel et al. (1991) displaying in a) Mean optical depth (over the band 0.215-0.685 μm) versus LWP and in b) Mean single scattering albedo (on the band 1.273-3.58 μm) for clouds having effective radii in the range 0.18 – 24 μm and effective variance between 0.01 and 0.25. Stars,squares and triangles indicate values for N of 1, 100 and 500 cm^{-3} . The complete and dashed-lines in a represent the parameterizations of Rockel et al. (1991) and Stephens (1978) respectively.	30
3.2	Average SSPs on a Log DSD calculated using Mischenko (orange), and by the integrals used for this study (in blue) for the SW region using 10000 logarithmically spaced sub-intervals	55
3.3	Blue points show Q_{ext} averaged over a Log DSD with $\sigma=0.2$. Blue curves show the improved version of SOCRATES fit called 1-part fit. The green curve shows the two part fit results. Orange curves indicate the SOCRATES parameterization. All these elements are illustrated for the 9th band of ecRad in a and for 8th band in b and c	56
3.4	Optimum cut points against central wavelength of bands and threshold of 2 . . .	57
3.5	a)The transmittances calculated using two-stream (in red) and ARTDECO (blue) for 207 wavelengths in the SW range b)The spectral bias (curves and right side axis) and broad-band errors (horizontal bars and right side axis) of two-stream Transmittance relative to ARTDECO.	59

3.6 Errors of Transmittance/Reflectance obtained with different spectral averaging methods (illustrated with different geometrical shapes), relative to the reference ARTDECO values, for four clouds with optical thicknesses of 1, 5, 10 and 20, in the presence of an atmosphere. 60

3.7 From left to right: Transmitted flux for a Log DSD with $\sigma = 0.9$, the transmitted flux difference between $\sigma=0.9$ and $\sigma=0.2$, transmittance relative difference with respect to $\sigma=0.9$. The dashed lines in the two right figures indicate the isolines of the optical depth difference between $\sigma=0.9$ and $\sigma=0.2$. The Full (dashed) lines on the first left column, shows the contour of the optical-depth (effective radius) for simulations of $\sigma=0.9$ 61

3.8 The PDF shapes of two points Highlighted in Fig 3.7 61

3.9 The error of transmittance calculated with a)Thin averaging and b)Thick averaging methods relative to the reference transmittance mean on each spectral band for 20 different band arrangements. Dashed-line presents the absorption calculated on 280 wavelengths. Yellow bars on upper side of *a* denote the ecRad bands 62

3.10 For a cloud with optical thickness of 10 having log-normal DSD with $\sigma=0.35$ are shown in a)The transmittance and absorption computed for 280 wavelengths (called high resolution) in SW. The dashed vertical line indicates where $\frac{dT}{d(1-\omega)}=1$. b) The high-resolution transmittance versus absorption for a cloud of $\tau=30$ in green and $\tau=10$ in black line c)The mean reference (in red) and thin averaging-related (in blue) transmittances for two and 14 bands configurations (illustrated with complete and dashed lines respectively) d) Same as b with thin and thick averaged absorption for two bands configuration indicated in orange and blue vertical lines. In zoomed parcel, red, orange, and blue dashed horizontal lines represent the reference, the thick and thin averaging-related transmittances, respectively. 67

4.1 Observations for 13-14 July on San Nicolas Island. Upper panel: cloud height from ceilometer data and acoustic-sounder. Lower panel: solar irradiance from an Eppley pyranometer and cloud liquid-water path from a microwave radiometer. Figure reproduced from Albrecht et al. (1988). The orange shadow indicates the portion that will be simulated in this chapter. Time is in UTC. 70

4.2 Time series of vertical profiles of liquid mixing ratio, SW_{\downarrow} flux and potential temperature, for the simulation '*Consistent-LwOff*' and $\nu=1$ 73

4.3 The evolution of liquid water content, r_{eff} , downwelling SW radiation, heating rate and temperature differences between $\nu = 1$ and $\nu = 30$ profiles four 9 hours of the *consistent-LwOff* simulations. For all the figures the dashed and full lines indicate the profiles obtained for $\nu = 30$ and $\nu = 1$, respectively, and dotted lines indicate the difference between both values of ν 74

4.4 Same as 4.3, for the upper part of the cloud above 400 m. The last column shows the integrated optical depth from cloud top, and second column indicates the temperature differences between the clouds of two DSD shapes. 77

4.5 Same as 4.4, but for the lower part of the cloud below 400 m. 78

4.6 r_{eff} -LWC relation derived for 4 gamma distribution shapes: $\nu = 1, 5, 15, 30$, derived from Eq. 5. of the article 79

4.7 Difference between $\nu = 1$ and $\nu = 30$ for time-series of LWC, SW_{\downarrow} , and the potential temperature of *Consistent* and *Consistent-LwOff* setups. 79

4.8	Differences between $\nu = 1$ and $\nu = 30$ for time-series of LWP and surface SW_{\downarrow} of <i>Consistent</i> and <i>Consistent-LwOff</i> setups.	80
4.9	The profiles of LWC, r_{eff} , the number concentration, N , and the SW_{\downarrow} output from two simulations associated to $\nu = 1$ and $\nu = 30$ for <i>Consistent-LwOff</i> and <i>Consistent</i> setup extracted at 14:00	81
4.10	Difference between $\nu = 1$ and $\nu = 30$ for time-series of liquid mixing ratio, SW_{\downarrow} flux and potential temperature profiles, for ' <i>JustReff</i> ' setup	81
4.11	Same as 4.10 but for ' <i>JustSSP</i> ' Setup	82
4.12	Vertical profiles time-series of liquid mixing ratio, SW_{\downarrow} flux and potential temperature, for <i>sed</i> setup for all four values of the ν	83
4.13	Same as 4.12 but for <i>sed+rain</i> Setup	84

List of Tables

4.1 Different Configurations based on the choice of DSD shape in LIMA, SSPs and R_{eff} parameterizations 72

Introduction Française

Importance du rayonnement solaire

Le rayonnement solaire fournit l'énergie nécessaire à la plupart des processus physiques de la Terre. Il agit sur les processus de chimie atmosphérique, y compris les émissions biogéniques et le taux de photolyse qui, à leur tour, contrôlent la qualité de l'air et la décomposition des gaz à l'état de traces et la formation d'ozone ; Sukhodolov et al. (2016); Topaloglou et al. (2005). La quantité d'énergie solaire qui atteint la surface, appelée irradianance solaire de surface (ou flux radiatif ou rayonnement), revêt une grande importance pour les simulations de l'évolution du manteau neigeux (Vionnet et al., 2016; Quéno et al., 2020), la modélisation de la surface terrestre (Lapo et al., 2017) et la gestion des unités de production d'énergie solaire (Hanna et al., 2014). Les irradiances ascendantes et descendantes au sommet de l'atmosphère et à la surface de la Terre sont également primordiales pour dériver les bilans énergétiques à la surface et de l'atmosphère (Wild, 2020) et pour mieux comprendre la réponse de la Terre à un réchauffement climatique (Voigt et al., 2021). Le rayonnement solaire entrant peut contribuer au profil de chauffage diabatique et à la stabilité de l'atmosphère. De plus, une surface chauffée par rayonnement, fournit l'énergie nécessaire à la convection (élévation de la parcelle au voisinage de la surface du fait de sa flottabilité) et favorise la libération de chaleur latente et de vapeur d'eau dans la couche limite atmosphérique. Pour ces raisons, une mesure et une modélisation robustes de l'irradianance sont primordiales. Ce n'est cependant pas simple. Les interactions entre rayonnement et aérosols, nuages et gaz dans l'atmosphère compliquent le calcul et les observations de l'irradianance. Dans ce qui suit, nous présentons les observations et les modèles d'irradianance existants ainsi que les défis à relever.

Mesure de l'irradianance et importance des nuages

Il est pratiquement impossible que le rayonnement solaire qui pénètre dans l'atmosphère terrestre atteigne la surface sans avoir interagi. Son interaction avec les éléments atmosphériques varie en fonction de la longueur d'onde de la lumière. Dans cette thèse, nous nous concentrons sur la région des ondes courtes (SW) variant entre 0,2 et 4 μm . Dans des conditions sans nuage, la fraction ultraviolette (UV) et visible (VIS) du rayonnement solaire se situant dans la plage de longueur d'onde de 0,2 à 0,7 μm est principalement absorbée par l'ozone (O_3) et le dioxyde de carbone (CO_2) et la vapeur d'eau, tandis que la partie proche infrarouge (NIR) du SW correspondant aux rayons de longueur d'onde supérieure à 0,7 est principalement absorbée par la vapeur d'eau. La figure 2 compare le rayonnement entrant au sommet de l'atmosphère (qui correspond à l'émission du soleil en tant que corps noir de 6000°) et la partie qui arrive à la surface qui est la quantité que les instruments au sol mesurent.

Il existe de nombreuses méthodes de mesure de l'irradianance de surface, permettant des observations au sol, par satellite et aéroportées.

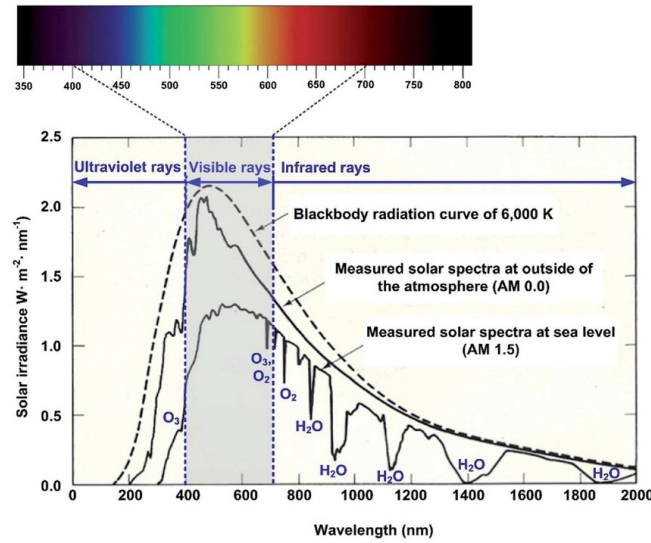


Figure 1: The incoming solar radiation at the top of atmosphere and the fraction that reaches the surface. A graph copied from Kim et al. (2019).

Les stations météorologiques locales de chaque pays ou région peuvent effectuer un certain nombre de mesures au sol. Cependant, nous nous référons ici à quelques exemples qui ont une couverture plus large et des réseaux robustes et fiables. Le Baseline Surface Radiation Network (BSRN), établi en 1988 par World Meteorological Organization (WMO), est maintenu par le World Radiation Monitoring Center (WRMC). Les 59 sites du BSRN, qui couvrent tous les continents et presque tous les océans, mesurent la partie solaire et infrarouge du spectre à la surface à l'aide de pyranomètres et de pyr géomètres, respectivement, avec une résolution d'une minute (pour plus de détails, voir Driemel et al. (2018)). En utilisant le même type d'instruments, le réseau de bilan radiatif de surface (SURFRAD), installé dans 6 régions climatiques différentes des États-Unis, fournit des flux à large bande descendants et montants SW et LW. Ces instruments sont généralement complétés par un ensemble d'autres équipements tels que le Total Sky Imager (TSI) pour cartographier les nuages ou un capteur quantique qui mesure la partie active photosynthétique dans le spectre solaire.

Avec le lancement de TIROS-1 au début des années 60 puis les projets MODIS et CERES en 2000, l'imagerie satellitaire ont permis des observations des flux radiatifs avec une couverture spatiale et temporelle continue qui fait défaut aux mesures de surface. Afin de dériver des produits d'irradiance de la surface, les données brutes des satellites doivent être traitées par des modèles de transfert radiatif (RTM), qui seront détaillés dans le chapitre 2, afin de tenir compte de l'interaction de la lumière avec les nuages, les aérosols et la vapeur d'eau. La précision des estimations satellitaires dépend du RTM utilisé et des caractéristiques et performances des instruments à bord du satellite. Les difficultés pour détecter les nuages multicouches et multiphases, le manque d'informations fiables sur les aérosols, les grandes incertitudes dans les cas où les nuages se trouvent au-dessus d'une couverture de neige/de glace (revue des méthodes satellitaires par (Huang et al., 2019)) sont quelques uns des problèmes liés aux méthodes indirectes de mesure du rayonnement solaire. Les observations par satellite ont également une résolution spatio-temporelle inférieure à celle des observations in-situ. Au contraire, les mesures aéroportées peuvent produire des observations à haute résolution mais avec une couverture spatiale inférieure à celle du satellite. Par exemple, le système SMART (Spectral Modular Airborne Radiation Measurement System) mesure l'irradiance spectral entre 0,3 et 2,3 μm avec un champ

de vision (FOV) de 2° en regardant au nadir (Krisna et al., 2018).

Pour les besoins de la modélisation du climat, l'irradiance ascendante et descendante au sommet de l'atmosphère doit également être mesurée afin d'en dériver les bilans énergétiques de la Terre. Une quantité qui aide à comprendre l'impact radiatif des nuages dans une région ou à l'échelle globale est l'effet radiatif des nuages (CRE), défini comme la différence nette des bilans radiatifs SW et LW entre les conditions de ciel nuageux et de ciel clair (Ramanathan et al., 1989). Les mesures de l'effet radiatif des nuages s'étendent de l'ancienne expérience du bilan radiatif de la Terre (ERBE) (Ramanathan et al., 1989) aux récentes mesures CERES de l'effet radiatif des nuages au niveau du sommet de l'atmosphère (EBAF) Loeb et al. (2018). Il est rapporté que les nuages exercent un effet de refroidissement net sur le bilan énergétique de la Terre. Cet effet peut être décomposé en $-47,7 \text{ W m}^{-2}$ dans le solaire au sommet de l'atmosphère (-56 W m^{-2} à la surface) et 28 W m^{-2} à la fois au sommet de l'atmosphère et à la surface dans le LW (Wild et al., 2019). Cela signifie que le CRE des nuages dans le Solaire représente environ 17% du rayonnement descendant au sommet de l'atmosphère.

Modélisation de l'irradiance dans les prévisions météorologiques et impact des nuages

Pour les prévisions d'irradiance à l'échelle de quelques heures, les méthodes statistiques basées sur les séries chronologiques sont utiles. Ces méthodes, basées sur des données historiques, dérivent une relation régressive pour prédire l'irradiance dans un futur proche. Les méthodes statistiques comprennent les approches linéaires telles que "Autoregressive moving average" (ARMA) ou les méthodes non linéaires comme les réseaux de neurones. Puisque le rayonnement est corrélé à l'existence des nuages, les modèles de mouvement des nuages (Cros et al., 2014) dérivés des images satellites peuvent être utilisés comme entrée des séries temporelles pour obtenir de meilleures simulations.

Pour la stabilité des réseaux électriques et de nombreuses autres applications telles que la prévision des inondations dans les bassins hydrologiques critiques dépendant de la fonte des neiges, les prévisions à un jour près sont primordiales. Pour les prévisions à des échelles de temps allant de 6h à plusieurs jours, on utilise des modèles de prévision numérique du temps. Ces modèles sont composés de grilles où les bilans d'énergie, de quantité de mouvement et de masse sont calculés en respectant leur conservation en utilisant la résolution des équations primitives. Les processus turbulents, microphysiques et radiatifs ne sont pas explicitement résolus et leurs effets sur les variables résolues du modèle sont représentés par des sous-modèles qu'on appelle paramétrisations. Dans cette thèse, la concentration est sur les paramétrisations dans le segment radiatif du modèle.

Malgré leurs capacités à prévoir un à plusieurs jours à l'avance, les modèles de PNT ne sont pas sans faille. De nombreuses études ont examiné le biais des prévisions d'irradiance des modèles de PNT évaluées grâce aux observations. Elles ont mis en évidence le rôle clé des nuages dans ces erreurs. En travaillant sur 9 modèles de prévisions numériques du temps et de projections climatiques Van Weverberg et al. (2018) ont montré que les erreurs d'irradiance sont corrélées avec l'évolution spatio-temporelle des nuages et que la contribution des nuages au biais d'irradiance dans le spectre solaire) la surface domine largement d'autres facteurs tels que les propriétés de surface ou la quantité de vapeur d'eau. L'évaluation des simulations d'irradiance du modèle AROME à 2,5 km de résolution sur les Alpes françaises montre un biais

positif dû à la sous-estimation de la couverture nuageuse, Vionnet et al. (2016). Cependant, même si les nuages sont bien prédits, le traitement des propriétés radiatives des nuages dans les modèles peut générer des erreurs. Tuononen et al. (2019) évalue la capacité du modèle IFS à prévoir l'irradiance au-dessus d'Helsinki. Ils ont trouvé de manière intéressante que même les cas de ciel couvert correctement prédits présentent un biais positif (8 W m^{-2}) associé à la sous-estimation de l'eau liquide intégrée (LWP) ou à la mauvaise représentation des propriétés optiques nuageuses. Compte tenu de ces résultats, il est important de présenter brièvement comment les propriétés radiatives des nuages sont calculées dans les modèles atmosphériques. Les nuages peuvent modifier considérablement le rayonnement solaire provenant du soleil en réfléchissant une fraction vers l'espace, en absorbant une partie et en laissant le reste être transmis à travers le nuage. Ces caractéristiques, appelées respectivement réflectance, absorbance et transmittance, sont connues comme les propriétés radiatives "bulk" des nuages. Les nuages émettent également un rayonnement aux longues longueurs d'onde comme un corps noir en fonction de leur température (selon la loi de Planck introduite en 1900). Dans chaque maille du modèle, le schéma radiatif calcule les propriétés radiatives "bulk" de la fraction de la maille occupée par les nuages (définie par la fraction nuageuse). Ce calcul est effectué en dérivant les propriétés optiques des gouttelettes (Slingo and Schrecker, 1982; Edwards and Slingo, 1996), en appliquant un ensemble d'hypothèses pour traiter l'hétérogénéité de l'eau liquide dans le nuage Tiedtke (1996) et le recouvrement vertical des nuages Hogan et al. (2016) et enfin fournissant toutes ces informations à un solveur d'équations de transfert radiatif (RTE).

Montornes et al. (2015) et Rontu and Lindfors (2018), utilisant respectivement les modèles WRF et HIRLAM-AROME NWP, montrent que pour des conditions atmosphériques similaires (y compris le même contenu intégré en eau liquide initial) avec un nuage couvert, le seul changement du schéma radiatif dans le spectre solaire aura un impact important sur la prévision d'irradiance et d'autres variables météorologiques telles que les profils de vitesse du vent. En retour, le rayonnement peut influencer les nuages de différentes manières. Selon Klinger et al. (2019), le refroidissement LW dans les cumulus peut améliorer les précipitations via la dynamique et la microphysique. D'un point de vue dynamique, il peut modifier la circulation et augmenter le taux de condensation, ce qui signifie convertir plus de vapeur d'eau en gouttelettes, par le biais de la microphysique, par le refroidissement thermique des particules qui re-circulent et arrivent au bord du nuage. Ce résultat a également été confirmé par de Lozar and Muesle (2016)). Le rayonnement dans le spectre solaire participe principalement au terme de chauffage diabatique. Le chauffage diabatique interagit dans les stratocumuli où la convection est faible Turner et al. (2018).

Irradiance dans les modèles climatiques et impact des nuages

Les modèles de circulation générale (GCM) utilisés pour la modélisation du climat partagent la même architecture que les modèles de PNT, bien qu'ils aient une résolution spatio-temporelle plus lâche. En conséquence, leurs défis en matière d'estimation de l'effet radiatif des nuages sont proches de ceux des modèles de PNT. Cependant, comme ils peuvent aller jusqu'à l'échelle temporelle des décennies, la réponse à l'erreur peut être différente. Une réponse reconnue du système terrestre au réchauffement climatique est le déplacement des cellules de Hadley et des courants-jets vers les pôles. Voigt et al. (2021) a souligné que les nuages sont les principaux contributeurs à cette tendance. Environ 70% de l'écart entre les modèles dans l'estimation de la sensibilité du climat (l'ajustement de la température de la Terre en réponse à un doublement

de la concentration de CO₂) est lié aux rétroactions des nuages (Vial et al., 2013). (Engström et al., 2014) attribue l'écart intermodèle au sommet de l'atmosphère à la variété des méthodes d'estimation de la fraction nuageuse. Le comportement des incertitudes peut varier en fonction du type de nuage. La sous-estimation de l'albédo du SW dans les stratocumuli brillants et la sous-prédiction des cumuli ayant un albédo surestimé sont des cas très connus. Ce dernier cas est appelé "too few too bright" problème (Nam et al., 2012). Comme l'indique Bony et al. (2006), les nuages liquides de la couche limite marine constituent la principale source d'incertitudes. En conséquence, Voigt et al. (2021) montre que les stratocumulus subtropicaux sont responsables de la plupart du schéma de rétroaction positive (méridionale) simulé par les GCMs (Zelinka et al., 2020). La couverture nuageuse, le contenu intégré en eau liquide, le rayon effectif et l'hétérogénéité sous-maille du condensat nuageux sont les raisons de ce manque de réflectivité dans le spectre solaire pour les stratocumulus (Ahlgrimm et al., 2018).

Objectif et structure de la thèse

Comme le soulignent la plupart des études mentionnées, les nuages ont une influence remarquable sur les erreurs d'estimation de l'irradiance dans les PNT et les incertitudes inter-modèles dans les modèles climatiques. De plus, on peut déduire que même si le profil des nuages est bien prédit par le modèle, le schéma radiatif du SW qui traite le rayonnement des nuages peut modifier de manière significative l'estimation de l'irradiance ou du flux radiatif. Parmi les éléments du schéma radiatif indiqués précédemment, nous nous concentrons sur la paramétrisation des propriétés optiques des particules de nuage.

L'accent est mis sur le SW, en raison du forçage radiatif important des nuages dans le SW, de sa plus grande sensibilité à la microphysique des nuages et aux hypothèses radiatives, et de sa plus grande contribution à l'écart entre les modèles par rapport à LW. En outre, nous ciblons les nuages liquides en raison de l'effet important de ce type de nuages sur la rétroaction climatique (Bony et al., 2006; Voigt et al., 2021). Une autre motivation est de combler le manque de littérature sur les propriétés optiques du SW liquide du nuage qui seront élucidées dans le chapitre 3 de la thèse.

La paramétrisation des propriétés optiques des nuages d'eau liquide dans les modèles atmosphériques comporte deux étapes : 1- L'estimation des propriétés de diffusion simple (SSPs). Les quantités qui sont responsables de l'interaction nuage-radiation à l'échelle microscopique, étant extrêmement variables en fonction de la taille de la particule et de la longueur d'onde de la lumière incidente. 2- Calcul du rayon effectif de la distribution de la taille des gouttelettes (DSD) à partir de la contenu en eau liquide (LWC) et de la concentration du nombre de gouttelettes (N). Deux quantités qui peuvent être dérivées du schéma microphysique du modèle. Il est à noter que des hypothèses distinctes sont faites sur la forme du DSD à travers chacune des étapes mentionnées. En outre, il existe plusieurs méthodes basées sur la littérature Hu and Stamnes (1993); Slingo and Schrecker (1982); Edwards and Slingo (1996); Manners (2015) pour faire la moyenne des propriétés optiques sur les bandes spectrales données par le modèle radiatif.

L'objectif principal de cette thèse est de quantifier les incertitudes dues au choix de la forme de la distribution de taille des gouttes et de la méthode de moyennage spectral des propriétés optiques sur le forçage radiatif des nuages dans le spectre solaire. Ceci est réalisé en 3 étapes principales qui définissent la présente thèse.

1. Une nouvelle paramétrisation des propriétés optiques est conçue qui prend en compte la

forme du DSD en plus de LWC et N . Elle contient également diverses méthodes de calcul de moyenne spectrale. Les paramétrisations ont été implémentées dans le code radiatif ecRad (Hogan and Bozzo, 2018). Par l'utilisation de cette nouvelle paramétrisation dans les simulations 1D d'ecRad hors ligne, sur un nuage idéal et 4 cas réels, nous démontrons les incertitudes sur le rayonnement transmis et réfléchi pour différentes valeurs de N et LWC (par conséquent pour différentes valeurs de rayon effectif et d'épaisseur optique). Le résultat de cette étude est détaillé au chapitre 3.

2. La version modifiée d'ecRad est implémentée dans le modèle de recherche de Météo-France, MesoNH. Un lien cohérent entre la microphysique et le rayonnement est établi, ce qui implique de communiquer les mêmes paramètres de forme de DSD appliqués dans la microphysique du modèle, au schéma radiatif. Cette cohérence n'existe pas dans la version actuelle de MesoNH et nous avons donc créé une nouvelle interface radiation-microphysique appropriée. Les outils pour créer les paramétrisations et les détails des codes radiatifs ecRad, ainsi que les outils utiles dans MesoNH, liés à notre thèse, sont documentés dans le premier et le deuxième chapitre.
3. réalisant des simulations 1D sur un cas connu de stratocumulus dans le MesoNH, l'objectif du chapitre 4 est de comprendre comment les incertitudes quantifiées dans le chapitre 3 se propagent temporellement et verticalement (puisque dans notre étude, seules des simulations 1D ont été effectuées) en interagissant avec d'autres composants de la simulation tels que la dynamique et la microphysique. L'impact des incertitudes de radiation sur les autres composantes du modèle à chaque pas de temps, sera reflété comme entrée dans le prochain appel au code radiatif. Ces simulations nous permettront d'étudier les éventuelles rétroactions.

Introduction

The importance of the SW irradiance

Solar radiation provides energy for most of the Earth physical processes. It takes part in atmospheric chemistry processes, including biogenic emissions and photolysis rate, which in turn control the air quality and decomposition of the trace gases and ozone formation (Sukhodolov et al., 2016; Topaloglou et al., 2005). The quantity of sunlight energy that reaches a surface area per time unit, known as surface solar irradiance (or radiative flux or radiation), is of great importance for snowpack evolution simulations (Vionnet et al., 2016; Quéno et al., 2020), land surface modeling (Lapo et al., 2017) and solar power units management (Hanna et al., 2014). The upwelling and downwelling irradiances at the top of the atmosphere (TOA) and the surface of the Earth are also primordial to derive the surface and atmosphere energetic budgets (Wild, 2020). The TOA irradiances are also crucial to better understanding Earth's response to a warming climate (Voigt et al., 2021). The incoming solar radiation can contribute to the diabatic heating profile and the atmosphere's stability. Moreover, a surface heated by radiation, supplies the energy for convection, the rise of the parcel at the vicinity of the surface, and enhances the release of latent heat and water vapor into the atmospheric boundary layer. For these reasons, robust measurement and modeling of irradiance are primordial. It is not straightforward, however. The radiative interactions between aerosols, clouds, and atmosphere gases complicate the irradiance computation and observations. In the following, we point out the existing observations and models of irradiance and the challenges.

Measurement of irradiance and the importance of cloud

It is almost impossible for the solar radiation that enters the Earth's atmosphere to reach the surface without being altered. The interaction of solar radiation with atmospheric elements depends on the wavelength. This thesis focuses on the shortwave region between 0.2-4 μm . In cloud-free conditions, the ultraviolet (UV) and visible (VIS) fraction of solar radiation lying within 0.2 to 0.7 μm range of wavelength is mainly absorbed by ozone (O_3), oxygen (O_2), and water vapor. In contrast, the near-infrared (NIR) portion of SW corresponding to rays with wavelengths greater than 0.7 is mainly absorbed by the water vapor. Figure 2 compares the incoming radiation at the top of the atmosphere (which corresponds to the emission of the sun as black body of 6000°) and the portion that arrives at the surface which is the quantity that the ground-based instruments measure.

Numerous methods exist for measuring surface irradiance, including ground-based, satellite, and airborne observations.

The local weather stations of each country or region can involve a quantity of ground-based measurements, including solar radiation measurements. Though here, we refer to some examples with broader coverage and robust and reliable networks. Baseline Surface Radiation

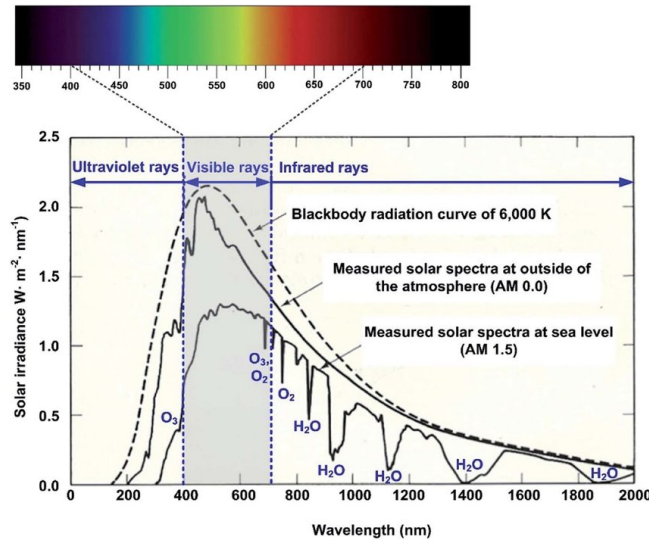


Figure 2: The incoming solar radiation at the top of atmosphere and the fraction that reaches the surface. A graph copied from Kim et al. (2019).

Network (BSRN), established in 1988 by World Meteorological Organization (WMO), is maintained by the World Radiation Monitoring Center (WRMC). The 59 sites of BSRN cover all continents and almost the oceans (the island-based measurements) and measure the SW and LW part of the surface using pyranometers and pyrometers, respectively, with 1-minute resolution (for more details, see Driemel et al. (2018)). Using the same kind of instruments, the Surface Radiation budget network (SURFRAD), installed in six various climate regions of the US, provides downwelling and upwelling broadband SW and LW fluxes. These instruments are generally complemented with a set of other equipment such as a Total Sky Imager (TSI) to monitor the clouds or a quantum sensor that measures the photosynthetic active part of the SW.

Emerging after the launch of TIROS-1 in the early 60s and progressing through the CERES and MODIS projects in 2000, satellite imagery enlightens new aspects of observations providing a continuous spatial and temporal cover lacking in surface-based measurements. In order to derive surface irradiance products, satellite raw data must be processed through Radiative Transfer Models (RTM), which will be detailed later in chapter 2, to take into account the interaction of light with clouds, aerosols, and gases (Letu et al., 2020). The accuracy of satellite estimations depends on the used RTM and the performance and characteristics of the instrument on board the satellite. Difficulties in detecting multilayer and multiphase clouds, lack of reliable aerosol information, and significant uncertainties in the cases where the clouds are over snow/ice cover (review of satellite methods by Huang et al. (2019)) are some issues related to indirect methods of solar radiation measurements.

Satellite observations also have a lower Spatio-temporal resolution than the in-situ observations. On the contrary airborne measurements can produce high-resolution observations but with lower spatial coverage than the satellite. For instance, Spectral Modular Airborne Radiation Measurement System (SMART) acquires spectral irradiance between 0.3 and 2.3 μm with a field of view (FOV) of 2° looking at nadir (Krisna et al., 2018).

These observations are used for various purposes. For the climate modeling studies, the top of atmosphere upwelling and downwelling irradiance must be measured to estimate the energetic budget of the Earth. A quantity that helps to understand the radiative impact of

clouds locally or globally is the cloud radiative effect (CRE), defined as the net radiative SW and LW budget difference between cloudy and clear sky conditions (Ramanathan et al., 1989). The measurements of CRE extend from the early Earth radiation budget experiment (ERBE) (Ramanathan et al., 1989) to the recent CERES-EBAF-TOA ¹ of CRE space-borne measurements (Loeb et al., 2018). It is reported that clouds exert a net cooling effect on the Earth’s energy budget. This can be decomposed into -47.7 W m^{-2} in the SW at TOA (-56 W m^{-2} at the surface) and 28 W m^{-2} at both TOA and at the surface in the LW (Wild et al., 2019). This means CRE in the SW is about 17% of the downwelling radiation at the TOA.

Irradiance modeling in Weather forecast and the impact of clouds

For the irradiance forecasts within the timescale of 6 hours, the statistical methods based on times series are helpful. Based on historical data, these methods derive a time series regressive relation to predicting the irradiance in the near future. Statistical methods include linear approaches such as Autoregressive moving average (ARMA) or nonlinear methods like artificial neural networks (Lauret et al., 2015; Diagne et al., 2013). Since the radiation is correlated to the existence of the clouds, the cloud motion patterns (Cros et al., 2014) derived from satellite images can be used as input of time series to achieve better simulations.

For the stability of power grids and numerous other applications such as flood prediction in critical snow-melt-dependent hydrological basins, one-day ahead predictions are primordial. For the forecasts with timescales from 6h to several days, Numerical weather prediction (NWP) models are used. NWPs are composed of the grids where the energy, momentum and mass budgets are calculated respecting the conservation of each component. The subgrid variability of turbulence, microphysics, and radiation processes can not be explicitly resolved due to their computation cost in the atmospheric models. A chain of parameterizations is generally used instead. In this thesis, the concentration is on the parameterizations in the radiative segment of the model.

Despite their capabilities in forecasting one to several days ahead, NWP models are not flawless. Numerous studies have investigated the bias of NWP irradiance forecasts evaluated against observations and highlighted the effect of clouds. Working on 9 NWP and climate models Van Weverberg et al. (2018) showed that radiation errors correlate with the Spatio-temporal evolution of clouds and that the cloud contribution to surface SW radiation bias dominates other factors such as surface properties and water vapor amount. The evaluation of the 2.5 km resolution AROME (Seity et al., 2011) model irradiance simulations over the French Alps presents a positive bias due to the underestimation of cloud cover, (Vionnet et al., 2016; Quéno et al., 2020). However, even if the clouds are well predicted, the treatment of the radiative properties of clouds in the models can generate errors. Tuononen et al. (2019) evaluated the IFS model skill in forecasting the irradiance over Helsinki. They interestingly found that even correctly predicted overcast cases present a positive (8 W m^{-2}) bias associated with the underestimation of liquid water path (LWP) or misrepresentation of optical properties of clouds having lower LWP. Provided these results, it is noteworthy to briefly introduce how the radiative properties of clouds are computed in atmospheric models.

Clouds can substantially hinder the solar radiation coming from the sun by reflecting a fraction towards space, absorbing a portion of it, and leaving the rest to be transmitted through the

¹Clouds and the Earth’s Radiant Energy System (CERES) Energy Balanced and Filled (EBAF) Top-of-Atmosphere (TOA)

cloud. These features, respectively called Reflectance, Absorptance, and Transmittance, are known as the bulk radiative properties of the clouds. Clouds also emit longwave radiation as a black body depending on their temperature (based on Planck's law introduced in 1900). In each model column, the radiative scheme computes the bulk radiative properties in the fraction of the pixel occupied by the cloud (defined by the cloud fraction). This is carried out by deriving the optical properties of the cloud droplet (Slingo and Schrecker, 1982; Edwards and Slingo, 1996), applying a set of hypotheses to deal with the in-cloud heterogeneity of liquid water (Tiedtke, 1996), and the overlap of cloudy grid cells (Hogan et al., 2016) and finally feeding all these information to a solver of the radiative transfer equation (RTE).

Montornes et al. (2015) and Rontu and Lindfors (2018), using respectively WRF and HIRLAM-AROME NWP models, show that for similar atmospheric conditions (including same initial LWP) with an overcast cloud, only changing the SW cloud radiative scheme will impact highly the irradiance forecast and other meteorological variables such as wind speed profiles.

The radiation both in LW and SW can influence clouds in different ways. According to Klinger et al. (2019) LW cooling in cumulus can enhance precipitation via dynamics and microphysics. From a dynamic aspect, it can enhance circulation and increase condensation rate, which means converting more water vapor into droplets. From the microphysics standpoint, LW or thermal cooling of particles that recirculate and arrive at the edge of the cloud (also confirmed by de Lozar and Muesle (2016)) can impact the precipitation. The SW radiation takes part mainly in the diabatic heating term. The diabatic heating interplays in stratocumuli where convection is low (Turner et al., 2018).

Irradiance in climate modeling and the impact of clouds

The general circulation models (GCMs) used for climate modeling, share the same architecture as NWP models, though they have a coarser spatio-temporal resolution. Accordingly, their challenges in estimating CRE are close to that of the NWPs. However, since they can go to the time scale of decades, the response to the error may not be the same.

A recognized response of the Earth system to the warming climate is the poleward shift of the Hadley cells and jet streams. Voigt et al. (2021) highlighted that the clouds are the prominent contributors to this tendency. About 70% of intermodel spread in the estimation of climate sensitivity (the Earth temperature adjustment in response to a doubling of CO₂ concentration) is related to the cloud feedbacks (Vial et al., 2013). Engström et al. (2014) attributes the intermodel spread at the top of the atmosphere to various cloud fraction estimation methods. The uncertainty behavior may vary depending on the cloud type. SW albedo underestimation in bright stratocumuli and under-prediction of cumuli having overestimated albedo are known cases. The latter being called "too few too bright" (Nam et al., 2012). As stated by Bony et al. (2006) marine boundary layer liquid clouds are the primary source of uncertainty. Accordingly, Voigt et al. (2021) shows that subtropical stratocumuli are responsible for most of the positive (meridional) feedback patterns simulated by GCMs (Zelinka et al., 2020). Cloud cover, LWP, the effective radius, and the subgrid heterogeneity of cloud condensate are the reasons for the lack of SW reflectivity in stratocumulus (Ahlgrimm et al., 2018).

Thesis objectives and structure

As highlighted by most of the mentioned studies, clouds demonstrate a remarkable signature on the irradiance estimation errors in NWPs and inter-model uncertainties in the climate

models. Moreover, it can be deduced that even if the model predicts the cloud profile well, the SW radiative scheme that treats the cloud-radiation interactions can significantly change the irradiance or radiative flux estimation. Among the elements of the radiative scheme pointed out earlier, we focus on the cloud particles' optical properties parameterization.

The emphasis is on the SW region due to the significant radiative forcing of clouds in the SW, its stronger sensitivity to cloud microphysics and radiative assumptions, and its more prominent contribution to inter-model spread compared to the LW. Additionally, we target the liquid clouds because of the critical effect of these kinds of clouds on the climate feedback (Bony et al., 2006; Voigt et al., 2021). Another motivation is to fill the literature gap in the liquid SW optical properties of the cloud that will be elucidated in chapter 3 of the thesis.

The SW liquid cloud optical properties parameterization in the atmospheric models involves two steps: 1-Single scattering properties (SSPs) estimation: The quantities responsible for the cloud-radiation interaction in the microscopic scale being extremely variable against the size of the particle and the wavelength of the incident light. 2- Computation of the Droplet Size Distribution (DSD) effective radius from the liquid water content (LWC) and droplet number concentration (N): Two quantities that can be derived from the microphysics scheme of the model. It is noteworthy that distinct assumptions are made on DSD shape through each of the mentioned steps. In addition, several methods are available based on the literature (Hu and Stamnes, 1993; Slingo and Schrecker, 1982; Edwards and Slingo, 1996; Manners, 2015) to average the optical properties over the spectral bands given by the radiative model.

To this end, the main objective of this thesis is to quantify the uncertainties in SW cloud radiative forcing due to the choice of the DSD shape and optical properties spectral averaging methods. This is carried out in 3 main steps, which outline the present thesis.

1. A novel optical properties parameterization is designed, which takes the DSD shape into account in addition to LWC and N . It also contains various spectral averaging methods. This parameterization was first implemented in the ecRad radiative code (Hogan and Bozzo, 2018). Then several offline 1D simulations were performed with this updated version of ecRad on one ideal cloud and four real case clouds. By the offline simulation, we mean that the cloud profile is constant, and only the sensitivity to the radiative part is examined. By choosing various DSD shapes and spectral averaging methods in ecRad through our new parameterizations, we demonstrate the uncertainties on transmitted and reflected radiation for different values of N and LWC (consequently for various effective radii and optical thickness values). This constructs chapter 3 of this thesis.
2. The modified version of ecRad is implemented in the research model of Météo-France, MesoNH. A consistent link between microphysics and radiation is established, which implies communicating the same LWC, N , and DSD shape parameters applied in the microphysics of the model to the radiative scheme. This consistency does not exist in the current MesoNH version; hence we created an appropriate new radiation-microphysics interface. The tools to create the parameterizations and the details of the ecRad radiative code, along with the useful tools in the MesoNH, related to our thesis, are documented in the first and second chapters.
3. By performing 1D simulations on a known stratocumulus case in MesoNH, the aim of chapter 4 is to understand how the quantified uncertainties in chapter 3 propagate temporally and vertically (since, in our study, only 1D simulations have been performed)

interacting with other components of the simulation such as dynamics and microphysics. The impact of radiation uncertainties on the other components of the model (turbulence, microphysics, and thermodynamic processes) at each time step will be reflected as the input in the next call to the radiative code. These simulations will allow us to identify possible feedback.

Chapter 1

Representing cloud-radiation interactions in atmospheric models

Once reaching the Earth's atmosphere, the sunbeams can undergo two types of interactions as they encounter molecules or particles in the atmosphere. Some will be absorbed, and the rest will be scattered. This chapter describes the interactions between light and clouds, starting from the microscopic scale, i.e., the scale of interaction with a particle, and extending to the kilometer scale, i.e., the scale of interaction with the cloud. We will focus on liquid water clouds. Next, we introduce the general radiative transfer equation, which will be further detailed in the succeeding chapter. In the last part, we highlight how gas absorption characteristics interplay with cloud radiative properties.

1.1 Droplet-scale interactions

The interaction of light with particles can be studied in two ways depending on how energy propagation by light is treated. This includes the classical mechanics' view on one hand, which defines light as electromagnetic waves with a continuous amount of energy, and quantum mechanics, on the other hand, which insists on the discrete energy quantities known as photons. As discussed by Bohren and Clothiaux (2006) both notions can be applied, but care must be taken to avoid mixing them up. Photons are sometimes mistakenly used in literature as an alternative to electromagnetic waves. While the photon is not a wave, it can quantify the momentum carried by the wave. Having this point in mind, we distinguish the use of each standpoint in this chapter.

1.1.1 Electromagnetic standpoint

When hitting a particle, a plane electromagnetic wave with a given frequency can excite a cluster of electrons in the particle, which will oscillate at the same frequency. This gives rise to a secondary electromagnetic wave. Solving Maxwell's equations (Pattelli, 2018) for this problem provides the expression for the secondary and primary fields, from which the scattered field can be estimated (Mishchenko et al., 2002). In the case of liquid water droplets that are assumed to be spherical and provided the particle's size and refractive index and the frequency of incoming light, the solution to this problem is known as the Mie theory. The refractive index of each particle type is given by a complex number. The real part indicates the speed of

light propagation, and the imaginary part quantifies the absorption. For liquid water droplets, in the SW, the real part does not vary much (ranging between 1.3-1.34), but the imaginary part can vary over a factor of 10. The refractive index depends on the chemical composition, thermodynamic phase, and temperature of the particle Kokhanovsky (2004).

1.1.2 Mie Theory

Mie theory quantifies the interaction of light with a single spherical particle via three parameters, namely the extinction efficiency, Q_{ext} , the scattering efficiency Q_{sca} and the scattering phase function, $p(\theta)$. The detailed calculations of Mie parameters can be found in Wiscombe (1980); Stephens (1979). The proportion of the geometrical cross-section of the particle normal to the incoming light, G , that contributes to the scattering of the light, C_{sca} , into several directions, gives Q_{sca} . The phase function describes the angular distribution of these scattered waves with respect to the incoming ray angle. The overall energy removed from the light by scattering and absorption is defined as the total extinction or attenuation of the light. The cross-section and efficiency of extinction can be determined similar to the scattering;

$$Q_{\text{ext}} = C_{\text{ext}}/G \quad (1.1)$$

And hence for absorption; $Q_{\text{abs}} = Q_{\text{ext}} - Q_{\text{sca}}$. In addition, the ratio of scattering efficiency to extinction efficiency is known as the single scattering albedo, ω :

$$\omega = \frac{Q_{\text{sca}}}{Q_{\text{ext}}}. \quad (1.2)$$

Another useful quantity that can be derived from the Mie theory is the asymmetry parameter, g , which is the average cosine of the deviation angle defined by the phase function. It will be further detailed in the next chapter (Eq. 2.6). g is positive (negative) when the scattering is mostly forward (backward), and $g = 1$ ($g = -1$) denotes pure forward (backward) scattering. When $g = 0$, the same amount of energy is scattered backward and forward.

Q_{ext} , g and ω are known as the single scattering properties (SSPs) of the droplets. This terminology distinguishes the single and multiple scattering processes. The multiple scattering occurs in a media where an ensemble of scatterers are present. This will be detailed later in section 1.2.1.

There is a subtlety between the Mie Theory and what is generally called the Mie scattering regime. The Mie scattering regime applies to particles comparable to the wavelength of the incident light and is featured by a strong forward scattering peak. For this size and wavelength category, it is crucial to use the Mie theory. Outside of this range, though, there exist simpler approximations. The scattering properties when the particles (having the mean radius or r) are smaller than the incident light ($\lambda \gg r$) are well approximated by the Rayleigh approach. The scattered light energy, in this case, is distributed homogeneously in every direction ($g = 0$), and in each direction, it is proportional to the inverse of the fourth power of the wavelength. Another simple strategy applies to large particles ($r \gg \lambda$). In this case, the geometrical optics is valid, and light can be treated as rays. The question that arises here is: Why do we apply complicated Mie computations? In the course of this thesis, the focus is put on the droplets with radii varying between 1 to 50 μm , and we are interested in the SW radiation. Fig. 1.1 illustrates for three particle with radii 1, 10 and 50 μm the extinction efficiency as a function of the size parameter, $2\pi r/\lambda$ in the SW ($\lambda=0.2-4 \mu\text{m}$) calculated with the Mie theory. It is

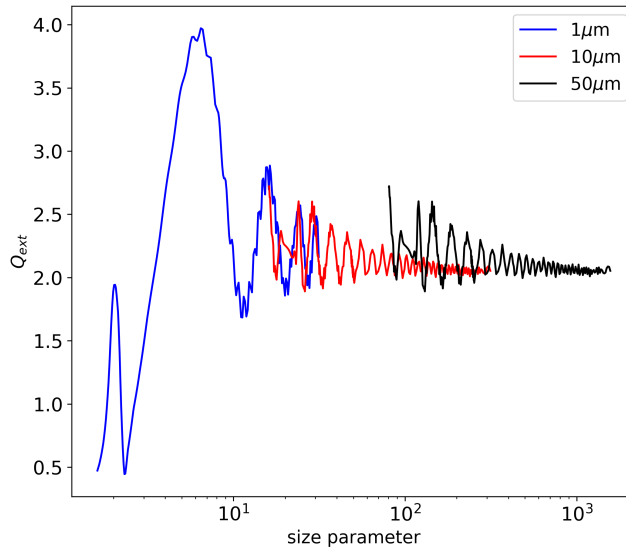


Figure 1.1: Extinction efficiency calculated using Mie theory for three spherical particles with radii of 1, 10 and 50 μm . The Mie computations are performed for a range of size parameter ($2\pi r/\lambda$), where λ varies in the shortwave wavelength range of 0.2-4 μm

discernible from Fig. 1.1 that using either Rayleigh or geometrical approaches, we would have missed all the features in the oscillating parts of the extinction. As stated by Stephens (1979), the fluctuations are due to the interference of light diffracted and transmitted by the particle.

1.2 Cloud-scale interactions

1.2.1 From single to multiple scattering

The cloud is a porous medium made of air and ice or liquid water (and possibly aerosols). The SSPs computed from Mie calculations are only valid for cloud droplets. If the number concentration of droplets per unit volume is called N , then the extinction coefficient is defined as:

$$\sigma_{\text{ext}} = C_{\text{ext}}N. \quad (1.3)$$

This expression only holds for a uni-size collection of particles. In real clouds, the particles are partitioned in different sizes, whereby they can follow an analytical distribution function such as a Log-normal or a Gamma distribution (Brennguier et al., 2011; Vie et al., 2016). In this case, the SSPs should be integrated over these distributions before being applied in 1.3. The integration over droplet size distribution functions are detailed in Eqs. 7-9 of our article in chapter 3.

It must be noted that the scattering obtained from 1.3 is only the result of single-scattering by a distinct particle extended to the cloud. In contrast, the natural attenuation by the droplets dispersed in a cloud is more significant than this quantity. The light entering a volume element of the cloud can be scattered several times by the particles, which increases the chance of absorption. However, quantifying the attenuation from multiple scattering is not straightforward. The reason is that the scattering term of C_{ext} in 1.3 is angular-dependent, and the phase function can not be resolved for all particles in the grid of the model. To deal with this issue, it is

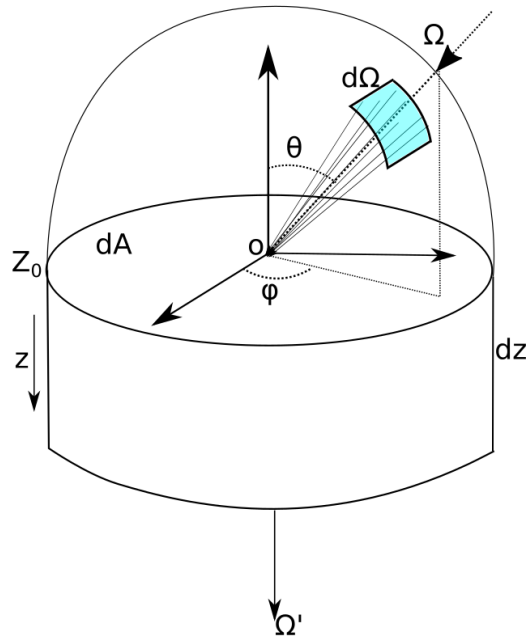


Figure 1.2: Schematic of incoming beams from the solid angle $d\Omega$ around Ω direction, and crossing the volume element of $dAdz$ of the atmosphere.

essential to understand the basics of the radiative transfer in the cloud, which is described in the following section.

1.2.2 Radiative transfer equation

The radiative transfer equation (RTE) is used to characterize the interaction of light with the medium it passes through, and provides the radiance within that medium, given the phase function, σ_{ext} and ω . The RTE has a wide range of applications from astrophysics (Mihalas and Mihalas, 1984) to snow optics (Choudhury, 1981) and cloud radiative forcing derivation (Lacis and Hansen, 1974). Before proceeding into the intricacies of the RTE, it is important to define two essential quantities, i.e., the solid angle and the radiance.

The ensemble of light directions that can be observed from a point of view in the space is identified by what is called the solid angle. If we assume a point at the center of a planar surface element of dA as in Fig. 1.2, an aggregate of vectors of incoming beams toward O , before hitting the point, intersect a part of the virtual sphere around O , defines a solid angle element, $d\Omega$. Assuming that the central axis of the mentioned directions, Ω , has spherical coordinates of θ and ϕ , $d\Omega$ can be written as:

$$d\Omega = \sin \theta d\theta d\phi. \quad (1.4)$$

The radiant energy of monochromatic (having a unique wavelength) beams incoming from a set of directions confined to the solid angle $d\Omega$, crossing a unit area normal to the main propagation direction (Ω), in a steady-state regime (no time dependence), is named radiance, and noted $I(s, \Omega, \lambda)$. s is the position where radiance is measured in the direction of the propagation of the light, and λ indicates the wavelength of the monochromatic beams.

We will present the radiance just for a given wavelength. Hence λ will be omitted in the following equations. As will be detailed later, these monochromatic radiances can then be

integrated over the shortwave spectral bands to calculate the broadband radiance.

We assume that the dA in Fig. 1.2 is an area element at the top surface of a vertical volume element, $dzdA$ from a horizontally infinite homogeneous cloud layer. To find out how much energy flows out at the bottom of this volume element in the direction Ω' , the sources and sinks of the energy in this direction must be defined. The scattering from other directions into Ω' is the main source. To quantify this contribution, we need to determine, firstly, the probability that a wave coming from a given direction Ω is scattered into Ω' . This is given by the phase function $p(\Omega, \Omega')$. The integral is normalized as below:

$$\frac{1}{4\pi} \int_{\Omega} p(\Omega, \Omega') d\Omega = 1. \quad (1.5)$$

It must also be noted that the radiance normal to the upper face of the $dzdA$ is :

$$I(z, \Omega) = \frac{I(s, \Omega)}{\cos \theta} \quad (1.6)$$

A potential secondary source would be the self-emission by the media in the direction of Ω' . However, this source is negligible in the SW at atmospheric temperatures; hence we do not consider it in our RTE.

On the other hand, the propagation of light in the direction of Ω' is dampened due to absorption and scattering, according to σ_{ext} .

Thereby, regarding the conservation of the energy and replacing the polar coordinates of the solid angle from Eq. 1.4, the rate of the radiance change along dz can be written as:

$$\frac{dI(z, \phi, \theta)}{dz} = -\sigma_{ext} I(z, \phi, \theta) + \frac{\sigma_{sca}}{4\pi} \int_0^{2\pi} \int_0^{\frac{\pi}{2}} p(\phi, \theta, \phi', \theta') I(z, \phi, \theta) \sin \theta d\theta d\phi. \quad (1.7)$$

The integral of extinction over a given path length, is known as the optical thickness τ :

$$\tau = \int \sigma_{ext} dz. \quad (1.8)$$

Given the definition of τ , by assuming $\cos \theta = \mu$ and dividing both sides of Eq. 1.7 by σ_{ext} , and integrating over the azimuth angle ϕ , we obtain:

$$\mu \frac{dI(\mu, \tau)}{d\tau} = -I(\tau, \mu) + \frac{\omega}{2} \int_{-1}^1 p(\mu, \mu') I(\mu, \tau) d\mu. \quad (1.9)$$

This is the basic radiative transfer equation. It shows that the radiance in one direction depends on the radiances in all other directions. It must be noted that $I(\mu, \tau)$ corresponds to the total radiance, the sum of direct and diffuse radiances. 'Direct' means the radiation has not undergone any scattering, while by the diffuse light, we mean that the radiant wave has already been scattered. These radiances must be integrated over all upward and downward directions to result in upward and downward fluxes ($F \uparrow$ and $F \downarrow$):

$$F \uparrow (\tau) = 2\pi \int_0^1 I(\tau, \mu) \mu d\mu \quad , \quad F \downarrow = 2\pi \int_0^1 I(\tau, -\mu) \mu d\mu \quad (1.10)$$

These kinds of integrals, however, are not straightforward to obtain due to the angular dependence of the radiance. The details of this issue will be further explored in Section 2.1.1. Once $F \downarrow$ and $F \uparrow$ are computed, the bulk radiative properties of the cloud, namely, reflectance,

transmittance, and absorbance, can be estimated. The ratio between the downwelling flux at the bottom of the cloud $F \downarrow_{\text{base}}$ and the downwelling flux at the cloud top $F \downarrow_{\text{top}}$ gives the transmittance (T) of the cloud. The proportion of $F \downarrow_{\text{top}}$ that is reflected to the atmosphere at the cloud top, $F \uparrow_{\text{top}}$, defines the reflectance (R) of the cloud. The latter is sometimes called the plane albedo. The absorbance of the cloud can be calculated as $1 - R - T$.

The RTE defined in Eq.1.9 is valid for a homogeneous cloud layer. Several possibly inhomogeneous layers containing clear sky and fractions of clouds, aerosols, and other gases must be considered to be able to generalize these equations through the whole atmosphere. This requires a priori, the derivation of SSPs for each mentioned component in each layer, and an appropriate method to combine them before feeding into the RTE. These issues are detailed and discussed in the next chapter. Moreover, in the previous RTE description, we have focused just on a given wavelength. As it was shown, for example, in Fig. 1.1, Q_{ext} exhibits large fluctuations against wavelength in the SW for the droplet size range of interest (1-50 μm). Nevertheless, the ω variations vs. wavelength are much more significant than that of Q_{ext} . Deriving the SSPs and dealing with the RTE at high spectral resolution is costly for the atmospheric models. This is why radiative models most often use a set of spectral bands. The SSPs must be averaged over these spectral bands (detailed in the Eqs. 10-12 of our article) after being integrated over the DSDs, as explained in the previous section.

It is worth noting that the absorption of gases is more sensitive to the wavelength than the SSPs of droplets. They also overlap the absorption by droplets over some spectral bands. To elucidate this issue, we concentrate more on gas absorption in the next section.

1.3 Gas absorption and overlapping issue

In the gas phase, interactions occur at the molecule scale. The gas molecules are considerably smaller than the wavelength of the incoming light; therefore, the scattering occurs in the Rayleigh regime. The scattering by the gas molecules in the cloud is generally negligible compared to the scattering by the droplets. The absorption is the dominant attenuating factor of light in the presence of the gases. Understanding the molecules' absorption requires preliminary knowledge about the transition from classical mechanics to the quantum mechanics notions of energy transport by light. This subject is addressed in the following subsection. Subsequently, the treatment of the absorption in atmospheric models is described. Finally, the overlapping of the droplet absorption by the gases and consequent issues and impact on the derivation of radiative properties of clouds are discussed.

1.3.1 Quantum standpoint in the light energy partition: Photons

As explained at the beginning of this chapter, photons measure the momentum of electromagnetic waves. The energy of a photon carried by an electromagnetic plane wave having the angular frequency of $\tilde{\omega}$ is given by:

$$E = hc\tilde{\omega}/2\pi, \quad (1.11)$$

where h is Planck's constant ($6.625 \times 10^{-34} \text{Js}$) and c is the speed of light. A photon from the incoming radiation can cause a change in the energy state in the target molecule. This energy can be transformed into molecules' collisional, rotational, and vibrational motion modes. As quantum physics implies, the difference between two adjacent energy levels for each of

mentioned motion phases can be presented as a factor of photon energy, $hc\nu$, where ν is the wavenumber (note that the ν here is the inverse of the wavelength but generally in literature it can be used as an equivalent of c/λ) of the incoming light. Since hc is a constant, the energy of levels are presented in terms of wavenumber to facilitate the link with incident light. ν_0 is the highest possible energy difference between two given levels which generally corresponds to the collision mode (between two molecules). The rest of the energies are distributed around ν_0 following a function called the line shape. The basic line shape is given by Lorentz as below (Bohren and Clothiaux, 2006):

$$f_c(\nu) = \frac{a_c}{(\nu - \nu_0)^2 + a_c^2} \quad (1.12)$$

Where $a_c = \gamma/4\pi c$ is the half-width of the line. γ accounts for the viscous damping effect, and ν_0 is the wavenumber at the center of the line. The c subscript in a_c corresponds to collisional mode. Line parameters depend on the temperature and pressure of the gas. The collection of these lines for every energy level of a molecule, gives the absorption lines of that molecule.

1.3.2 Absorption computation in atmospheric models

The absorption lines can be calculated explicitly for an atmospheric layer where the absorbers' temperature, pressure, and amount are homogeneous, using a line-by-line code. In such a code, the absorption cross sections are first calculated for the line centers and are then broadened following the line shape. A sample of these lines is illustrated in Fig. 1.3-a. Then the transmission through the atmosphere is calculated by (Lacis and Oinas, 1991):

$$T(u) = \frac{1}{\Delta\nu} \int_{\Delta\nu} e^{-k_\nu u} d\nu, \quad (1.13)$$

where u is the number of absorbers and $(\Delta\nu)$ the wavenumber range, and $k_\nu u$ is the absorption at wavenumber ν . About 10^6 lines are required to explicitly resolve the absorption variations in the SW (Lacis and Oinas, 1991) with a line-by-line model. This is too costly for an atmospheric model. However, the spectroscopic databases, like HITRAN (Gordon et al., 2022), can provide the reference to develop approximations to calculate the absorptions more rapidly. One of these methods widely used in atmospheric models is called k-distribution. The k-distribution method classifies the monochromatic absorption line strengths in descending order. The sample of these ordered absorption lines is shown in Fig. 1.3-b. Finally, the cumulative distribution function $g(u)$ is derived and inverted as illustrated in Fig. 1.3-c. This allows transforming the integration on the frequency intervals in Eq. 1.13, to the integral on the smoother function g , as follows:

$$T(u) = \int_0^1 e^{-uk(g)} dg, \quad (1.14)$$

where $k(g)$ presents indeed the inverse of the cumulative function $g(k)$. The discretization of the integral in Eq. 1.14 requires remarkably lower quadrature points or sub-intervals than in Eq. 1.13. The value of $g(k)$ in these sub-intervals is also known as g -points in the radiative models. In spectral regions where more absorption lines exist, more g -points are needed.

The k-distribution strategy not only saves time, but also remains accurate over distinct horizontal layers since it depends mainly on the absorption strength rather than the absorber amount

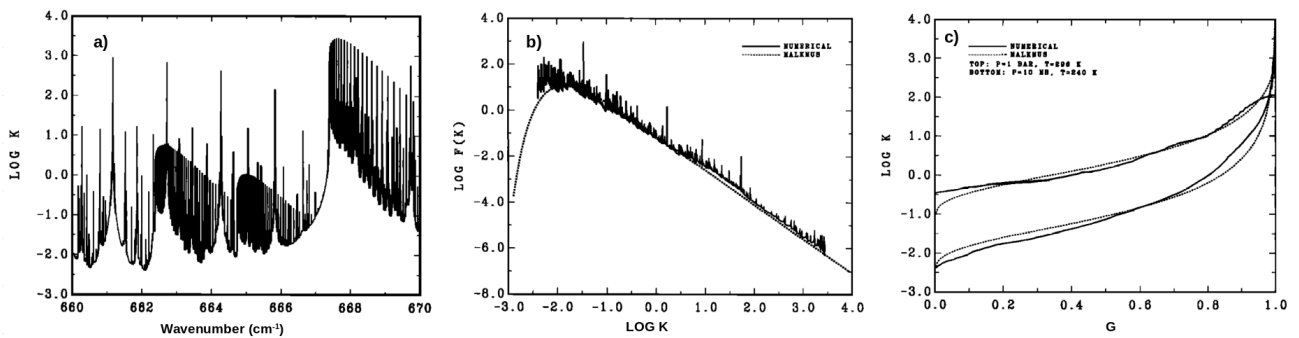


Figure 1.3: Absorption coefficient spectrum for the $1510\text{-}1520\text{ cm}^{-1}$ portion of the water vapor absorption band. a) Line-by-line absorption coefficients for a pressure of 10 mbar and temperature of 240 K. b) Ordered absorption coefficients of a) and frequency distributions function fitted on them. c) The inverse of cumulative distribution function or the k-distribution values of the absorption coefficient spectra of a). The figure is reproduced from Lacis and Oinas (1991)

which can vary with altitude.

1.3.3 Water vapor-Droplet absorption overlapping

As discussed earlier in this chapter, clouds are a mix of droplets, water vapor, and possibly aerosols. Therefore, we can not rely just on the optical properties of the droplets to derive the bulk radiative properties of this ensemble. Using a radiative transfer model (ARTDECO), we performed a simulation within the Air Force Geophysics Lab (AFGL) mid-winter atmosphere Anderson et al. (1986). In this simulation, the only absorbing gas is water vapor. The continental polluted (high value of aerosols) cumulus cloud from Hess et al. (1998) is located at 1 km altitude. The transmittance through the atmosphere is calculated in the presence and absence of the cloud over the SW ($0.2\text{-}2.5\ \mu\text{m}$). The results, illustrated in Fig. 1.4, reveal that the maximum absorption of the water vapor overlaps the absorption by cloud droplets. In these overlap regions, the light is already absorbed by the water vapor before being modified by the cloud droplets. This issue must be considered in the spectral averaging of the cloud optical properties. Further discussions about this overlapping problem will be raised in chapter 3.

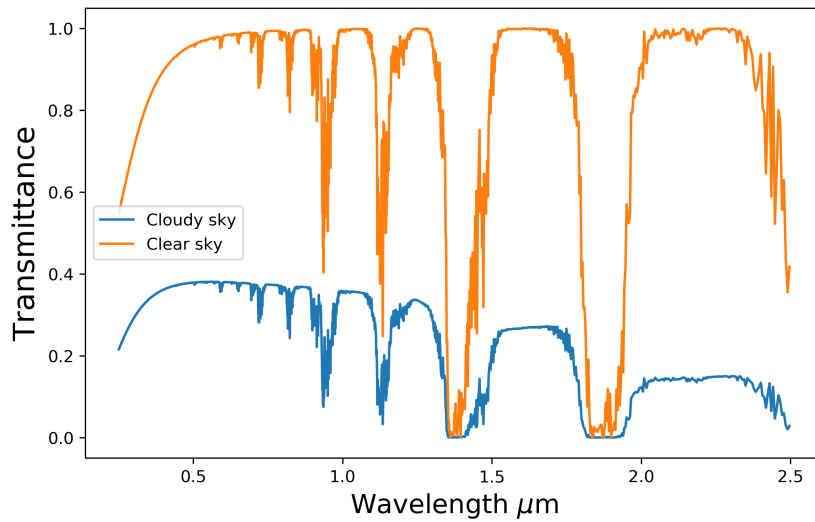


Figure 1.4: The transmission of the AFGL atmosphere (explained in the text) with and without the cloud, the water vapor being the only present gas.

Chapter 2

Tools and models

This chapter documents the tools employed throughout this thesis. The first part focuses on the radiative tools incorporating 1- A simplified formulation of the two-stream solution of the radiative transfer equation, 2- the ecRad radiative code where our parameterizations of optical properties are embedded, 3- The description of the ARTDECO model, which will serve in chapter 3 to provide benchmark calculations of optical properties to evaluate the two-stream model. The second part of the chapter describes Meso-NH, the mesoscale model in which the modifications of the parameterization of optical properties are tested. In particular, the physical parameterizations are detailed with a focus on the current links between the microphysics and the radiation scheme highlighting the existing flaws.

2.1 Radiative codes

One of the main objectives targeted in this thesis is the development of new optical properties parameterizations that rely on distinct methods of SSPs' averaging over the spectral bands (given by the radiative model, ecRad). To develop each method, we need an analytical formula for Transmittance, Reflectance, and Absorbance of a homogeneous cloud. For this purpose, the two-stream method is applied. The first part of this chapter will present this method and describe how it allows computing bulk radiative properties from SSPs over each spectral band.

Furthermore, the spectral averaging methods developed based on the two-stream approximation must be evaluated against a more detailed model. For these evaluations, the ARTDECO radiative model is employed. The ARTDECO options relevant to our application are detailed in section 2.1.3.

Our cloud optical properties parameterizations were implemented in ecRad. Consequently, using ecRad, we can assess the impact of the DSD shape and SSPs spectral averaging method on fluxes uncertainties. The architecture of ecRad and how it computes fluxes from physical inputs are explained in section 2.1.2. ecRad is also the radiation code implemented in the Meso-NH research model.

2.1.1 Two-stream method

The aim here is to deal with the RTE presented in Section 1.2.2 but for the fluxes rather than radiances.

As stated earlier, we are interested in the solar flux transmitted or reflected by clouds. Thus we can only limit our computations to vertical directions and integrate the radiances over two hemispheres to obtain upward and downward direction fluxes as we did in Eq. 1.10. Given

these fluxes, Eq. 1.9 will turn into two differential equations in terms of the flux for the diffuse part of the radiation (Meador and Weaver, 1980; Aquino and Varela, 2005):

$$\frac{dF^-(\tau)}{d\tau} = -2\pi \int_0^1 I(\tau, -\mu)d\mu + \pi\omega \int_0^1 \int_{-1}^1 I(\tau, \mu')p(-\mu, \mu')d\mu'd\mu - S_1F_0 \quad (2.1)$$

$$\frac{dF^+(\tau)}{d\tau} = 2\pi \int_0^1 I(\tau, \mu)d\mu + \pi\omega \int_0^1 \int_{-1}^1 I(\tau, \mu')p(\mu, \mu')d\mu'd\mu + S_2F_0, \quad (2.2)$$

where F_0 is the direct incident radiation hitting the top of the cloud and the equivalent for S_1 and S_2 can be found in Eqs. 15-17 of Aquino and Varela (2005). Eqs. 2.1 and 2.2 are the basics of the two-stream method. For the direct part of the radiation, solving Eq. 1.9 in terms of the flux is more straightforward (Eq. F22 of Libois (2014)).

The dependence of radiances on the incident and scattering angles complicates dealing with the integro-differential equations 2.1 and 2.2. The radiances in the integrals can not be resolved explicitly in all directions. To address this issue, a system of assumptions on the directional distribution of scattering is generally made in atmospheric models.

For this purpose, we apply the δ -Eddington method among various strategies of two-stream such as quadrature, the hemispheric constant and hybrid composition of these methods (listed in Meador and Weaver (1980) and Harshvardhan and King (1993)).

It must be noted that the version of the two-stream we present in the following aims at approximating the bulk radiative properties of only one homogeneous layer of cloud. This can be then extended to the plane parallel horizontally homogeneous layers, as is the case for the McICA solver of the ecRad detailed in 2.1.2.

δ -Eddington

The two-stream equations represent a class of solutions based upon varying approximations of the phase function and the angular integral of the intensity field in the radiative transfer equation (Eq. 1.9). As a solution we use a mix of Eddington (Shettle and Weinman, 1970) and δ scaling (Joseph et al., 1976) methods, called δ -Eddington.

The phase function, integrated on the azimuthal directions, can be written as a sum of Legendre polynomials functions:

$$p(\mu, \mu') = \sum_{n=0}^N (2n+1)\chi_n P_n(\mu)P_n(\mu') \quad (2.3)$$

Where P_n is the n^{th} order polynomial and χ_n coefficients are defined by:

$$\chi_n = \frac{1}{2} \int_{-1}^1 p(\mu, \mu') P_n(\mu) d\mu. \quad (2.4)$$

$p(\mu, \mu')$ can be normalized in the form below:

$$\frac{1}{2} \int_{-1}^1 p(\mu, \mu') d\mu = 1. \quad (2.5)$$

The first moment of these Legendre polynomial gives the g (asymmetry parameter):

$$g = \frac{1}{2} \int_{-1}^1 \mu p(\mu, 1) d\mu \quad (2.6)$$

In the Eddington method, the phase function is approximated by its first two-term truncation as:

$$p(\mu, \mu') = 1 + 3g\mu\mu' \quad (2.7)$$

The diffuse intensity in 1.9 can also be written in the form of Legendre polynomials. The first truncation of these polynomials is used in the Eddington approach:

$$I(\tau, \mu) = I_0(\tau) + \mu I_1(\tau) \quad (2.8)$$

Applying the two latter simplifications, Eq. 1.9, in azimuth independent condition and the absence of direct radiation, can be resumed in the form:

$$\mu \frac{dI(\mu, \tau)}{d\tau} = -I(\tau, \mu) + \frac{\omega}{2} \int_{-1}^1 (1 + 3g\mu\mu') (I_0(\tau) + \mu I_1(\tau)) d\mu. \quad (2.9)$$

However, the Eddington method is unsuitable for highly asymmetric scattering phase functions, such as the strong forward-scattering by cloud droplets (corresponding to the Mie scattering regime). Therefore we use a set of transformations, known as δ approximation, to decompose the phase function into a purely forward and a more isotropic phase function. In this case, g reads:

$$g = \frac{1}{2} \int_{-1}^{-1} \mu p(\mu, 1) d\mu = f + (1 - f)g^* \quad (2.10)$$

where f defines the purely forward scattering portion of the Eddington phase function, and g^* is the asymmetry parameter for the rest of the phase function. f is chosen so that the second moment of the initial phase function is conserved. Assuming that the Henyey-Greenstein function is used as the phase function, its second moment equals g^2 . Thus we can write:

$$f = g^2, \quad g^* = \frac{g}{1 + g} \quad (2.11)$$

This implies subsequent scaling also on ω and τ as below:

$$\tau' = (1 - \omega f)\tau, \quad \omega' = \frac{\omega(1 - f)}{1 - \omega f} \quad (2.12)$$

These δ -transformed SSPs must be replaced in 2.8 and 2.7.

Integro-differential Equations

Applying the δ -Eddington transformations on Eqs. 2.1 and 2.2, Aquino and Varela (2005) proposed a solution called diffuse-type equations which gives the upward and downward fluxes as:

$$F^+(\tau) = K_1 e^{\kappa\tau} + \Gamma K_2 e^{-\kappa\tau} + G^+ e^{-\tau/\mu_0}, \quad (2.13)$$

$$F^-(\tau) = \Gamma K_1 e^{\kappa\tau} + K_2 e^{-\kappa\tau} + G^- e^{-\tau/\mu_0} + F_0 \mu_0 e^{-\tau/\mu_0}, \quad (2.14)$$

where μ_0 is the cosine of the solar zenith angle. The direct solar irradiance at the top of the cloud, $F_0 \mu_0$ contributes to the downward flux. In the following we show how assuming two different boundary conditions at the cloud top, can change the solution to Eqs. 2.14 and 2.13.

Boundary conditions

If no direct solar radiation exists at the top of the cloud, Eqs. 2.13 and 2.14 can be written as:

$$F^+(\tau) = K_1 e^{\kappa\tau} + \Gamma K_2 e^{-\kappa\tau} \quad (2.15)$$

$$F^-(\tau) = \Gamma K_1 e^{\kappa\tau} + K_2 e^{-\kappa\tau} \quad (2.16)$$

Where,

$$\gamma_1 = \frac{1}{4} [7 - \omega^*(4 + 3g^*)], \quad \gamma_2 = \frac{-1}{4} [1 - \omega^*(4 - 3g^*)] \quad (2.17)$$

$$\kappa = \sqrt{\gamma_1^2 - \gamma_2^2} \quad (2.18)$$

$$\Gamma = \frac{\gamma_1 - k}{\gamma_2} \quad (2.19)$$

This condition is called the diffuse method hereafter. Eqs.2.15 and 2.16 can be solved considering two boundary conditions; 1- No reflection of the light at the lower (surface) boundary of the cloud: $F^+(\bar{\tau}) = 0$ and 2-The downwelling energy at the top of the cloud is defined as: $F^-(0) = F_0$. The Reflectance and Transmittance of the cloud are hence:

$$R = \frac{F^+(0)}{F_0} \quad T = \frac{F^-(\bar{\tau})}{F_0} \quad (2.20)$$

Eqs.2.15 and 2.16 are solved on these boundary conditions for two cloud type assumptions: Solving 2.15 and 2.16 at the top $\tau = 0$ and lower boundary $\tau = \bar{\tau}$ of cloud leads to:

$$\Gamma K_1 + K_2 = F_0 \quad \text{and} \quad K_2 = \frac{-K_1 e^{2\kappa\bar{\tau}}}{\Gamma} \quad (2.21)$$

$$K_1 = \frac{\Gamma F_0}{\Gamma^2 - e^{2\kappa\bar{\tau}}} \quad , \quad K_2 = \frac{-F_0 e^{2\kappa\bar{\tau}}}{\Gamma^2 - e^{2\kappa\bar{\tau}}} \quad (2.22)$$

In this case the radiative properties of the cloud with an optical depth of τ^* will be:

$$T = \frac{\Gamma K_1 e^{\kappa\tau^*} + K_2 e^{-\kappa\tau^*}}{F_0} = \frac{e^{\kappa\tau^*} (\Gamma^2 - 1)}{\Gamma^2 - e^{2\kappa\tau^*}} \quad (2.23)$$

$$R = \frac{\Gamma(1 - e^{2\kappa\tau})}{\Gamma^2 - e^{2\kappa\tau}} \quad (2.24)$$

Testing the diffuse method, we obtained negative values for transmittance for the wavelengths greater than $2.5 \mu\text{m}$. This is also in line with the results obtained by Wiscombe (1977). Applying the boundary conditions on Eqs. 2.14 and 2.14, this time in the presence of direct radiation, the K_1 and K_2 read:

$$K_1 = \frac{\Gamma G^- e^{-\kappa\tau^*} - G^+ e^{-\tau^*/\mu_0}}{e^{\kappa\tau^*} - \Gamma^2 e^{-\kappa\tau^*}}, \quad (2.25)$$

$$K_2 = -(G^- + \Gamma K_1). \quad (2.26)$$

The Reflectance and Transmittance of a cloud with the optical depth of τ will be:

$$R = \frac{F^+(0)}{F^-(0)} = \frac{K_1 + \Gamma K_2 + G^+}{F_0 \mu_0} \quad (2.27)$$

$$T = \frac{F^-(\tau^*)}{F^-(0)} = \frac{\Gamma K_1 e^{\kappa \tau^*} + K_2 e^{-\kappa \tau^*} + G^- e^{-\tau^*/\mu_0} + F_0 \mu_0 e^{-\tau/\mu_0}}{F_0 \mu_0} \quad (2.28)$$

Where the required parameters are given by:

$$G^- = \frac{\mu_0^2 \omega F_0}{(\kappa \mu_0)^2 - 1} \left[\left(\gamma_1 + \frac{1}{\mu_0} \right) \gamma_4 + \gamma_2 \gamma_3 \right], \quad (2.29)$$

$$G^+ = \frac{\mu_0^2 \omega F_0}{(\kappa \mu_0)^2 - 1} \left[\left(\gamma_1 - \frac{1}{\mu_0} \right) \gamma_3 + \gamma_2 \gamma_4 \right], \quad (2.30)$$

$$\gamma_3 = \frac{1}{4}(2 - 3g^* \mu_0) \quad , \quad \gamma_4 = \frac{1}{4}(2 + 3g^* \mu_0). \quad (2.31)$$

To this end, to estimate the bulk radiative properties we use the method that considers direct radiation at the cloud top, since it remedies the problem of negative transmittance values, fixing the incident angle at 50° . This gives us an analytic formula that allows the calculation of radiative properties from SSPs in a given spectral band.

2.1.2 Structure of ecRad radiative code

ecRad (Hogan and Bozzo, 2018) is the radiative code implemented in the European Centre for Medium-Range Weather Forecast's (ECMWF's) Integrated Forecast System (IFS). Since 2017, ecRad is also available in the atmospheric research model used at Météo-France, Meso-NH (Lac et al., 2018) (details in the next section). Improving numerous aspects of the previous version of ECMWF radiative scheme, McRad (Morcrette et al., 2008), ecRad has been made 40% faster. In addition, the modular structure of ecRad makes it flexible for any modifications. Optical properties of clouds or aerosols, for instance, can be altered independently without needing to manipulate the solver (the component which deals with solving the radiative transfer equation). This allows us to implement our new SSPs parameterizations directly in the liquid optical properties module of ecRad. We will give an overview of ecRad components, including the input parameters, the spectral resolution of the model, optical properties of atmospheric and surface elements, and finally, the solver choice and computation of the flux profiles.

Input parameters from atmospheric model

The input parameters to ecRad include an atmospheric profile, solar zenith angle, and surface albedo. The atmospheric profile contains the host model's prognostic variables, including the temperature, pressure, cloud fraction, mixing ratios of water vapor, liquid, and ice (and possibly rain, snow, and graupel if they are activated in the microphysics scheme), and the concentration of gases and aerosols. ecRad processes 1D vertical atmospheric columns. In Meso-NH, ecRad is called for every column of the model. On the vertical, only pressure and temperature are required at half-levels, while the remaining parameters are at full levels. The effective radius of the DSD is another input to the radiative code and is computed depending on the host model. For Meso-NH, this is explained in section 2.2.4 and more detailed in section 2.1 of the article in 3.

Spectral resolution

The optical properties of cloud particles, aerosols, and gases, must be averaged over each spectral band specified in ecRad. The averaging method varies among each mentioned component depending on their spectral behavior. This is especially crucial in gases where absorption is highly sensitive to the wavelength variation. To deal with this, ecRad uses the g-points derived from the k-distribution method as explained in the section 1.3.2. ecRad applies the RRTM-G spectral band configuration, which contains 14 and 16 spectral bands in the SW and LW, respectively (Morcrette et al., 2008), and equivalently includes 112 g-points in the SW, and 140 in the LW Mlawer et al. (1997).

The optical properties of cloud particles (Ice and Liquid) are parameterized in terms of effective radius (of the liquid droplet or ice crystal). In this thesis, we intend to add our new parameterization designed for the optical properties of liquid clouds.

The surface module contains the LW emissivity on two bands and SW diffuse and direct albedo on 6 spectral bands. These are interpolated on the 14 RRTM-G bands and fed into the solver.

Geometrical characteristics of clouds and sub-grid inhomogeneity

The host atmospheric model provides only the cloud fraction and water content to ecRad, whereas no information is provided about the sub-grid heterogeneity and cloudy layers' vertical arrangement. ecRad enables opting for different assumptions of vertical cloud overlapping and horizontal heterogeneity of the water content.

The plane parallel uniform clouds assumption, despite its effectiveness, may lead to substantial biases of cloud bulk radiative properties (Harshvardhan and Randall, 1985; Carlin et al., 2002) due to neglecting the horizontal inhomogeneity. Cahalan et al. (1994a) proposed using a scaling factor of 0.7 on the optical depth of the grid box before performing plane parallel calculations (applied by Tiedtke (1996) later as a parameterization in the ECMWF model). This coefficient, however, was derived for marine stratocumulus and may not be suitable for other cloud types. Moreover, any scaling factor also depends on the scale on which the cloud optical properties are averaged (Szczap et al., 2000). A more explicit strategy to account for the sub-grid scale inhomogeneity is the independent column approximation (ICA) method (Cahalan et al., 1994b) on columns generated with a cloud generator. ICA relies on decomposing the domain into independent columns within which it solves the RTE (applying homogeneous plane parallel assumption). By independent, we mean that no horizontal transfer is permitted between the columns. The domain averaged broadband flux (integral of fluxes on every spectral interval) for the radiation grid is then calculated by (Pincus et al., 2003):

$$F_{\text{mean}} = (1 - a_c) \int s(\lambda) F^{clr} d\lambda + a_c \int s(\lambda) \left[\int p(s) F(s, \lambda) ds \right] d\lambda \quad (2.32)$$

Where a_c is the total cloud fraction prognosticated from the model. $S(\lambda)$ is the incoming radiation at the TOA on the spectral interval of λ . ecRad proposes three different solvers to tackle the heterogeneity issue, namely : HOMOGENEOUS, McICA¹ (Pincus et al., 2003), Tripleclouds (Shonk and Hogan, 2008) and SPARTACUS² (Hogan et al., 2016). The latter solver additionally enables the 3D treatment of the radiative transfer equations. HOMOGENEOUS solver supposes that clouds are homogeneous in the horizontal directions and occupy

¹Monte Carlo Integration of independent column approximation

²Speedy Algorithm for radiative Transfer through cloud sides

all the cloudy fractions of the model grid. McICA remedies the problem of the double integral in Eq. 2.32, by randomly associating one specific cloud state to a given g -point. Tripleclouds assumes that the water content in a vertical level of a grid box is distributed through a Gamma or log-normal pdf, which the user must select. The pdf median is used to split the cloudy region into a thick and thin cloud. The LWC of the thin cloud is set to the 16th percentile of the cumulative probability of the same distribution function. The LWC of the thick cloud portion is derived based on conserving the mean total water content of the grid.

All solvers use the two-stream method to deal with the radiative transfer equation, although sub-grid horizontal transport is parameterized in SPARTACUS. The heterogeneity treatment in SPARTACUS is similar to Tripleclouds.

Once the horizontal heterogeneity is addressed, to handle the vertical overlapping issue between cloudy layers, another set of hypotheses is available in ecRad. The cloudy fraction of layers can be vertically correlated. Geleyn and Hollingsworth (1979) assumed that the overlap between the cloud layers is maximum where the cloud is vertically contiguous. That means, if for two adjacent layers of a and b , the cloud covers are denoted with C_a and C_b , the total cloud cover would be $C_{max} = Max(C_a, C_b)$. In addition, if a cloud-free layer exists between two cloudy layers the overlap is random, $C_{rand} = C_a + C_b - (C_a C_b)$. The problem of this method emerges in the multitude-layer cases since it treats the layers in pairs. For instance, an approximately zero cloud fraction in an interstitial layer of a cloud patch can maintain continuity and lead to a maximum overlap. While if the same layer is set to zero, the overlap is random between two separated parts of the cloud. A significant difference can be generated due to a minute change in an intermediate layer. In order to remedy this problem, Hogan et al. (2016) used a more coherent strategy. To achieve the total projected cloud cover at a given level, they apply the MAX-RAN method between this specific cloud layer and the cumulative cloud cover of all upper levels instead of considering just the cloud cover of the upper level. This is how the MAX-RAN method of ecRad is designed. Furthermore, based on the radar observations, Hogan and Illingworth (2000) demonstrated that the total cloud cover, C_{True} of a column is a mix of random and maximum strategies and can be written as:

$$C_{tot} = \alpha C_{max} + (1 - \alpha) C_{rand} \quad (2.33)$$

Where α is the overlap parameter and depends exponentially on the distance between two cloud layers, ΔZ and a decorrelation length ΔZ_0 :

$$\alpha = \exp\left(-\frac{\Delta Z}{\Delta Z_0}\right) \quad (2.34)$$

This strategy is available as the second overlap option in ecRad called EXP-RAN. EXP-EXP is another derivative of the latter method, which assumes the exponential correlation can exist between the separated cloud layers.

The simulations for the third chapter are performed uniformly with McICA. However, for the 1D cases, this is equivalent to the homogeneous since the cloud fraction was set to 1.

2.1.3 ARTDECO

This section will summarize the essential components of the Atmospheric Radiative Transfer Database for Earth Climate Observation (ARTDECO)³ model that will be used later in chapter 3 to evaluate the two-stream method developed in this study. ARTDECO is developed and maintained at Laboratoire d’Optique Atmosphérique (LOA) and distributed by the data and services center AERIS/ICAR (University of Lille), and funded by the TOSCA program of the French space agency (CNES). This tool aims to assemble the reference 1D available radiative codes and dataset, allowing us to simulate the radiances and fluxes in the earth’s atmosphere as seen by the passive sensors on-board satellites. ARTDECO is composed of 5 main modules:

- Atmosphere module: The atmospheric profile is defined in this module. It can be selected from a set of standard profiles available in the library. If any fixed gas concentration exists, it can be defined here. Then the program will read the absorption coefficients and continuum information for these gases from the library.
- Surface module: Surface features, e.g., type, albedo, temperature, etc., are defined in this part.
- Particles module: This is where the particle’s type, method of calculating the particle’s optical properties, the optical thickness of the cloud where the particles are located, and the altitude where the cloud is located are defined. The last parameter determines if the cloud occupies all atmospheric layers of the introduced atmospheric profile or is distributed vertically with the user-defined layout. If the defined type of particle exists in the library of ARTDECO, it will calculate the mean optical properties of particles in the cloud using the Mie theory, using the refractive index of that species, and the droplet size distribution function details that can be entered by the user. Samples of optical properties of clouds and aerosols of known cases are already available in the library. ARTDECO also allows the users to prescribe their own optical properties under the condition that they provide the Legendre coefficients of the phase matrix expansion. These can be calculated if the phase function is available. If this is not the case, an Henyey-Greenstein phase function will be used to calculate the Legendre coefficients from the asymmetry parameter, g .
- Main module: All modules described till here were indeed the inputs to the radiative core. As with all radiative models, the last critical step is dealing with the radiative transfer equations via a solver. ARTDECO incorporates DISORT method (Hu and Stamnes, 2000), 1D monte carlo (Cahalan et al., 1994b) and Adding-doubling method (Lacis and Hansen, 1974) as the solver choice for the user. By activating each of these solvers in the main interface, a secondary configuration file with the abbreviation name of the solver is created, which requires manipulation before running the simulation.

2.2 Meso-NH model description

Meso-NH is a non-hydrostatic atmospheric model for meso-scale simulations (Lac et al., 2018), developed jointly by the Laboratoire d’Aérodynamique (UPS/CNRS) and CNRM (CNRS/Météo-France). It is designed for the research goals of modeling the meteorological processes from synoptic (up to several hundred kilometers) to turbulent scales (on the order of meters), and it

³Available at <https://www.icare.univ-lille.fr/artdeco/download/>

allows for developing parameterizations for the application in the operational prevision model. The prognostic variables in each time step and the center of each grid in MesoNH incorporate potential temperature, the mixing ratio of various water species such as raindrop, cloud droplets, water vapor, and more species depending on the microphysics scheme, the subgrid turbulent kinetic energy (TKE) and hydrometeor concentrations in the case of 2-moment microphysics scheme application. The wind components, responsible for the advection of the scalar variables, are situated at the faces of the model grid. Solving the Eulerian equations of the transport in each grid (ensuring energy, momentum, and mass conservation) is not straightforward. To deal with the term which contains the advection of wind components, a discretization method is applied. This discretization can be carried out differently depending on the available computation resources and the scale of the simulation. Weighted essentially non-oscillatory (WENO), and centered discretization of fourth (CENT4th) and second order (CEN2end), are the available options in Meso-NH. WENO is appropriate for large scales and simulations that inhibit significant gradients winds. In finer scales though, WENO soon becomes numerically diffusive. For higher resolutions, CEN4th is the recommended option.

Meso-NH can be run in 1D, 2D or 3D mode. In 1D, the advection is not solved (however a forcing from the coarser scale may be present), and computations are carried out through a single column model (SCM). In 3D mode, Meso-NH can be used for both idealized simulations or real cases, with a wide range of horizontal resolutions, up to large eddy simulations (LES) where 80 percent of turbulent energy is resolved, or even Direct Numerical Simulations (DNS). Meso-NH features advanced physical parameterizations for subgrid processes. In the following, we will focus on microphysics, turbulence and radiation parameterizations. This triplet is tightly interactive in space and time. The following gives a brief description of the schemes that deal with these processes in MesoNH

2.2.1 Turbulence scheme

A turbulence scheme aims at reproducing the impact on the resolved variables of the different turbulent eddies. If the resolution is fine enough (lower than 500 m), the thermals (large coherent vertical structures) are explicitly resolved, and the turbulent scheme is needed to represent the turbulent transport carried out by the vortices of scale lower than the mesh. It is assumed that the turbulence is isotropic, and we use a K-diffusion type scheme where the vertical turbulent flows are expressed as a function of the vertical gradients of the resolved variable (temperature, moisture, or wind) and a transfer coefficient (the eddy-diffusivity) which depends on the turbulent kinetic energy for which we have a prognostic equation (Cuxart et al., 2000) and a length scale. This configuration is set for the LES simulations used in Chapter 3. If the resolution is coarser, we also need to represent, with a parameterization, the effect of thermals (coherent structures with a size of the order of the boundary layer). In that case, in addition to the K-diffusion scheme, we use a mass-flux scheme (Pergaud et al., 2009) following the eddy-diffusivity mass flux framework. This configuration is used in the simulations used in Chapter 4.

2.2.2 Radiation scheme

The radiative scheme calculates the radiative fluxes in each grid. These fluxes are used to calculate atmospheric heating/cooling rates and surface fluxes for the surface energy budget. The radiation is the first scheme called in a time step of simulation in MesoNH. It provides the

energy on the surface and atmosphere to trigger turbulence and larger-scale atmospheric circulations and control the microphysical phenomena. As mentioned in section 2.1.2 ecRad is the radiative scheme employed in this thesis, and it has been available in MesoNH since version 5.4. Though in the following, a brief overview of other available shortwave and longwave schemes is provided.

Two longwave schemes exist as in ancient versions of IFS. One based on Morcrette et al. (1986); Morcrette (1991) splits the LW into six bands of different gases' absorption lines. The other is RRTM Mlawer et al. (1997) containing 16 spectral bands relying on the k -distribution method. The parameterizations of cloud LW SSPs include that proposed by Smith and Shi (1992) and Savijärvi and Räisänen (1998). Malavelle, is the third SSPs parameterization that works for both LW and SW. It is based on the internship of Malavelle carried out in Météo-France, concerning the evaluation of SSPs delivered by different parameterizations against detailed Mie calculation. The conclusion was to opt for the optical thickness of Savijärvi and Räisänen (1998), the asymmetry factor of Fouquart Fouquart and Bonnel (1980) and the single scattering albedo of Slingo (Slingo, 1989).

In shortwave, the only scheme originally available was that designed by Fouquart and Bonnel (1980). They have used a path distribution method to calculate the absorption both in clouds and gases. The SW has six bands in this scheme; if SSPs parameterizations are not outlined for these six bands, their coefficients are interpolated. In the SW the SSPs parameterizations of Slingo and Schrecker (1982), Fouquart and Bonnel (1980) are available.

2.2.3 Microphysics scheme

Several microphysics schemes are available in Meso-NH. We will focus here on the 2-moment scheme LIMA (Liquid Ice Multiple Aerosols Vie et al., 2016) which is a bulk 2-moment microphysical scheme. Bulk schemes assume that the particle size distribution (PSD) of hydrometeors follows a chosen continuous distribution function, for several water species, such as rain, droplets, ice crystals etc. Different moments of these distribution functions are then used to describe the microphysical processes. Bulk schemes predict the evolution of different moments of the PSD. For example, 1-moment schemes usually predict the third moment, which is proportional to the hydrometeor mass mixing ratio. 2-moment schemes use a second prognostic variable, allowing the scheme to represent the cloud composition and its variability better. Usually, the number concentration of hydrometeors (the zeroth moment of the PSD) is predicted.

LIMA was built upon the 1-moment scheme ICE3 (Pinty and Jabouille, 1998), used operationally in the regional convective-scale model AROME at Météo-France. Thus, it inherits the ICE3 hydrometeor species (cloud droplets, raindrops, ice crystals, snow/aggregates, graupel, and hail as an option). As in ICE3, for each species, the PSD follows a generalized gamma distribution function:

$$n(D)dD = N \frac{\alpha}{\Gamma(\nu)} \lambda^{\alpha\nu} D^{\alpha\nu-1} \exp(-(\lambda D)^\alpha) dD, \quad (2.35)$$

where $n(D)$ is the number concentration of the droplets with diameter D per unit volume.

The α and ν parameters are fixed at the start of the simulation, while the shape parameter λ is calculated in each model grid box depending on the hydrometeor number concentration and mass mixing ratio. It is interesting to note here that, for $\alpha = 1$, the PSD becomes a standard

gamma distribution function, and $\alpha = 1$ and $\nu = 1$ give the widely used Marshall-Palmer (exponential) distribution.

At each time step of the simulation, the evolution of the prognostic variables, namely the concentration and mixing ratio of hydrometeors, is predicted, accounting for all the processes that can impact these variables while ensuring the conservation of the total water mass. These mechanisms can be non-microphysical such as advection and turbulence, or microphysical processes. Since we are interested in warm liquid clouds, the microphysical processes include activation of aerosols into CCN, sedimentation of cloud droplets and raindrops, autoconversion and accretion of cloud droplets into raindrops and condensation and evaporation of raindrops and cloud droplets.

LIMA relies on the assumption that supersaturations with respect to liquid water remain low and spurious and therefore uses an adjustment procedure at the end of each timestep which ensures that an equilibrium is reached: if the grid box is supersaturated, water vapor condenses form cloud droplets until saturation is reached, and if the grid box is undersaturated, cloud droplets evaporate until saturation is reached. The raindrop condensation/evaporation processes rely on the explicit computation of the water vapor transfer rates.

In the 2-moment scheme LIMA, the number of cloud droplets N formed in clouds is explicitly calculated from the number of aerosols activated as cloud condensation nuclei (CCN). The treatment of the activation, though, is not straightforward. Based on the Köhler theory, aerosols' activation occurs when supersaturation becomes higher than a threshold value. This value depends on aerosol size and characteristics (whether they are hygroscopic, the degree of solubility, etc.). Since LIMA uses a saturation adjustment, the supersaturation is not correctly predicted. Instead, the parameterization of Cohard et al. (1998) is used, i.e., a diagnostic of maximum supersaturation (S_{\max}) that the air parcel can reach is computed based on its vertical velocity, the radiative cooling tendency, and the water vapor condensation on CCN and cloud droplets. This parameterization was improved in LIMA to handle the competition of several aerosol modes (with different size distributions and chemical compositions).

LIMA also relies on a prognostic aerosol population to initiate the formation of cloud droplets and ice crystals. This population is defined by a certain number of modes, each one being defined by its chemical composition (and thus varying abilities to act as cloud condensation and/or ice freeing nuclei) and log-normal size distribution with a chosen modal diameter and spectral width. LIMA can use as many aerosol modes as necessary to represent complex aerosol populations, although increasing the number of prognostic variables obviously makes the simulations longer. The aerosol population can be initialized from observations, aerosol climatologies, or CAMS real-time analyses and forecasts. The evolution of aerosols includes their transport by resolved and sub-grid motions and their interaction with clouds (activation and evaporation of droplets and ice crystals, and precipitation scavenging). LIMA does not include aerosol emission, aging, and sedimentation schemes but can be coupled to the ORILAM (Tulet et al., 2005) aerosol scheme in Meso-NH.

The explicit aerosol treatment in LIMA allows a robust treatment of the Twomey effect (Twomey, 1974) on the microphysical processes. We aim to profit from such thorough aerosol microphysics consideration, to enhance the radiative forcing of aerosols in future works. This goal is achievable by coupling LIMA and our new parameterizations, as will be detailed in the next section.

c2R2 and *KHKO* are the other 2-moment microphysics schemes in MesoNH. *C2R2* is based on the scheme developed by Cohard and Pinty (2000) and is recommended for use in modeling

the clouds containing large raindrops such as cumulus. The *KHKO* leans on the study of Khairoutdinov and Kogan (2000) for the precipitating stratocumulus and was implemented in MesoNH by Geoffroy et al. (2008).

2.2.4 Communication between the radiation and microphysical schemes

The only possible bridge between microphysics and radiation in Meso-NH is the interface where the effective radius is calculated before being fed to the radiation. Generally, the number concentration, N , is diagnosed from experimental formulations such as that of Martin et al. (1994), based on a given value of aerosol number concentration. Only the mixing ratios of hydrometeors are obtained from the microphysics. Several attempts have already been made on the older version of the radiation model to use the appropriate number concentration diagnosed by the microphysics scheme in the radiation code. Based on these approaches, the prognosticated N from warm microphysics schemes of *C2R2* and *KHKO* can be used to compute the r_{eff} prior to being used in Malavelle and Savijervi parameterizations. These couplings have been scarcely documented or evaluated, and there exists a lack of scientific results of possible simulations with these couplings in MesoNH. Moreover, no DSD shape communication is still available between microphysics and radiation. The r_{eff} in the radiative code is derived from N and the mixing ratios of hydrometeors, utilizing the observation-based method of Martin et al. (1994) which assumes two different DSD shapes based on the aerosol number concentration.

To this end, we have added a new option in the ecRad interface of effective radius computation that reads the N , mixing ratio, and the DSD type and shape directly from the LIMA microphysics scheme. Based on this new consistent coupling between microphysics and radiation, we will perform different simulations with Meso-NH, in chapter 4 to investigate the impacts of consistency between radiation and microphysics scheme on 1D simulations.

Chapter 3

Uncertainties in climate models due to the parameterization of liquid cloud optical properties

3.1 Introduction

Recalling from the last two chapters, the atmospheric models use parameterizations to estimate the clouds' optical properties, including single scattering properties (SSPs) parameterization and effective radius estimation. These parameterizations imply a set of assumptions on the DSD shape and the spectral averaging of optical properties over the spectral bands. It could happen to most of the atmospheric model users that they unconsciously activate a default radiative scheme. This default option may use an optical properties parameterization designed for another type of cloud and microphysical conditions, not appropriate with the one simulated by the atmospheric model. In this case, the choice of a suitable parameterization is not straightforward. To probe this issue, we try to answer three main questions:

- How are microphysics and radiation schemes related in actual atmospheric models?
- How much uncertainty can be generated in the bulk radiative properties (Transmittance, Reflectance, Absorbance) due to the assumptions on the shape of droplet size distribution (DSD) and SSPs spectral averaging method?
- How much of such uncertainty is related to the SSPs parameterization and what is the contribution of effective radius estimation?

The answer to the first question is partly provided in the section 2.2.4 and its brief background will be explained in this introduction. The 2 remaining questions are answered through this chapter.

In most atmospheric models, the water content of various hydrometeors is the only information provided by one-moment microphysics schemes (detail in the section 2.2.3) to the radiative code. Based on this fact, most of the early liquid cloud SSPs parameterizations relied on the liquid water content, LWC (or LWP), to describe the optical properties of clouds' particles (e.g., in Rockel et al. (1991), and Stephens (1978)). Fig. 3.1a,b shows the mean optical depth

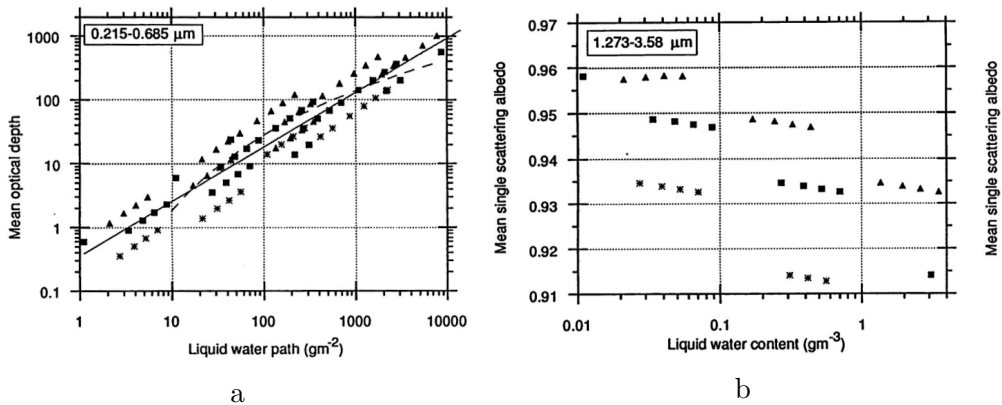


Figure 3.1: Figure adapted from Rockel et al. (1991) displaying in a) Mean optical depth (over the band 0.215-0.685 μm) versus LWP and in b) Mean single scattering albedo (on the band 1.273-3.58 μm) for clouds having effective radii in the range 0.18 – 24 μm and effective variance between 0.01 and 0.25. Stars, squares and triangles indicate values for N of 1, 100 and 500 cm^{-3} . The complete and dashed-lines in *a* represent the parameterizations of Rockel et al. (1991) and Stephens (1978) respectively.

and single scattering albedo, respectively, calculated for distinct values of droplet number concentration, N , denoted by different geometrical shapes, and illustrated against LWP by Rockel et al. (1991). The parameterization of Stephens (1978) and Rockel et al. (1991) are shown in dashed and full lines respectively in Fig. 3.1-a. An uncertainty bound is observable around the fitted curves in Fig. 3.1-a due to the choice of the N . This issue accentuates in Fig. 3.1b, where no meaningful relationship can be captured between single scattering albedo and LWC for clouds of different N . The problem is hidden behind the dependence of N and LWC on the shape of the droplet distribution. It can be demonstrated that the N and LWC can be related to each other by the effective radius r_{eff} and a DSD shape parameter named k Martin et al. (1994). More recent parameterizations, such as Slingo and Schrecker (1982); Slingo (1989); Edwards and Slingo (1996), hence formulated the SSPs in terms of r_{eff} . Their method consists of a crude fitting of an analytical function on the SSPs calculated for several clouds, having different features and DSD shapes. They use the limited cases of cloud observations already used by Stephens (1978), which were adapted from the earlier study of Carrier et al. (1967). The DSD shape was still not the determining factor of these parameterizations. Most of these parameterizations are still used in a wide range of atmospheric models. This is a motivation for us to explore the impact of DSD in SSPs parameterizations.

To answer the two last questions, in this chapter, we have proposed a new set of parameterizations that consider the DSD shape and include several spectral averaging methods. Our designed parameterizations are then implemented in ecRad. The offline version of ecRad is used to simulate the radiative fluxes in 1D atmospheric profiles to study the potential uncertainties.

This chapter consists of a published article in the JAMES journal, a complementary section that provides additional details on the issues encountered in deriving the parameterizations, and a discussion on spectral averaging methods and the impact of the N on the uncertainty behavior.

3.2 Article:Uncertainty of SW Cloud Radiative Effect in Atmospheric Models Due to the Parameterization of Liquid Cloud Optical Properties



RESEARCH ARTICLE

10.1029/2021MS002742

Key Points:

- The estimation of cloud single scattering properties (SSPs) is affected by not accounting for the droplet size distribution (DSD) and by spectral averaging over wide bands
- The impact of the DSD shape on the estimation of r_{eff} is significant, and slightly offset by the weak dependency of SSPs to DSD shape
- The global cloud radiative effect simulated by a climate model can vary up to 13% depending on the assumed DSD

Correspondence to:

Q. Libois,
quentin.libois@meteo.fr

Citation:





Jahangir, E., Libois, Q., Couvreur, F., Vié, B., & Saint-Martin, D. (2021). Uncertainty of SW cloud radiative effect in atmospheric models due to the parameterization of liquid cloud optical properties. *Journal of Advances in Modeling Earth Systems*, 13, e2021MS002742. <https://doi.org/10.1029/2021MS002742>

Received 27 JUL 2021

Accepted 21 NOV 2021

© 2021 The Authors. Journal of Advances in Modeling Earth Systems published by Wiley Periodicals LLC on behalf of American Geophysical Union. This is an open access article under the terms of the [Creative Commons Attribution-NonCommercial-NoDerivs License](https://creativecommons.org/licenses/by/4.0/), which permits use and distribution in any medium, provided the original work is properly cited, the use is non-commercial and no modifications or adaptations are made.

Uncertainty of SW Cloud Radiative Effect in Atmospheric Models Due to the Parameterization of Liquid Cloud Optical Properties

E. Jahangir¹, Q. Libois¹ , F. Couvreur¹ , B. Vié¹ , and D. Saint-Martin¹ 

¹CNRM, Université de Toulouse, Météo-France, CNRS, Toulouse, France

Abstract Clouds are largely responsible for the spread of climate models predictions. Here we focus on the uncertainties in cloud shortwave radiative effect due to the parameterization of liquid cloud single scattering properties (SSPs) from liquid water content (LWC) and droplet number concentration (N), named parameterization of cloud optical properties. Uncertainties arise from not accounting for the droplet size distribution (DSD)—which affects the estimation of the effective radius (r_{eff}) and modulates the r_{eff} -dependency of the SSPs—and from averaging SSPs over wide spectral bands. To assess these uncertainties a series of r_{eff} -dependent SSPs parameterizations corresponding to various DSDs and spectral averaging methods are derived and implemented in a radiative code. Combined with the DSD-dependent estimation of r_{eff} they are used to compute the bulk radiative properties (reflectance, transmittance, absorptance) of various clouds (defined in terms of LWC and N), including a homogeneous cloud, more realistic case studies, and outputs of a climate model. The results show that the cloud radiative forcing can vary up to 20% depending on the assumed DSD. Likewise, differences up to 20% are obtained for heating rates. The estimation of r_{eff} is the main source of uncertainty, while the SSPs parameterization contributes to around 20% of the total uncertainty. Spectral averaging is less an issue, except for atmospheric absorption. Overall, global shortwave cloud radiative effect can vary by 6 W m^{-2} depending on the assumed DSD shape, which is about 13% of the best observational estimate.

Plain Language Summary Climate predictions differ a lot from one model to another, and the difficulty to simulate how clouds will behave in a warmer world is largely responsible for that. The radiative effect of clouds depends on the size of the individual droplets forming a cloud, a quantity that is not explicitly represented in climate models. In this study we investigate how not accounting for the detailed droplet size distribution affects the capability of climate models to reliably predict the radiative effect of clouds. By assuming a variety of droplet size distributions in a set of simulations, we observe that apparently similar clouds in climate models can have very different radiative impacts depending on the assumed distribution. This is primarily attributed to the estimation of the effective radius of cloud droplets, a key quantity that drives cloud radiative properties. Differences up to 20% are observed on critical quantities such as fluxes at top-of-atmosphere and at the surface. The absorption of radiation within clouds is also significantly altered. The impact on the global estimate of shortwave cloud radiative effect is around 13%, which highlights the need to improve the representation of the microphysical characteristics of clouds to run more reliable climate predictions.

1. Introduction

The Earth radiative budget, which is the primary driver of Earth's climate, is largely governed by clouds, whose response to global warming remains the largest source of uncertainty in the estimation of the effective climate sensitivity (the change in near-surface temperature resulting from CO_2 doubling) by state-of-the-art general circulation models (GCMs) (Zelinka et al., 2020). In the shortwave (SW), clouds tend to cool the Earth by reflecting solar radiation. On the contrary, clouds trap longwave (LW) radiation emitted by the surface, which tends to warm the system. The cloud radiative effect (CRE, Charlock & Ramanathan, 1985), defined as the difference between net radiative fluxes in cloudy and clear-sky conditions (either at the top of atmosphere [TOA] or at the surface), quantifies these counteracting cooling and warming effects. The best estimations from a combination of satellite (Loeb et al., 2018) and ground measurements (Wild et al., 2019) suggest that CRE is about -47.7 W m^{-2} in the SW at TOA (-56 W m^{-2} at the surface) and 28 W m^{-2} (both at TOA and at the surface) in the LW, meaning that

clouds overall cool the system. Although in average GCMs reproduce these observations well, significant differences exist among the CRE simulated by 38 individual GCMs participating in the sixth phase of the Coupled Model Intercomparison Project (CMIP6) as reported by Wild (2020). Indeed, the SW CRE at TOA ranges from -41 to -60 W m^{-2} (-43 to -63 W m^{-2} at the surface) while the LW CRE at TOA ranges from 19 to 29 W m^{-2} (22 to 30 W m^{-2} at the surface). This points to the long-standing difficulty to simulate clouds and their radiative effect, and makes questionable the capability of GCMs to predict how CRE might be altered in a warmer climate.

Several factors can explain these inter-model discrepancies: differences in total cloud fraction (Nam et al., 2012; Vignesh et al., 2020), location of the clouds, diurnal or seasonal cycles of the clouds, cloud optical properties (Engström et al., 2014; Hu & Stamnes, 2000), radiative treatment of cloudy layers (Costa & Shine, 2006; Pincus et al., 2003) or even surface albedo (Hourdin et al., 2013). Although there are many reasons for clouds to differ amongst GCMs, due to differences in the physical parameterizations trying to catch the complex and unresolved physical processes of cloud formation and evolution, it is worth pointing out that even with identical clouds (same spatial distribution, cloud fraction, amount of condensate etc.), distinct GCMs may predict distinct CRE. This stems from the fact that CRE fundamentally depends on the way cloudy layers are treated in the radiative scheme of each model (e.g., Fouquart et al., 1991), and how their bulk radiative properties—namely transmittance, reflectance and absorptance—are computed.

Generally GCMs rely on one-moment microphysical schemes, meaning that only the hydrometeors water contents (liquid, ice, rain, snow etc.) are prognostic variables. It implies that the number concentration N of cloud particles, and consequently the effective radius r_{eff} of the hydrometeors (the ratio of the third moment to the second moment of the particle size distribution), are simply diagnosed from the liquid water content (LWC) and ice water content (IWC) (most often along with a prognostic aerosols mass concentration (e.g., Boucher & Lohmann, 1995)). Hence radiative transfer schemes in GCMs essentially take as inputs vertical profiles of LWC, IWC, cloud fraction, and aerosol concentration, and rely on a succession of assumptions to compute radiative fluxes based on this limited information. In addition, for computation cost reasons, the radiative calculations are performed in a limited number of spectral bands, in which the single scattering properties (SSPs) of clouds are considered constant. This number can range from a single one (Geleyn et al., 2017) to a dozen (as in the Rapid Radiative Transfer Model for General Circulation Models Applications [RRTMG; Clough et al., 2005], which is implemented in several GCMs). Computing the bulk radiative properties of clouds thus requires two preliminary steps: (a) treating the vertical overlap of cloud layers and their subgrid horizontal and vertical heterogeneities; (b) parameterizing cloud optical properties for given LWC and IWC. The latter generally includes the parameterization of r_{eff} on the one hand, and the computation of the band-averaged cloud SSPs—that is, the fundamental quantities describing the optical characteristics of a cloudy layer, which are detailed below—on the other hand. The question of cloud overlap has been the focus of many research studies (Di Giuseppe & Tompkins, 2015; Geleyn et al., 1979; Hogan & Illingworth, 2000; Räisänen et al., 2004; Sulak et al., 2020). Subgrid heterogeneities have also been extensively investigated over the past 20 years (Barker et al., 2002; Jouhaud et al., 2018; Pincus et al., 2005; Shonk & Hogan, 2008), including their effects on the intensity of subgrid 3D radiative effects (Barker et al., 2016; Hogan et al., 2016). Regarding cloud SSPs, most recent studies focused on the ice clouds (Edwards et al., 2007; Baum et al., 2011; Yang et al., 2013; W. Zhao et al., 2018), probably because clouds made of spherical droplets have been considered as largely understood. The parameterization of liquid cloud SSPs has indeed received limited attention since the seminal works of Fouquart and Bonnel (1980), Stephens (1978) and Slingo and Schrecker (1982), although the choice of these SSPs has been shown to alter CRE computations (Fouquart et al., 1991; Freidenreich & Ramaswamy, 2005). This impact is much stronger in the SW than in the LW, because multiple scattering makes the bulk radiative properties very sensitive to SSPs. For the aforementioned reasons the present study only tackles the SW radiative properties of liquid clouds.

The interactions of spherical cloud particles with solar radiation is well described by the Lorenz-Mie theory (Van De Hulst, 1968), which applies to particles comparable in size to the wavelength of incident radiation. This theory provides the SSPs of a spherical particle, in particular the extinction efficiency Q_{ext} , the asymmetry parameter g , and the single scattering albedo ω . Q_{ext} determines the fraction of the geometrical cross sectional area that contributes to light extinction. g is the average cosine of the deviation angle of the scattering phase function, the latter describing the angular distribution of scattered light. g is used here instead of the full scattering phase function, because most GCMs rely on two-stream radiative transfer codes which only use g (Fouquart & Bonnel, 1980; Meador & Weaver, 1980). ω quantifies the contribution of scattering to the total extinction. The single scattering

co-albedo $1-\omega$ hence quantifies the contribution of absorption. These SSPs depend on the size of the particles, on the wavelength of incident radiation and on the refractive index of liquid water.

To compute cloud SSPs on given spectral bands, SSPs of individual droplets must be averaged over the cloud droplet size distribution (DSD) and across the spectral bands. Because SSPs strongly vary with droplet size and incident wavelength, and since the DSD is not resolved in a GCM simulation, computing these averages is not straightforward. This has given rise to a variety of parameterizations, generally giving the SSPs for individual spectral bands as a function of r_{eff} . These parameterizations implicitly assume a specific DSD. They also treat in different ways the spectral averaging issue. While g and Q_{ext} barely vary within spectral bands, the co-albedo ($1-\omega$) can show significant variations (up to 100%) in a single band (Dobbie et al., 1999). Since the relationships between bulk radiative properties and the SSPs are highly nonlinear, using linear averages of $1-\omega$ on each spectral band can lead to biases in bulk radiative properties. This issue was tackled with a variety of strategies, most of which aiming at minimizing the errors in flux computations (Chou et al., 1998; Edwards & Slingo, 1996; Espinoza, 1996; Räisänen, 1999). This stresses that spectral averaging has to be carefully considered when attempting to derive new SSPs parameterizations.

In practice, many parameterizations currently used in atmospheric models date back to the 80's and 90's (Edwards & Slingo, 1996; Fouquart, 1988; Slingo & Schrecker, 1982; Stephens, 1978). They are used for instance in the radiative codes available in the Weather Research and Forecasting (WRF) model (Chou et al., 1998; Dudhia, 1989), in the Hadley Centre (Pope et al., 2000) and IPSL (Madeleine et al., 2020) climate models, and in the radiative scheme of the Integrated Forecasting System (Hogan & Bozzo, 2018; Manners, 2015). However, Nielsen et al. (2014) recently pointed out that using the parameterizations from Fouquart (1988) and Slingo and Schrecker (1982) can generate large biases compared to detailed Lorenz-Mie computations. This highlights the need for revisiting the parameterization of SSPs.

The estimation of r_{eff} from LWC also depends on an assumption on the DSD (Martin et al., 1994). In most cases, this underlying assumption is inconsistent with that used to derive the r_{eff} dependent SSPs, although generally none is explicit. For instance Slingo and Schrecker (1982) mention seven different DSDs used to derive their parameterization, but no details are revealed about how SSPs are averaged over these seven DSDs. This also holds for the parameterization of Hu and Stamnes (1993), who in addition use SSPs computed at specific wavelengths rather than averaged over bands. This same study concluded that the impact of DSD shape on SSPs could not exceed 6%, which was cited in subsequent studies as a reason not to focus too much on the DSD. However SSPs were only computed for a cloud with effective radius of $20 \mu\text{m}$, and the differences in SSPs were not translated into errors in bulk radiative properties. In the present study, the DSD assumptions used for estimating r_{eff} and the SSPs, along with the spectral averaging, will be clearly stated.

The overarching objective of this paper is thus to estimate the uncertainties on CRE resulting from the assumption on the DSD and the spectral averaging strategy. To this end, a large set of SSPs parameterizations is developed, based on detailed Lorenz-Mie computations applied to well-defined DSDs, and various spectral averaging methods are used. These new parameterizations are meant to be made available to the community, to be used in place of the historical ones which can hardly be traced back to actual DSDs. These parameterizations are implemented in the radiative transfer code ecRad (Hogan & Bozzo, 2018) and combined to a consistent r_{eff} estimation to assess the overall impact of these choices on the simulated CRE. This sensitivity study is performed for several single column case studies of clouds, as well as for global outputs of a climate model. The paper is partitioned as follows. Section 2 provides complementary details about the DSD and spectral averaging issues. Section 3 describes how the parameterizations are derived and Section 4 shows the application of the newly developed parameterizations on cloudy atmospheres. These results are discussed along with perspectives in Section 5.

2. Theoretical Background

In this section we detail how the shape of the DSD affects the relationship between LWC and r_{eff} , and present the two types of DSDs used in this paper to represent clouds. In addition, preliminary ecRad simulations are performed to demonstrate that changing cloud SSPs parameterization in a radiative transfer code can make a difference in terms of the CRE. This is what initially motivated the present study.

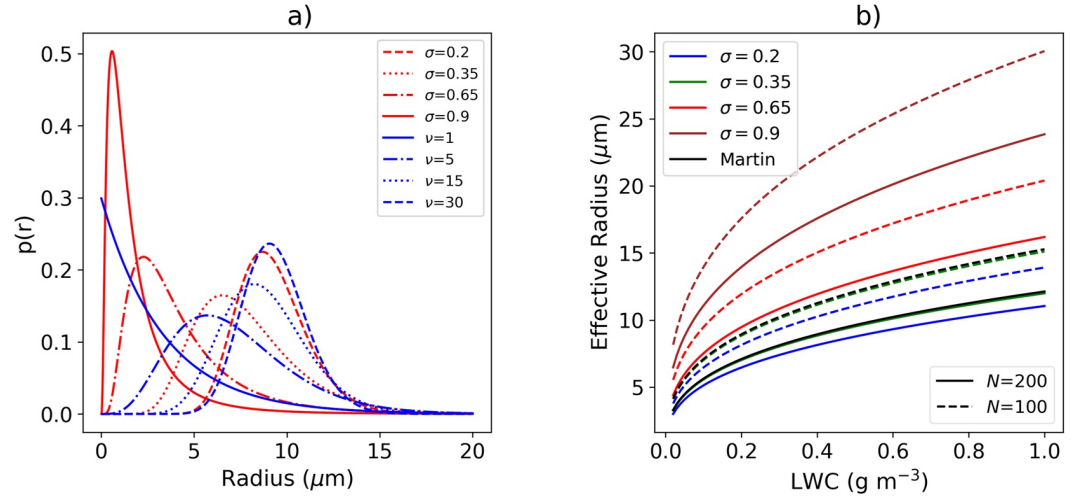


Figure 1. (a) Lognormal and modified gamma functions for different shape parameters (σ and ν correspond to the lognormal and modified gamma functions, respectively) but similar r_{eff} of $10 \mu\text{m}$. (b) r_{eff} -LWC relation derived for 4 lognormal distributions from Equation 5. The solid lines correspond to $N = 200 \text{ cm}^{-3}$ and the dashed lines to $N = 100 \text{ cm}^{-3}$. The curves labeled *Martin* were obtained using the value $k = 0.67$, as recommended by Martin et al. (1994).

2.1. Parameterization of Cloud Optical Properties

Let us consider $n(r)$, the cloud droplet number concentration per unit of cloud droplet radius r , hereafter called DSD. The total number concentration N is defined as:

$$N = \int_0^{\infty} n(r) dr. \quad (1)$$

LWC is proportional to the third moment of the DSD:

$$\text{LWC} = \frac{4}{3} \pi \rho_w N \int_0^{\infty} r^3 p(r) dr, \quad (2)$$

where $p(r) = n(r)/N$ is the normalized DSD and ρ_w is the density of liquid water. The modified gamma and lognormal distributions are commonly used to describe clouds DSD (Geoffroy et al., 2010; Misumi et al., 2018; C. Zhao et al., 2006). In this paper the following forms adapted from Miles et al. (2000) are used:

$$p(r) = \frac{1}{\sqrt{2\pi}\sigma r} \exp\left(\frac{-(\ln(r/r_n))^2}{2\sigma^2}\right), \quad \text{for lognormal}, \quad (3)$$

$$p(r) = \frac{1}{\Gamma(\nu)} \left(\frac{r}{r_n}\right)^{\nu-1} \frac{1}{r_n} \exp\left(-\frac{r}{r_n}\right), \quad \text{for modified gamma}, \quad (4)$$

where r_n is the median droplet radius in Equation 3 and a nonphysical scaling radius in Equation 4, and Γ is the gamma function. σ and ν are hereafter referred as shape parameters. Figure 1a shows these functions for various shape parameters but with a fixed r_{eff} of $10 \mu\text{m}$. It highlights that distributions with identical r_{eff} can be practically very different. For these two DSDs, r_{eff} can be explicitly computed as a function of N and LWC. It takes the following form:

$$r_{\text{eff}} = \left(\frac{1}{k}\right)^{1/3} \left(\frac{3\text{LWC}}{4\rho_w\pi N}\right)^{1/3}, \quad (5)$$

where expressions for the parameter k are provided in Table 1. Hence k only depends on the shape parameters σ or ν . Interestingly, Martin et al. (1994) found a similar relationship between r_{eff} and LWC based on *in situ* observations in stratocumuli, and identified distinct k values for clouds over ocean and over land. They

Table 1
Expressions of k for the Lognormal and Modified Gamma Distributions, in Terms of the Shape Parameters σ and ν

Distribution function	k	r_{eff}
Lognormal	$e^{-3\sigma^2}$	$r_n e^{\frac{3}{2}\sigma^2}$
Modified gamma	$\frac{(\nu^2 + \nu)}{(\nu + 2)^2}$	$r_n (\nu + 2)$

recommend to use $k = 0.67$ over land, and $k = 0.80$ over ocean, which remain widely used values.

LWC and N are the usual variables provided to the radiative scheme. However Equation 5 highlights that an additional shape parameter is needed to compute r_{eff} . Figure 1b shows how r_{eff} varies with LWC for distinct lognormal distributions for N equal to 100 and 200 cm^{-3} . σ varies from 0.2 to 0.9, which covers the field observations reported in Miles et al. (2000). A factor larger than two in r_{eff} is found for these extreme values, which correspond to k values of 0.88 and 0.09, respectively. Thus, neglecting the impact of the shape parameter on the effective

radius results in an uncertainty, called r_{eff} -uncertainty hereafter. When k is not provided to the radiative scheme, the r_{eff} -uncertainty impacts the overall estimation of SSPs, and consequently alters the cloud bulk radiative properties.

r_{eff} has long been identified as the driving quantity for cloud SSPs since it is related to the volume-to-surface-area ratio of liquid droplets, a quantity that compares absorption (which occurs in the volume) and scattering (which occurs at the surface) and naturally arises in the derivation of single scattering albedo (Grenfell & Warren, 1999; Mitchell, 2002). However r_{eff} does not contain any information about the shape of the DSD. For instance, based on aircraft observations, Brenguier et al. (2000) demonstrated that a thin marine cloud ($N = 50 \text{ cm}^{-3}$) or a thick polluted one ($N = 150 \text{ cm}^{-3}$) with very distinct DSDs could have the same r_{eff} . Obviously such different clouds, despite having similar r_{eff} , have different SSPs. Neglecting the influence of the DSD shape when parameterizing SSPs in terms of r_{eff} thus results in a second source of uncertainty when computing bulk radiative properties, hereafter called *SSP-uncertainty*. This highlights that the DSD shape assumption is critical both for r_{eff} estimation and for the subsequent SSPs estimation in terms of r_{eff} . To remain consistent, the same assumption should be made for both steps. This will be carefully ensured in this study.

In practice, one objective of this study is to derive a set of cloud optical properties parameterizations in the following form:

$$Q_{\text{ext}}^i, \omega^i, g^i = f^i(\text{LWC}, N, \text{DSD shape}, \text{Spectral averaging method}), \quad (6)$$

where i refers to individual spectral bands and DSD shape corresponds to a set of lognormal and modified gamma distributions. By implementing these new parameterizations in ecRad, this paper aims at quantifying the contribution of each uncertainty component on the estimation of CRE.

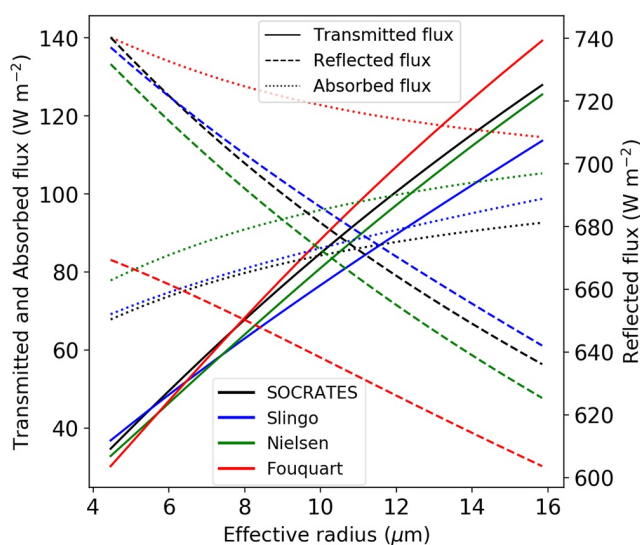


Figure 2. Transmitted, reflected and absorbed fluxes computed for an ideal cloud (details in Section 4.1) with the *Slingo*, *SOCRATES*, *Nielsen* and *Fouquart* SSPs parameterizations, as a function of r_{eff} .

2.2. Preliminary Sensitivity Study

Before implementing the new parameterizations and to give a first hint of the impact of the choice of SSPs on cloud bulk radiative properties, preliminary radiative transfer simulations are performed on an ideal 1D cloud (having a vertically homogeneous LWC of 0.6 g m^{-3} , see details in Section 4.1) with the radiative code ecRad (presented in more details in Section 3.4). In ecRad, two options are natively available to compute the SSPs from r_{eff} : namely *Slingo* (Slingo & Schrecker, 1982) and *SOCRATES* (Edwards & Slingo, 1996; Manners, 2015). Both parameterizations are based on DSD observations dating back to the 70s (Hansen, 1971; Stephens, 1978). In addition, the parameterizations of Nielsen et al. (2014), which was derived from rigorous Lorenz-Mie calculations, and that of Fouquart (1988), which uses also Mie calculations applied to a stratus cloud (described in Hansen, 1971), were implemented. These parameterizations are then used to simulate transmitted (at cloud base) and reflected (at cloud top) fluxes, as well as atmospheric absorption (in-cloud), as a function of r_{eff} (Figure 2). The optical thickness of the cloud is about 126 (at the reference wavelength of 0.55 μm) for $r_{\text{eff}} = 10 \text{ μm}$. Note that this experiment is limited to the r_{eff} range of $4\text{--}16 \text{ μm}$, since the Slingo parameterization is not valid out of this range. The resulting differences can reach several tens of W m^{-2} for fluxes. The lower transmittance obtained with the Slingo parameterization compared to the Nielsen parameterization is in agreement with the

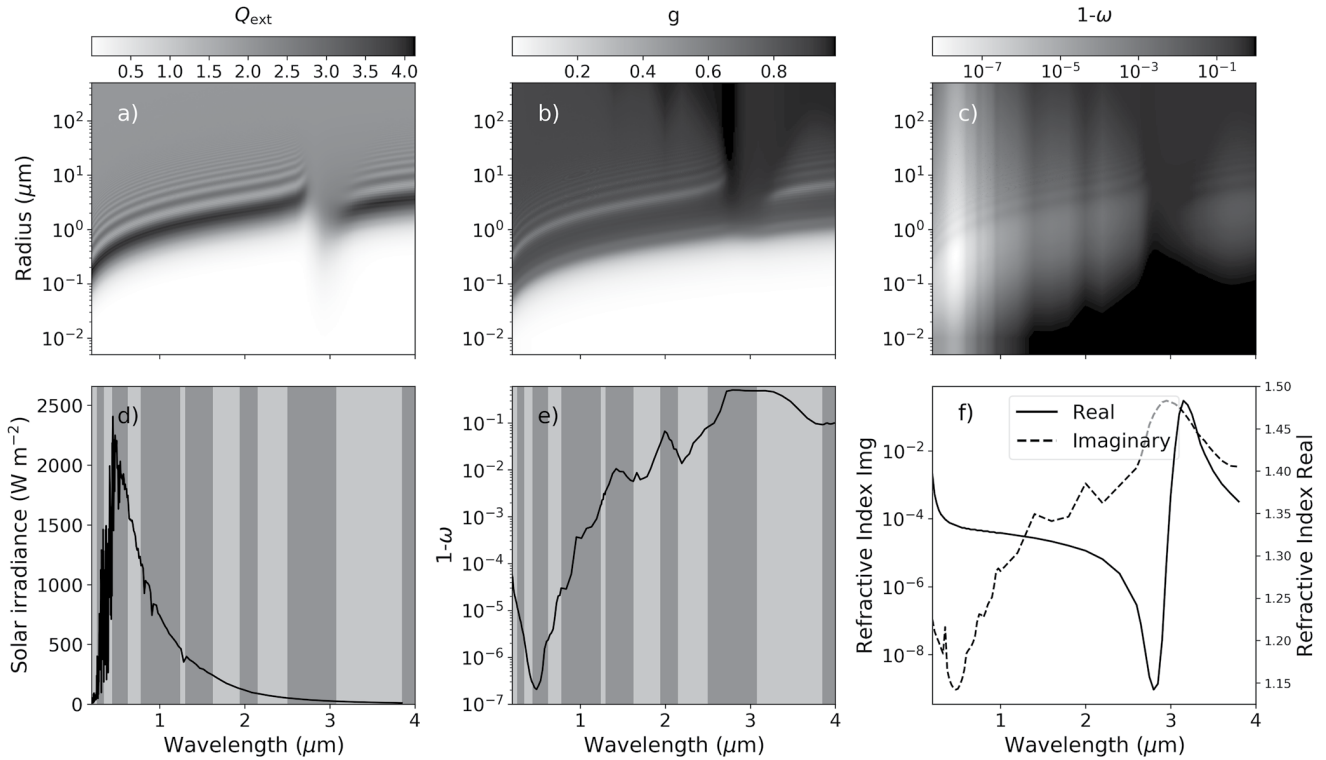


Figure 3. Maps of (a) extinction efficiency (b) asymmetry parameter and (c) co-albedo as a function of radius and wavelength. (d) Solar spectrum from Kurucz (1994). (e) Spectral variations of $1-\omega$ for $r = 10 \mu\text{m}$. Background shades in (d) and (e) correspond to ecRad spectral bands. (f) Imaginary and real parts of water refractive index (Hale & Querry, 1973).

findings of Nielsen et al. (2014). Differences are hard to trace back to physical reasons because the way those parameterizations were developed (in particular regarding the reference DSDs that were used) is not sufficiently detailed in the reference papers. Nevertheless this highlights the importance of cloud SSPs parameterization and the need to assess in a transparent and consistent way its impact on simulated cloud radiative properties.

3. Methodology

This section details how the new parameterizations of cloud SSPs are derived, accounting for DSD shape and spectral averaging. In the end these parameterizations take the form of simple analytical formulas in terms of r_{eff} to facilitate their implementation in any radiative transfer code.

3.1. Computation of Average SSPs Over Droplet Size Distribution and Spectral Bands

Here we consider that r_{eff} has been estimated from LWC and N assuming a particular DSD. The following aims at expressing the SSPs in terms of r_{eff} , assuming the same DSD. The first step thus consists in reconstructing the full DSD based on r_{eff} and the shape parameter (σ or ν). This is straightforward, because r_n can be expressed in terms of r_{eff} and the shape parameter (see Table 1). SSPs for individual droplet radius r and incident wavelength λ have been tabulated from Lorenz-Mie computations (using the Python module *pymiecoated*, based on Mätzler [2002], and the refractive index of liquid water from Hale and Querry [1973]). Figures 3a–3c show the variations of SSPs as a function of r and λ . A characteristic feature is the marked oscillations with r when r is close to the wavelength of the incident light. Figure 3f also highlights that the spectral variations are closely related to the spectral variations of the liquid water refractive index. For a given wavelength the SSPs are first integrated over the DSD as follows:

$$Q_{\text{ext}}(\bar{r}, \lambda) = \frac{\int Q_{\text{ext}}(r, \lambda) r^2 p(r) dr}{\int r^2 p(r) dr}, \quad (7)$$

$$g(\bar{r}, \lambda) = \frac{\int g(r) Q_{\text{sca}}(r, \lambda) r^2 p(r) dr}{\int Q_{\text{sca}}(r, \lambda) r^2 p(r) dr}, \quad (8)$$

$$\omega(\bar{r}, \lambda) = \frac{\int Q_{\text{sca}}(r, \lambda) r^2 p(r) dr}{\int Q_{\text{ext}}(r, \lambda) r^2 p(r) dr}, \quad (9)$$

where \bar{r} denotes the average over the DSD and Q_{sca} corresponds to the fraction of the geometrical cross sectional area that contributes to the scattering of light. The integration is performed numerically by computing the SSPs on the interval 0.01–500 μm , splitted into 10,000 logarithmically spaced sub-intervals. This ensures that the oscillations pointed out in Figure 3 are properly captured. This configuration has been validated against the widely used code of Mishchenko et al. (1999).

The SSPs are then averaged over the spectral bands of the radiative code. This can be done as in Equation 11 of Slingo and Schrecker (1982), weighting the SSPs by the incident solar radiation at the top of atmosphere $S(\lambda)$ (Kurucz, 1994) shown in Figure 3d:

$$Q_{\text{ext}}(\bar{r}, \bar{\lambda}) = \frac{\int Q_{\text{ext}}(\bar{r}, \lambda) S(\lambda) d\lambda}{\int S(\lambda) d\lambda}, \quad (10)$$

$$g(\bar{r}, \bar{\lambda}) = \frac{\int g(\bar{r}, \lambda) Q_{\text{ext}}(\bar{r}, \lambda) \omega(\bar{r}, \lambda) S(\lambda) d\lambda}{\int Q_{\text{ext}}(\bar{r}, \lambda) \omega(\bar{r}, \lambda) S(\lambda) d\lambda}, \quad (11)$$

$$\omega(\bar{r}, \bar{\lambda}) = \frac{\int \omega(\bar{r}, \lambda) Q_{\text{ext}}(\bar{r}, \lambda) S(\lambda) d\lambda}{\int Q_{\text{ext}}(\bar{r}, \lambda) S(\lambda) d\lambda}, \quad (12)$$

where $\bar{\lambda}$ indicates the average on the spectral band. The linear averages displayed in Equations 10–12 are hereafter named *thin averaging*, after Edwards and Slingo (1996). Note, however, that alternatives for the spectral averaging are introduced in the next section. For the spectral integral, 280 wavelengths are used, which corresponds to 20 linearly distributed wavelengths for each of the 14 spectral bands of ecRad (these bands are depicted in Figures 3d and 3e).

The reference SSPs have been computed for 8 different DSD shapes, namely $\sigma = \{0.2, 0.35, 0.65, 0.9\}$ for the lognormal and $\nu = \{1, 5, 15, 30\}$ for the modified gamma. These ranges are consistent with the extreme values reported in Miles et al. (2000). For each shape the SSPs have been computed for 80 values of r_{eff} ranging from 1 to 50 μm .

3.2. Spectral Averaging Methods

The co-albedo $1-\omega$ features large variations across the SW, and within individual bands of ecRad. Figure 3e, which shows the spectral variations of $1-\omega$ for $r = 10 \mu\text{m}$, demonstrates that $1-\omega$ can vary by up to 3 orders of magnitude across a single spectral band. Since the bulk optical properties of scattering media are highly non-linear in terms of the SSPs, which is a consequence of multiple scattering, using linear spectral averaging as in Equations 10–12 may bias the estimated cloud radiative properties. This was already pointed out by Edwards and Slingo (1996), and is further explained below.

Neglecting the effect of gases, the reflectance and transmittance of a homogeneous cloud can be computed using the two-stream approximation (see Appendix A). They can be formally written as (expanded in Equations A1 and A2):

$$T = T_{2S}(\omega, g, \tau), \quad (13)$$

$$R = R_{2S}(\omega, g, \tau), \quad (14)$$

where $2S$ stands for two-stream and τ is the optical thickness of the cloud of geometrical thickness H . By definition (Stephens, 1978; Xu et al., 1996):

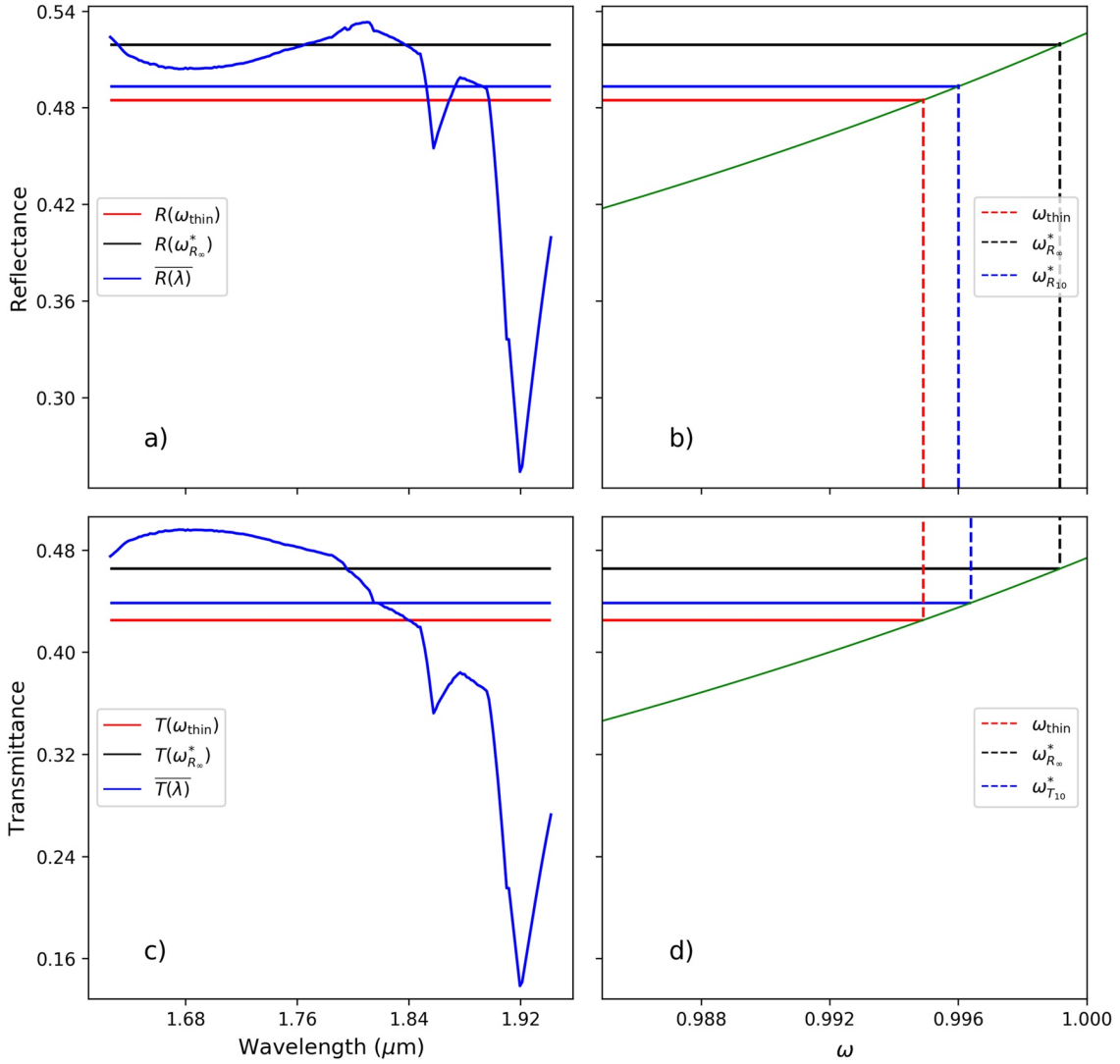


Figure 4. The blue curves in (a and c) show the reference reflectance and transmittance for the spectral band 1.62–1.94 μm , computed with Equations 13 and 14. The horizontal blue lines show the average of these quantities over the spectral band, weighted by the TOA solar spectrum. In (b and d) the green curves show the relation between the monochromatic reflectance, transmittance and ω computed from Equations A1 and A2, using thin averaged values for \bar{g} and Q_{ext} . The red lines indicate the results of Equations 13 and 14 applied to the thin average ω (ω_{thin} highlighted by the blue dashed lines) while the black lines indicate the results of Equations 13 and 14 applied to the thick average ω ($\omega_{R_{\infty}}^*$ highlighted by the black dashed lines). All the computations were made for a cloud with $\tau = 10$ (at $\lambda = 0.55 \mu\text{m}$), $r_{\text{eff}} = 10 \mu\text{m}$ and $\sigma = 0.2$. The dashed blue lines highlight the value that ω should take over that spectral band to match the reflectance ($\omega_{R_{10}}^*$) or transmittance ($\omega_{T_{10}}^*$). Note that $\omega_{R_{10}}^* \neq \omega_{T_{10}}^*$.

$$\tau(\lambda) = H \int Q_{\text{ext}}(r, \lambda) \pi r^2 n(r) dr \quad (15)$$

$$= \frac{3Q_{\text{ext}}(\bar{r}, \lambda) \text{LWP}}{4r_{\text{eff}} \rho_w}, \quad (16)$$

where LWP is the liquid water path of the layer, defined as:

$$\text{LWP} = H \text{LWC}. \quad (17)$$

Using Equations 13 and 14, $T(\lambda)$ and $R(\lambda)$ of an ideal cloud layer with $r_{\text{eff}} = 10 \mu\text{m}$ and $\tau = 10$ (at $\lambda = 0.55 \mu\text{m}$) are computed at high spectral resolution in the band 1.62–1.94 μm , and depicted by the blue curves in Figure 4. The horizontal blue lines show the corresponding averages over the band (weighted by $S(\lambda)$), hereafter named

true properties. We define ω^* , the band-averaged value ω should take for this band to ensure that the transmittance (reflectance) computed from band-averaged properties with Equation 13 (14) equals the true transmittance (reflectance). These are depicted by the dashed blue lines projections in Figures 4b and 4d, where the green lines correspond to Equations 13 and 14 with g and τ corresponding to thin averages. The value ω_{thin} corresponding to thin averaging is highlighted by the red line. Once projected on the left panels it results in about 2% relative errors in reflectance and transmittance compared to the true values. This highlights that using thin averaging to estimate band-averaged $\bar{\omega}$ is not accurate. This is the result of absorption saturation within the band. The linear average $1-\bar{\omega}$ underestimates (resp. overestimates) absorption in the wavelengths where highly absorbing (resp. less absorbing) features of liquid water are present. Depending on the solar energy available in that band this can lead to broadband overestimation or underestimation of absorption.

To circumvent this issue, Edwards and Slingo (1996) have introduced the notion of *thick averaging*. Starting from the statement that $\overline{Q_{\text{ext}}}$ and \bar{g} slightly vary across the SW, they used thin averaging (Equations 10 and 11) to compute the band-averaged quantities for these variables. To approximate ω^* they used a formula equivalent to Equation 14, assuming in addition that $\tau = \infty$, implying that any cloud can be considered optically thick. In this case $\omega_{R_{\infty}}^*$ can be estimated from \bar{g} and $\overline{R_{\infty}(\lambda)}$. Although many clouds are indeed optically thick, many are not. For instance, the black lines in Figure 4 show that T and R estimated using $\omega_{R_{\infty}}^*$ are as inaccurate as using thin averaging for this particular cloud. In addition, this approach allows to match the reflectance of optically thick clouds, but not their transmittance, a quantity that is also of interest in our study. In order to generalize this strategy to transmittance and to any optical thickness, various expressions for ω^* are derived, based on the inversion of Equations A2 or A1 for various optical thicknesses ($\tau = 1, 10$ and 20). These 6 new methods are noted T_1, T_{10}, T_{20} and R_1, R_{10}, R_{20} . These parameterizations can be formally written as:

$$\omega_{X_{\tau}}^* = \omega \quad \text{such that} \quad X(\omega, \bar{g}, \bar{\tau}) = \overline{X(\omega(\lambda), g(\lambda), \tau(\lambda))}, \quad (18)$$

where X can be either R or T , and $\overline{\quad}$ indicates thin averaging. It is worth noting that Ritter and Geleyn (1992) have suggested an approach somehow similar to the transmittance-based methods (T_1, T_{10}, T_{20}). They searched an ω which would provide accurate fluxes below clouds of various optical thicknesses. However in their computations, multiple scattering was ignored. Fouquart and Bonnel (1980) also derived an empirical equation which relates $1-\omega$ to the total optical thickness of the cloud, in order to account for absorption saturation. However this sensitivity to total cloud optical thickness precludes using their parameterization within the individual layers of a cloud.

Figure 5a shows the broadband differences between the various spectral averaging methods and the reference two-stream computation for reflectance and transmittance, for clouds of various optical thicknesses. For instance, the error is 0 when the transmittance of a cloud of optical thickness 10 is computed with the parameterization T_{10} . This figure also confirms that reflectance and transmittance cannot be matched at the same time, which means that systematic errors are obtained when computing surface and TOA budgets using radiative codes with limited spectral resolution. Importantly, using thick averaging can result in significant errors even for large optical thicknesses. To clarify this, we have extended the optical thickness range and distinguished the errors related to reflectance and transmittance in Figures 5b and 5c. It can be noticed that thick averaging works well only for optical thicknesses higher than 200–300. This corresponds to extremely thick clouds, probably not representative of the majority of clouds on Earth.

To be exhaustive, the logarithmic average, used by Chou et al. (1998), was also included in the spectral averaging methods. In this case, $\bar{\omega}_{\text{log}}$ is computed as:

$$\bar{\omega}_{\text{log}} = 1 - \exp\left(\frac{\int \log(1 - \omega(\lambda))Q_{\text{ext}}(\lambda)S(\lambda)d\lambda}{\int Q_{\text{ext}}(\lambda)S(\lambda)d\lambda}\right). \quad (19)$$

The 9 above mentioned spectral averaging methods (thin, thick, logarithmic, and the 6 new methods) are applied to all the considered DSD shapes to complete the whole set of parameterizations described by Equation 6. The obtained set of ω^* parameterizations allows to estimate the impact of spectral averaging on the overall uncertainty. It is worth noting that here the spectral averages are all weighted by the incident radiation at TOA, to remain consistent with the work of Edwards and Slingo (1996) and Slingo and Schrecker (1982), and to generalize the thick averaging approach. In addition gaseous absorption was not considered in the computation of ω^* . This might not be the most accurate strategy because the solar spectrum at cloud top can differ from that at TOA as a result of

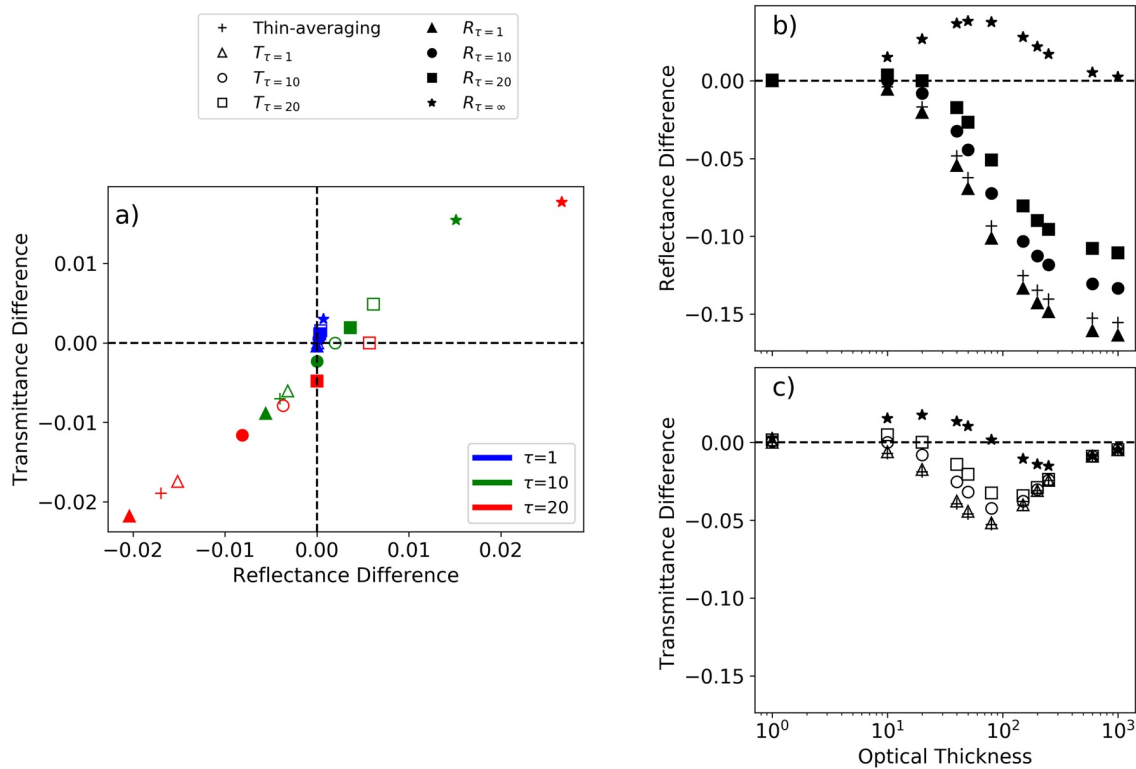


Figure 5. Differences in broadband SW (0.2–4 μm) transmittance and reflectance between the reference two-stream values and the quantities computed with various spectral averages of ω . These are calculated for a droplet size distribution with $r_{\text{eff}} = 10 \mu\text{m}$ and $\sigma = 0.2$.

atmospheric absorption above the cloud. Also, as water vapor and cloud absorption are correlated, the averages may be biased due to an overestimation of radiation in water vapor absorption bands.

To resolve this issue, several strategies were proposed in the literature. Lu et al. (2011) used a correlated k -distribution approach consistent with what is done for the gases to derive cloud absorption. They demonstrated that their method can moderate the 30% error on heating rates obtained with the thin averaged $1-\omega$, relative to line-by-line calculations. However the contribution of considering the correlation between water vapor and droplet scattering, compared to that of the higher spectral resolution, is not quantified. In addition, they have used the average spectrum at 500 hPa to derive the average $1-\omega$. Although Dobbie et al. (1999) showed that using the typical spectrum at 500 hPa in Equations 10–12 did not change their calculations of the band mean SSPs, this could still contribute to the differences. The parameterization of Fouquart and Bonnel (1980) includes the contribution of a constant amount of water vapor in the cloud, since their parameterization was derived for a stratus cloud in the presence of an atmosphere. Räisänen (1999) proposed an exhaustive method to derive $1-\bar{\omega}$ that not only accounts for the absorption of water vapor above the cloud, but also considers if other clouds are present above the evaluated cloud. Such strategies have not been replicated in this study because the focus is more on the uncertainties than on the absolute values. The correlation between water vapor and clouds remains a critical issue to derive the most accurate parameterizations, though.

3.3. SSPs Parameterizations in Terms of r_{eff}

Natively available SSPs parameterizations in ecRad consist of analytical expressions of SSPs in terms of r_{eff} . In order to implement the new parameterizations in ecRad, we mimic the analytical function used for the *SOCRATES* parameterization, which is based on Padé approximants (Manners, 2015). This allows straightforward inclusion of the new parameterizations in ecRad library, with minor changes to the core of the code. Once the SSPs have been computed for 80 individual r_{eff} in the range 1–50 μm for eight DSD shapes and nine spectral methods, they are fitted with the following functions:

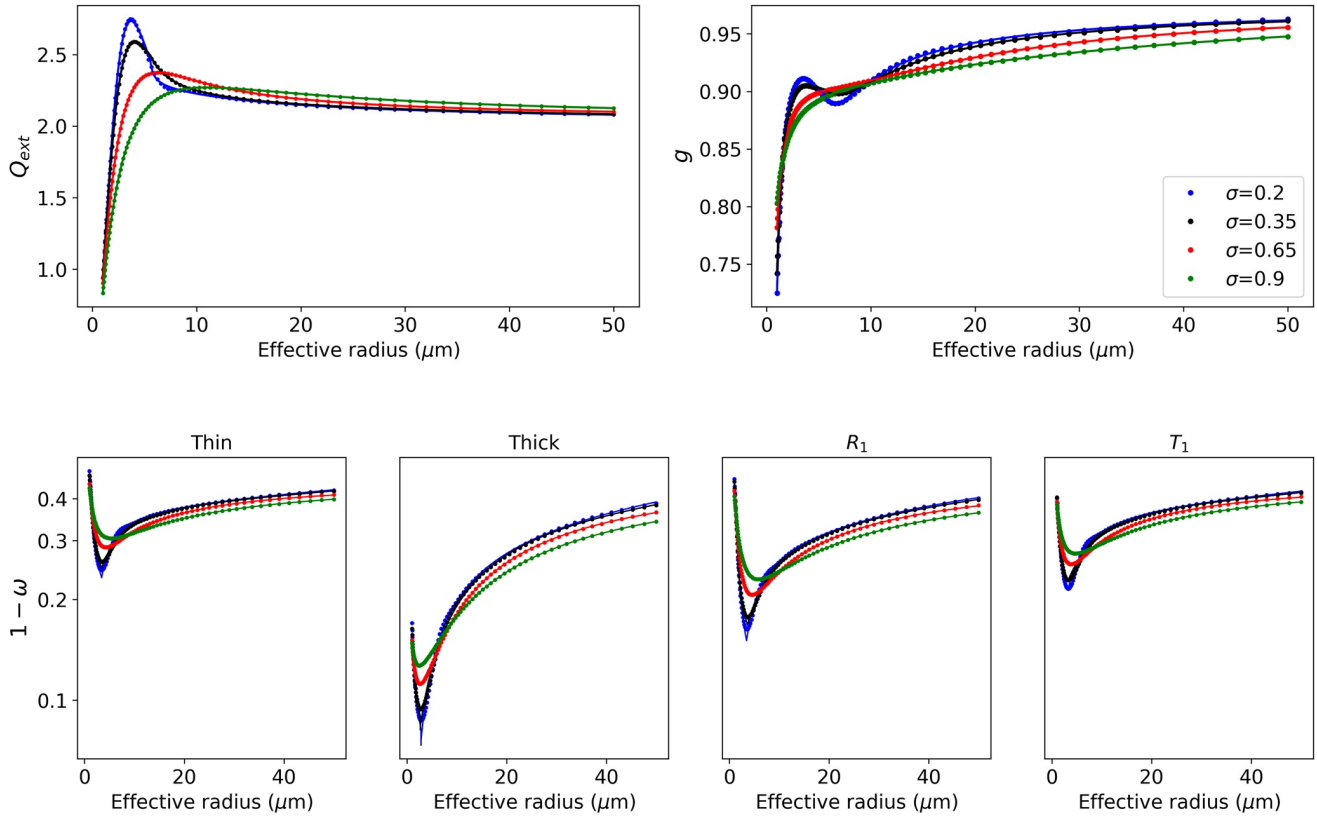


Figure 6. Single scattering properties of the 2.15–2.5 μm band in terms of r_{eff} , computed for various droplet size distributions (DSDs). The dots are the reference single scattering properties obtained from Lorenz-Mie calculations and the lines correspond to the fitted analytical functions. The colors depict four distinct lognormal DSDs. Each column in the lower row shows the single scattering albedo calculated with a different spectral method.

$$Q_{\text{ext}} = \frac{4}{3} \left(\frac{P_1 r_{\text{eff}} + P_2 r_{\text{eff}}^2 + P_3 r_{\text{eff}}^3}{1 + P_4 r_{\text{eff}} + P_5 r_{\text{eff}}^2 + P_6 r_{\text{eff}}^3} \right), \quad (20)$$

$$\ln(1 - \omega) = \ln \left(\frac{P_7 + P_8 r_{\text{eff}} + P_9 r_{\text{eff}}^2}{1 + P_{10} r_{\text{eff}} + P_{11} r_{\text{eff}}^2} \right), \quad (21)$$

$$g = \frac{P_{12} + P_{13} r_{\text{eff}} + P_{14} r_{\text{eff}}^2}{1 + P_{15} r_{\text{eff}} + P_{16} r_{\text{eff}}^2}. \quad (22)$$

The main difference with *SOCRATES* parameterization is the fact that two distinct fits are applied (the reference SSPs calculated with the Lorenz-Mie theory are shown with the dots in Figure 6) while ensuring continuity at the junction. This follows the strategy of Hu and Stamnes (1993) who separated their fits in three size ranges. This means that a total of 32 parameters are needed to describe the variations of SSPs with r_{eff} . This strategy ensures that the oscillations for small r_{eff} are well captured (see Figure 6), which would not be possible with a single term. It also prevents the function to diverge at small r_{eff} as occurs for *SOCRATES*. Hence for each new parameterization a cut-point is provided that splits the fits into two. This cut-point was derived empirically for each spectral band. For Q_{ext} and g , the cut-point is set such that $r_{\text{eff}}/\lambda_{\text{center}} = 2$ (where λ_{center} denotes the central wavelength of the spectral band), which is approximately where the oscillations take place. However the latter constant does not work as well for $1 - \omega$. Thus the local minima of the $1 - \omega$ curves (Figure 6 lower row) were selected as cut-points. Figure 6 shows an example of these two-part fits on the 2.15–2.5 μm band. It highlights that the strongest sensitivity to DSD is obtained for effective radii smaller than 10 μm . The differences can reach 50% for $1 - \omega$ and 25% for Q_{ext} . Finally, the obtained coefficients are introduced in ecRad in the form of a new netCDF file containing 33 values per spectral band (32 fit parameters and the cut-point value).

3.4. Configuration of ecRad

ecRad is a modular radiative scheme for SW and LW radiative fluxes computations, dedicated to atmospheric models. It was developed for the Integrated Forecasting System, the weather forecast model used operationally by the European Centre for Medium Range Weather Forecasts (ECMWF). In this paper its offline version is used (freely available for research use at <https://github.com/ecmwf/ecrad/tree/master/ifs>). The main inputs of this radiative code are the atmospheric profile (including aerosols and trace gas concentrations), the surface albedo and temperature, the solar zenith angle and TOA incident broadband irradiance. Note that in this study the simulations were performed without aerosols. The ozone profile in the ideal case corresponds to that of the I3RC experiment (detailed in Section 4.1) while for the real cases it comes from the US67 standard atmosphere. In the SW region, ecRad deals with 14 spectral bands, corresponding to those of RRTM (Mlawer et al., 1997; Morcrette et al., 2008). The new cloud SSPs have been computed on the same bands with the previously detailed parameterizations and were added to ecRad library. ecRad offers several options to solve the radiative transfer equation. In the present study, the McICA solver (Pincus et al., 2003) is used. The surface albedo is set to 0.2 and the fractional subgrid standard deviation of LWP is set to 0.75 (Ahlgriem et al., 2018). The simulations are performed for a solar zenith angle of 40°. The downwelling solar irradiance at the top of atmosphere is set to 1366 W m⁻².

4. Results

The newly developed parameterizations are now used to investigate how limited knowledge of the DSD shape impacts the estimation of CRE. The parameterizations are thus applied to various 1D cloudy profiles and the focus is on the energy transmitted below the cloud, reflected at the top of the cloud, and absorbed within the cloud. The profiles comprise an ideal profile based on the I3RC reference profile (Cahalan et al., 2005), and more realistic cases derived from horizontally averaged 3D fields of large eddy simulations (LES) performed with the Meso-NH research model (Lac et al., 2018). Finally ecRad was applied to outputs of the climate model CNRM-CM6-1 (Roehrig et al., 2020; Voltaire et al., 2019) to compute CRE. The DSD shape impact is assessed for all cases both in terms of *SSP-uncertainty* and *r_{eff}-uncertainty*.

4.1. Ideal Case

The goal of this ideal case is to explore a variety of LWC in order to assess the impact of the DSD assumption on simulated cloud bulk radiative properties. The input profile is based on the I3RC cloud, which extends between 1,000 and 2,400 m. The total number concentration of cloud droplets is set to 200 cm⁻³. *r_{eff}* is computed from Equation 5. The simulations are carried out with all the new parameterizations, ensuring that the value of *k* in Equation 5 is consistent with the DSD shape of the SSPs parameterization. The fluxes reflected at the top of the cloud, transmitted through the cloud layer, and absorbed in cloud, are computed with ecRad. The simulations were performed for 100 values of LWC in the range 0.02–1 g m⁻³, which corresponds to LWP ranging from 0.028 to 1.4 kg m⁻². The results of these experiments are shown in Figure 7.

For nearly all bulk radiative properties the envelope of the lognormal parameterizations is wider than that of the modified gamma. The spread for transmitted energy at cloud base, reflected energy at cloud top and absorbed energy in the lognormal case rises up to 141, 147 and 14 W m⁻² respectively (these maximal differences correspond to the lowest values of LWC for reflectance and transmittance and to the highest value of LWC in the absorptance case) while the counterpart values for the modified gamma are 91, 96 and 10 W m⁻². In the following, the uncertainties will be assessed using only the lognormal DSDs with $\sigma = 0.2$ and $\sigma = 0.65$, which roughly corresponds to the 5th and 95th percentiles of the values reported by Miles et al. (2000). To quantify the impact of spectral averaging, simulations were run with a lognormal DSD ($\sigma = 0.2$), with all available spectral averaging methods. Figure 8 shows the radiative properties calculated with 6 methods (T_1 , R_1 , R_{10} , T_{10} , thick averaging R_∞ and logarithmic), in terms of the differences with respect to thin averaging.

The range observed in absorbed energy (8 W m⁻²) is more significant than that of reflectance and transmittance (6 and 2.5 W m⁻², respectively). This is expected because the spectral averaging method mostly affects cloud absorption via $1-\omega$, but not cloud optical thickness which is the main driver of cloud transmittance and reflectance. This is in agreement with the results of Edwards and Slingo (1996). For their 24 band model, which is similar to ecRad spectral resolution, they reported differences of 8 and 6 W m⁻² in absorbed energy for an optically thin ($\tau = 10$) and thick ($\tau = 100$) cloud, respectively, between the thin and thick averaging methods.

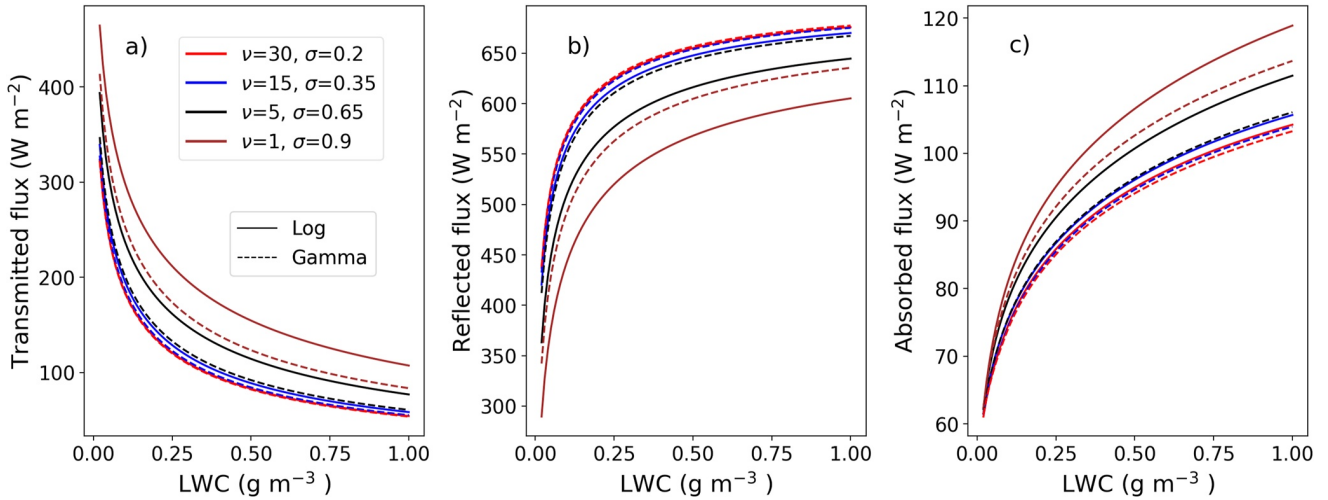


Figure 7. Bulk radiative properties of the ideal cloud as a function of liquid water content (LWC), computed for lognormal (full lines) and modified gamma (dashed-line) distributions using thin spectral averaging. As the cloud geometrical thickness is fixed, increasing the LWC implies increasing the LWP.

T_1 and R_1 methods are close to thin averaging results and become closer as LWC increases. Another noticeable trend is that the thick averaging and logarithmic methods significantly diverge from thin averaging, as LWC—and consequently cloud optical thickness—increases. Conversely, for the lower optical thicknesses all spectral methods are relatively close. This is because differences in absorption and scattering are not enhanced by multiple scattering in thin clouds.

In Figure 7 the same DSD shapes were used for r_{eff} diagnostic and SSP parameterization. However, each of these two steps generate their own uncertainty. In order to quantify the contribution of each step to the overall uncertainty, two additional simulations were performed:

1. Two DSDs with $\sigma = 0.2$ and $\sigma = 0.65$ are used for the SSP parameterization while r_{eff} is estimated using the k value of 0.67, which corresponds to the recommendation of Martin et al. (1994) for continental clouds and is close to the value corresponding to $\sigma = 0.35$ (Figure 1).

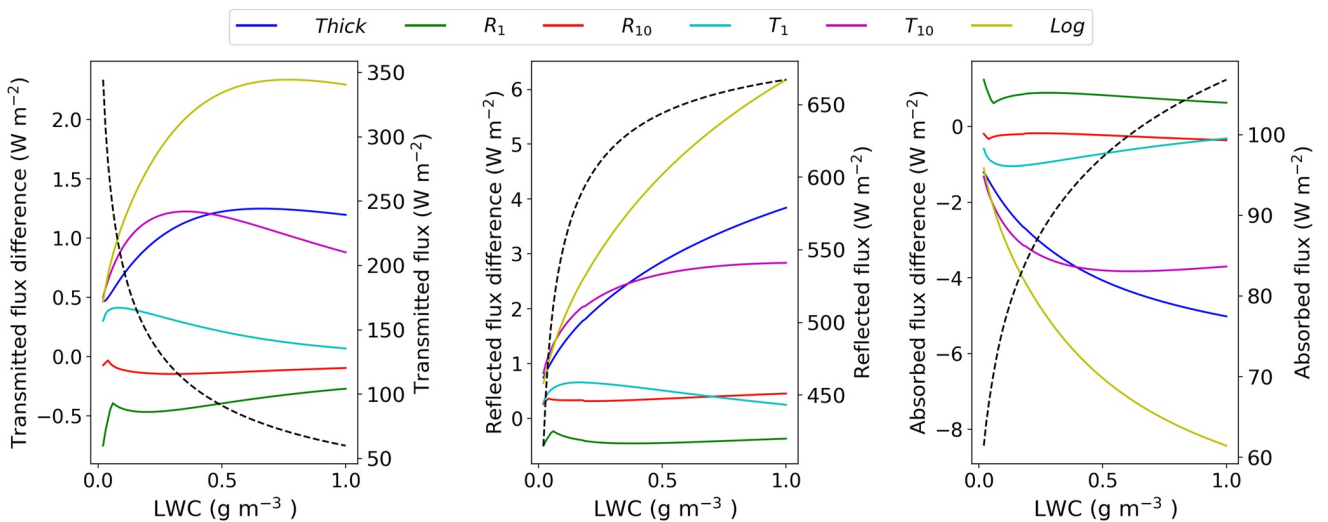


Figure 8. Differences (with respect to thin averaging) in bulk radiative properties of the ideal cloud as a function of liquid water content, for various spectral averaging methods (thick, logarithmic, R_1 , R_{10} , T_1 and T_{10}), calculated only for lognormal droplet size distribution of $\sigma = 0.2$. The dashed black lines show the bulk radiative properties calculated using the thin averaging method (right y-axis).

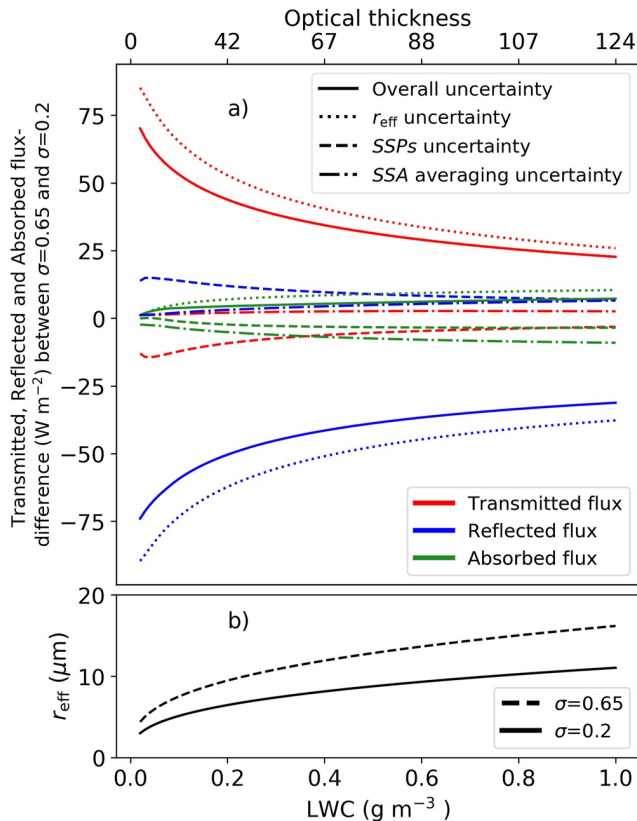


Figure 9. (a) Overall droplet size distribution-related bulk radiative properties uncertainty (solid lines), r_{eff} -uncertainty (dotted lines), SSP-uncertainty (dashed lines) as a function of liquid water content ($g m^{-3}$), all being calculated with the thin averaging method. The uncertainties related to the spectral averaging method are shown with dashed-dotted lines, for $\sigma = 0.2$. Red, blue and green colors depict the uncertainties in transmitted, reflected and absorbed flux, respectively. The upper x-axis shows the equivalence of lower axis in terms of optical thickness calculated using Equations 5 and 16, with $k = 0.67$. (b) Variations of r_{eff} with LWC for $\sigma = 0.2$ and $\sigma = 0.65$.

the 3D output fields, the quantities are averaged over the domain, including only cloudy columns (columns where at least one layer has a LWC larger than $10^{-6} kg kg^{-1}$). The cloud fraction is then set to 1 for all cloudy grids. The value of N is fixed at $200 cm^{-3}$. The following provides specific details for each simulation.

4.2.1.1. Fog

This is a simulation of a fog event observed at Cardington (UK) on the night of 24–25 November 2014 during the Local and Non-local Fog Experiment (LANFEX, Price et al., 2018). This is a typical case of radiative fog forming in a nocturnal stable boundary layer and developing over several hours into an optically thick fog. An intercomparison exercise was built on this case, involving LES and single column model simulations from different models. The vertical profile used in this study comes from a simulation using the 2-moment microphysical scheme LIMA (Vié et al., 2016) with a typical aerosol population for Cardington (3MOD experiment described in Ducongé, 2019). The transition to a thick fog occurs a bit too fast and the fog top height is overestimated compared to observations, but the vertical distributions of LWC and N are in good agreement with observations, with maximum values found near the top of the fog layer. Note that the N value computed by LIMA is not used in our 1D simulations. The optical thickness of the fog is about 3.

2. r_{eff} is estimated assuming distinct k values corresponding to the above mentioned σ , but the SSP parameterization is the same, corresponding to $\sigma = 0.35$.

These configurations are used to simulate the bulk radiative properties of the ideal cloud, using only thin averaging. The differences between bulk radiative properties obtained in all configurations are shown in Figure 9a. Dashed lines highlight the SSP-uncertainty and the dotted lines highlight the r_{eff} -uncertainty. The solid lines show the overall differences when the DSD shape is consistent throughout both steps. The overall differences in transmitted and reflected fluxes reach 70 and 74 $W m^{-2}$. The corresponding surface and top of the cloud fluxes equal 323 and 437 $W m^{-2}$ for $\sigma = 0.2$. Figure 9 also shows that the r_{eff} -uncertainty dominates over the SSP-uncertainty. Interestingly, the SSP-uncertainty slightly offsets (by about 20%) the r_{eff} -uncertainty. Maximum uncertainties of 89, 85 and 10 $W m^{-2}$ in reflected, transmitted and absorbed fluxes due to the r_{eff} -uncertainty are indeed compensated by 15, 14 and 3.5 $W m^{-2}$ uncertainties due to the SSP-uncertainty. Looking at the effective radii corresponding to the investigated range of LWC in Figure 9b, it can be deduced that the r_{eff} -uncertainty results from a nearly 50% increase of the effective radius when σ changes from 0.2 to 0.65.

To highlight the effect of spectral averaging, the dash-dotted lines in Figure 9 show the differences between two extreme methods, namely the R_1 and logarithmic methods. In this case both steps relied on the lognormal DSD with $\sigma = 0.2$. It confirms that the absorption is more sensitive to the spectral averaging uncertainty than reflectance and transmittance.

Based on the above results, only two extreme spectral averaging methods are selected to estimate uncertainties in the next sections.

4.2. Real Cases

Four LES simulations were used to construct the realistic 1D profiles used in this section. They are presented, along with the methodology to convert 3D outputs into 1D profiles. Then the results of ecRad simulations are discussed. The profiles of LWC are shown in Figure 10.

4.2.1. Description of the Cases

The 4 reference cases have been simulated with the Meso-NH model. To extract 1D profiles of temperature, pressure, relative humidity and LWC from

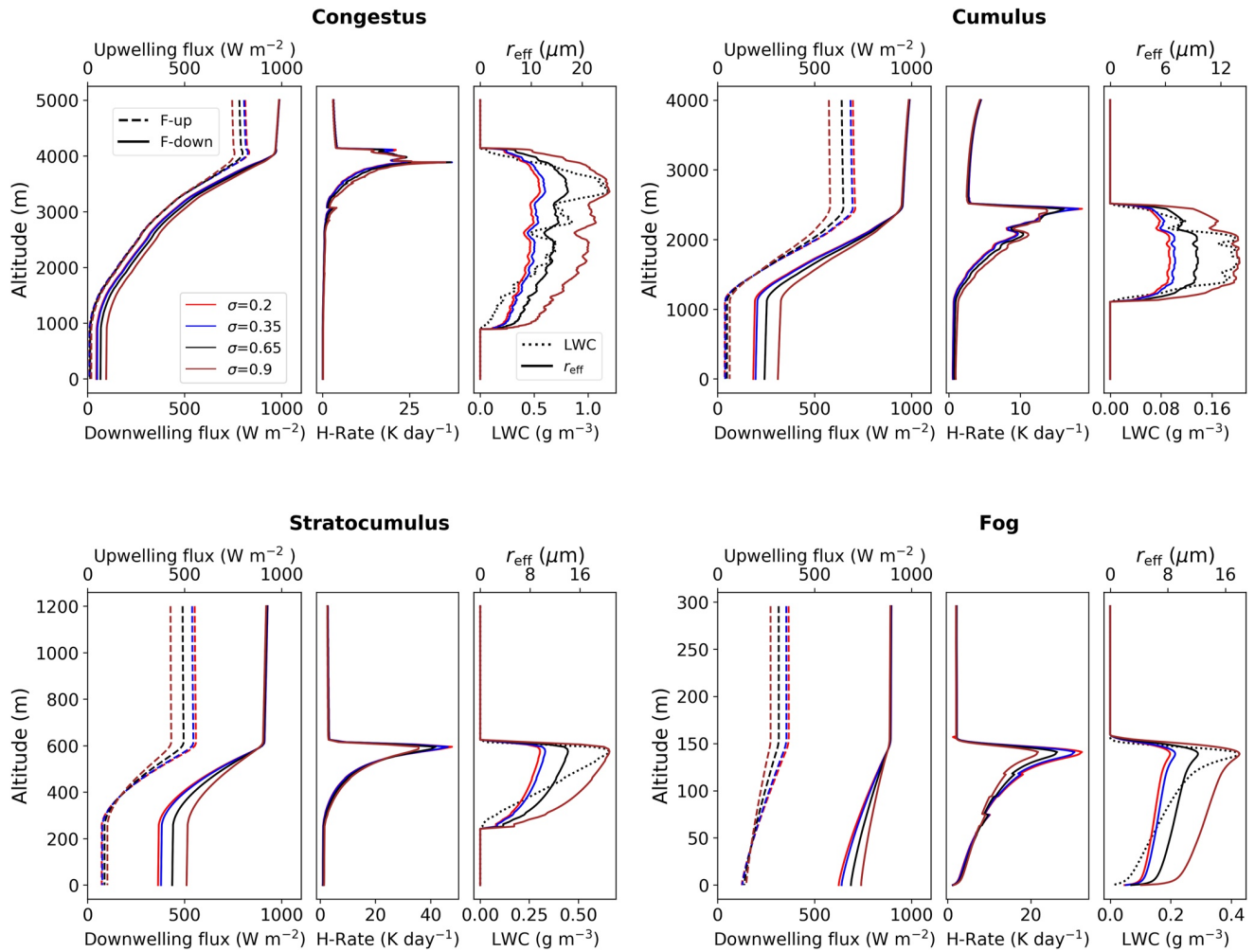


Figure 10. For each large eddy simulation (congestus, cumulus, stratocumulus and fog), from left to right, shortwave radiative fluxes, heating rates and effective radii profiles, calculated for the lognormal droplet size distributions with $\sigma = \{0.2, 0.35, 0.65, 0.9\}$ (shown with different colors). The black dotted lines in the right panel shows the liquid water content profile.

4.2.1.2. Stratocumulus

This is a simulation of a stratocumulus based on the First International Satellite Cloud Climatology Project Regional Experiment model intercomparison study (Duykerke et al., 2004), inspired from observations above the Pacific Ocean, off the coast of California, acquired in July 1987. The LES simulation used here is detailed in Briant et al. (2019) and the profiles provided to ecRad are extracted from the simulation during nighttime at a time of maximum vertical extension of the stratocumulus. The optical thickness of this cloud is about 8.

4.2.1.3. Cumulus

This is a simulation of continental shallow cumulus based on the ARMCU model intercomparison study (Brown et al., 2002) inspired from observations on 21 June 1997 at the Southern Great Plains site of the Atmospheric Radiation Measurement. This case corresponds to a diurnal cycle of shallow convection and the profiles provided to ecRad were extracted after 9 hr of simulation, the time of maximum development of the shallow clouds. The optical thickness of the cumulus is close to 20.

4.2.1.4. Congestus

This is a simulation of a congestus cloud in growing phase simulated at very high-resolution (5 m) (Strauss, 2020). This simulation was nested around a selected congestus cloud from a 50 m-resolution simulation of a population of clouds. The optical thickness of this congestus is around 100.

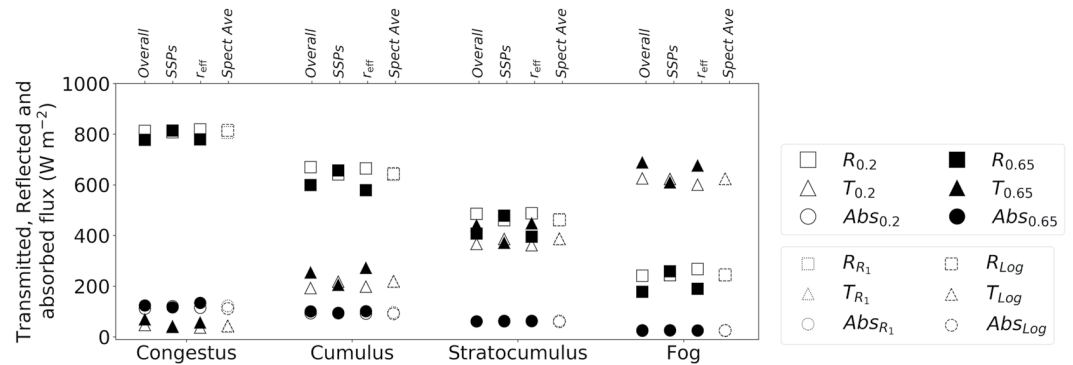


Figure 11. Bulk radiative properties of the 4 real cases calculated using two droplet size distribution shapes of $\sigma = 0.2$ and $\sigma = 0.65$. First column: consistently in both r_{eff} and single scattering properties (SSPs) parameterizations. Second column: only in SSPs parameterization (using r_{eff} computed with $\sigma = 0.35$). Third column: only in r_{eff} estimation (using the $\sigma = 0.35$ in SSPs parameterization). Fourth column: radiative properties obtained with the two extreme spectral averaging methods, with $\sigma = 0.2$.

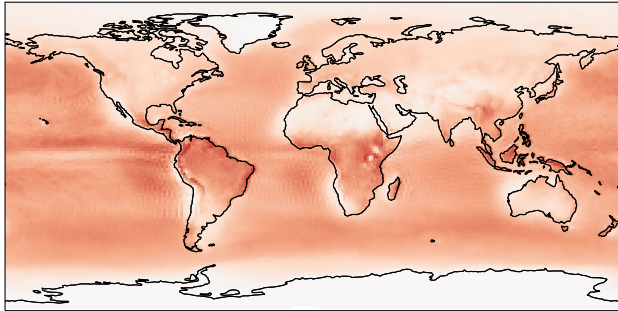
4.2.2. Results of Simulations

ecRad was applied to the 1D profiles, completed above the simulation domain with the US67 standard atmospheric profile up to 80 km. The simulations were performed with the 4 lognormal DSD shapes, again restricting to thin averaging. Figure 10 depicts the upwelling (dashed lines) and downwelling (solid lines) fluxes, hereafter called F_i^\uparrow and F_i^\downarrow , where i indicates the corresponding DSD shape (σ value). The cloud boundaries can be deduced from the LWC profiles shown in black dotted lines in the third panel of each case. Generally it can be seen that the cloud with DSD shape of $\sigma = 0.2$ is more opaque than that of $\sigma > 0.2$. This can be explained by looking at the effective radius profiles on the third panel (solid color lines). For example, for any cloudy layer in our model, the effective radius for a DSD with $\sigma = 0.65$ is about 50% larger than that of $\sigma = 0.2$. According to Equation 16 the optical thickness will be larger for $\sigma = 0.2$, resulting in larger reflectance and lower transmittance. This explains why $F_{0.2}^\downarrow$ at the surface ($F_{0.2}^\uparrow$ at the top) is smaller (greater) than $F_{0.65}^\downarrow$ ($F_{0.65}^\uparrow$). In addition to the fluxes, the heating rates are also displayed to highlight differences in atmospheric absorption. It suggests that changing the DSD shape from $\sigma = 0.2$ to $\sigma = 0.65$ can alter the heating rates from 1% in the cumulus case (higher optical thickness) up to 17% in the fog case (lower optical thickness).

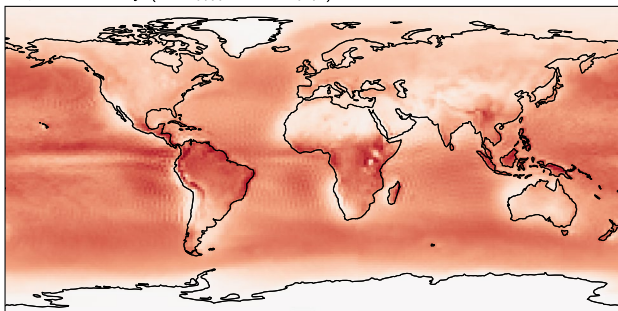
As for the ideal case, we distinguish the contributions of r_{eff} -uncertainty and SSP-uncertainty. For each real case, switching between $\sigma = 0.2$ and $\sigma = 0.65$ produces distinct results in terms of bulk radiative properties, illustrated with filled and empty geometrical shapes in Figure 11. The difference between identical filled and empty shapes for each case demonstrates the overall DSD-related uncertainty in the first column, the SSP-uncertainty in second, and r_{eff} -uncertainty in the third column. The uncertainty due to the DSD shape can reach 80 W m^{-2} on transmitted/reflected fluxes for the fog and stratocumulus cases having LWP amounts of 0.028 and 0.12 kg m^{-2} , respectively. For the cumulus and congestus cases where the liquid water path reaches 0.19 and 1.8 kg m^{-2} , respectively, lower differences are obtained for transmitted and reflected fluxes. It must be noted that while cumulus and stratocumulus clouds have close values of LWP, they differ significantly in terms of bulk radiative properties. This is due to the lower values of LWC in cumulus, which results in a greater optical thickness (see Equations 5 and 16).

Similarly to the ideal case results, it is observed that SSP-uncertainty partly offsets the r_{eff} -uncertainty on reflected, transmitted and absorbed fluxes by 17%, 13% and 22% for the congestus case. Approximately similar results are obtained for the cumulus case. In the fog and stratocumulus cases the offset reaches 20% and 19% for reflected and transmitted fluxes. Regarding absorption, SSP-uncertainty amplifies r_{eff} -uncertainty in the fog case (not visible in the figure), while it nearly offsets it in the stratocumulus case. Note however that absorption in these two cases is negligible.

Overall uncertainty ($CRE_{065065} - CRE_{0202}$) - Mean difference = 6.2 W m^{-2}



r_{eff} uncertainty ($CRE_{06502} - CRE_{0202}$) - Mean difference = 7.8 W m^{-2}



SSP uncertainty ($CRE_{065065} - CRE_{06502}$) - Mean difference = -1.6 W m^{-2}

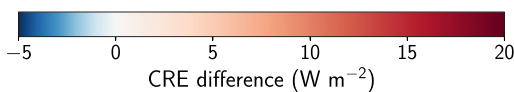
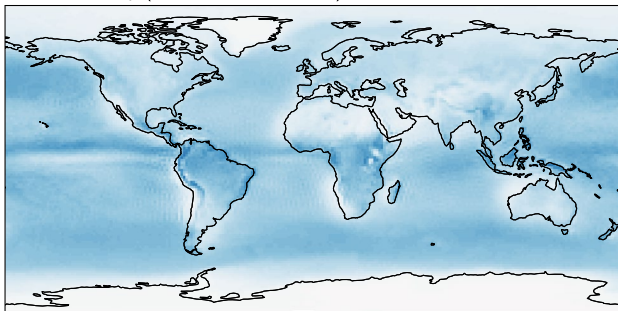


Figure 12. Global difference maps of the 2000–2004 average cloud radiative effect (CRE) computed from outputs of the CNRM-CM6-1 *amip* simulation for various choices of cloud single scattering properties (SSPs) and r_{eff} parameterizations. The subscripts of CRE in the titles indicate the configurations that are compared. CRE_{06502} means that k corresponding to the lognormal distribution with $\sigma = 0.65$ was used to estimate r_{eff} from the GCM LWC, and that the SSPs corresponding to the lognormal distribution with $\sigma = 0.2$ were then used.

4.3. GCM Outputs

As outlined in the introduction, CRE is a key quantity of the climate system that GCMs should correctly simulate. Although most GCMs reasonably reproduce observed SW CRE, it is such because models are tuned to match as closely as possible the observed radiative budget and SW CRE in order to avoid any drift in long-term simulations. However, simulated CRE remains very sensitive to the way clouds are treated by the radiative code. Here, the sensitivity of CRE to the parameterization of SSPs and effective radius is investigated. To this end, outputs of the CNRM-CM6-1 model are used as inputs to ecRad. TOA and surface SW fluxes in cloudy and clear-sky conditions are computed from 3-hourly full fields of the forced historical simulation *amip* (Eyring et al., 2016) performed for CMIP6 for the period 2000–2004. CRE is averaged over 5 years to compute CRE global maps, that are compared for various parameterizations, as well as their global averages. The exponential-exponential cloud overlap assumption is used in ecRad. N is computed as in Martin et al. (1994) from fixed values of cloud condensation nuclei set to 900 cm^{-3} over land and 150 cm^{-3} over sea. The effective radius is then estimated from Equation 5 with k corresponding either to $\sigma = 0.2$ or $\sigma = 0.65$. The SSPs corresponding to these two distributions are then used for both choices of k . Hence four simulations are performed. As previously this approach allows to split the r_{eff} and SSP uncertainties by comparing simulations with similar k values but different SSPs on the one hand, and distinct k but identical SSPs on the other hand. Simulations are also performed, where SSPs are consistent with k .

Figure 12 shows maps of the TOA SW CRE differences. The top panel shows the difference between the fully consistent simulations with $\sigma = 0.65$ and $\sigma = 0.2$. Differences up to 15 W m^{-2} are found in the Tropics, where low clouds dominate, and the global average differs by 6.2 W m^{-2} . The middle panel shows the r_{eff} - uncertainty, assuming $\sigma = 0.65$ or $\sigma = 0.2$ in Equation 5 while using only the SSPs corresponding to $\sigma = 0.2$. Differences up to 18 W m^{-2} are found in the Tropics, and the global average differs by 7.8 W m^{-2} . The bottom panel shows SSP-uncertainty, using the SSPs corresponding to $\sigma = 0.65$ and $\sigma = 0.2$ while using the same k corresponding to $\sigma = 0.65$. The differences do not exceed -4 W m^{-2} and the global averages differ by -1.6 W m^{-2} . Note that these differences are approximately twice larger if the more extreme value $\sigma = 0.9$ is used instead of $\sigma = 0.65$. As expected, as k decreases with σ , a wider DSD (i.e., larger σ) results in clouds with larger r_{eff} hence lower reflectance and less negative TOA CRE. On the contrary, for a given r_{eff} using the SSPs of a wider DSD intensifies the CRE. Although this second effect is one order of magnitude less than r_{eff} impact it partially offsets the main impact. It is worth comparing these numbers to the observed CRE value (-47.7 W m^{-2}) and to the range of CRE simulated by CMIP6 participating models (spread of 19.2 W m^{-2} and standard deviation of 3.6 W m^{-2}). This highlights that the impact of DSD shape is far from being negligible, and that the underlying assumptions made in different GCMs should not be overlooked when investigating differences in CRE. It also suggests that changing the underlying hypothesis on the DSD in a GCM could significantly alter its

radiative budget, and consequently the tuning required to match observations. The same maps were computed for the surface and atmospheric CRE (not shown). For the surface, the global differences are very similar (6.3 , 7.8 and -1.5 W m^{-2} for the overall, r_{eff} and SSP uncertainties, respectively). For the atmospheric CRE, which is slightly positive (between 4 and 7 W m^{-2} according to Wild, 2020), the differences are of the order of 0.1 W m^{-2} , but it is worth noting that most of it is due to the choice of SSPs.

5. Conclusion and Discussion

Shortwave bulk radiative properties of liquid clouds (transmittance, reflectance and absorptance) critically depend on their optical properties at the droplet scale. The derivation of these properties in atmospheric models generally involves two steps: (a) estimating the DSD effective radius (r_{eff}) and (b) estimating the SSPs from r_{eff} . SSPs are modulated by the DSD and the frequency of incident light, two quantities that are not fully resolved in GCMs. Indeed, LWC is generally the single prognostic cloud property provided by cloud schemes and the embedded radiative code has a limited spectral resolution. For these reasons, estimating cloud optical properties implies making an assumption on the DSD and finding strategies to average the SSPs over spectral bands. This generally results in SSPs parameterizations in terms of r_{eff} for each band. This study aimed at estimating the impact of the aforementioned assumptions on the simulated SW CRE, the latter being a key characteristic of Earth climate, showing however a significant variability across GCMs. To this end we developed a new set of SSPs parameterizations that explicitly account for the shape of the DSD and cover a variety of spectral averaging methods. These parameterizations were implemented in the radiative code ecRad and offline simulations were performed on a variety of 1D cloud profiles, including idealized profiles, profiles obtained from LES and outputs from a GCM. Our results show that the assumption on the DSD significantly alters the simulated fluxes at the surface and TOA, up to several tens of W m^{-2} . Atmospheric absorption and heating rates are also affected in the case of optically thick clouds. This implies that care should be taken in DSD shape assumptions when studying the radiative impact of liquid clouds.

To quantify the uncertainty associated with the choice of the DSD, the estimation of r_{eff} and the SSPs computation were distinguished. Over the variety of clouds analyzed in this study, the r_{eff} -uncertainty dominates the uncertainty. The *SSP-uncertainty*, which is about five times smaller, tends to counteract the r_{eff} -uncertainty. The uncertainty resulting from spectral averaging is substantially lower but still impacts absorption, especially in clouds with large liquid water paths (LWP). This is expected as spectral averaging only impacts the estimation of the single scattering co-albedo which quantifies absorption. Note however that the radiative code used in this study has 14 bands in the SW, so that larger spectral averaging errors are expected for radiative codes with fewer bands. When applied to global outputs of a GCM, the parameterizations revealed that the SW CRE can vary by 6.2 W m^{-2} depending on the assumed DSD, which is about 13% of the measured SW CRE, with local differences up to 15 W m^{-2} over the Tropics where low clouds are ubiquitous. These differences are primarily due to the 50% difference in the estimation of r_{eff} obtained when using distinct values of k in Equation 5.

In most atmospheric models, the estimation of r_{eff} , a quantity that is only used in the radiative code, is made independently of the assumptions made in the microphysical scheme. Likewise the DSD from which SSPs parameterizations were derived is distinct from the previous ones. Our results emphasize the importance of using a consistent DSD throughout the microphysical and radiative schemes, which is practically rarely the case. Several studies have already underlined the importance of using the same DSD in the microphysical and radiative schemes. Improvements in surface radiation, precipitation and temperature were thus reported as a result of such consistent simulations with WRF (Bae et al., 2016; Thompson et al., 2016). Sieron et al. (2017) also showed that ensuring consistency altered the satellite radiances simulated from WRF model outputs. Positive impacts on temperature and CRE were also reported for the Met Office Unified Model Global Atmosphere 5.0 (GR5) (Baran et al., 2014). We are currently working on the harmonization of microphysical and radiative schemes in the Meso-NH model, which will be the focus of a future study.

This study confirms that r_{eff} is a key property and drives cloud radiative forcing. r_{eff} as an indicator of droplet size, greatly depends on the number concentration of droplets N , which itself depends on the amount of cloud condensation nuclei. In the past, many studies focused on the relation between N and r_{eff} , in particular when investigating the indirect aerosol effect through the so-called Twomey effect (Twomey, 1974). Increased levels of aerosols tend to increase N , hence to reduce r_{eff} , making clouds brighter and cooling the Earth system. However we have demonstrated that for a given LWC, r_{eff} also depends on the parameter k which is directly related to the DSD shape and can vary by a factor of 6 based on observations. From the introduction of this k parameter by Pontikis and Hicks (1992), many GCMs have used constant k values to describe very different clouds. For instance, $k = 0.36$ in CanAM4 (Von Salzen et al., 2013), $k = 0.75$ in the IPSL (Madeleine et al., 2020) and CNRM-CM6-1 (Roehrig et al., 2020) climate models. In ECHAM6 (Stevens et al., 2013) $k = 0.67$ over land and $k = 0.8$ over ocean, as proposed by Martin et al. (1994). It shows that the CRE computed from these models would greatly differ even if LWC and N were strictly similar. Several theoretical studies (Liu et al., 2008; Igel &

van den Heever, 2017; M. Wang et al., 2020) reported correlations between k , N , microphysical processes (e.g., autoconversion and evaporation) and dynamics (e.g., vertical velocity). They tried to quantify the radiative effect of such correlations on the indirect aerosol effect. Rotstajn and Liu (2003, 2009) and W. Zhao et al. (2018) have shown the advantages of considering such a correlation in climate models. Some observation-based studies, on the contrary, reject the general relation between N and k (Brennguier et al., 2011; Tas et al., 2015; Y. Wang et al., 2021). This overall highlights that k remains a very poorly constrained parameter which would deserve more investigation and a detailed parameterization in GCMs.

To conclude, attention must be put on two aspects. First, given the crucial importance of k in the CRE uncertainty deduced from the results of the present study, explicitly relating k to the physics of the model, instead of using a fixed value for all clouds, appears as a priority. Second, in the mentioned studies which investigated the effect of k on indirect aerosol effect, only the r_{eff} -uncertainty was considered, the SSPs-uncertainty being ignored while the present study has demonstrated its own significance. Our fully consistent parameterizations, accounting for the impact of DSD both on the estimation of r_{eff} and on the SSPs, thus provide a more robust framework for reliable studies of the indirect aerosol radiative effect. Finally it is worth bearing in mind that this study was restricted to the SW impact of liquid clouds. To have a global picture of the impact of DSD assumptions on CRE, it should be extended to ice clouds and to the longwave.

Appendix A: Two-Stream Approximation

To compute the bulk radiative properties of a cloud layer, the plane-parallel radiative transfer equation must be solved. A widely used solution, especially in fast radiative codes used in NWP and climate models, is the two-stream approximation. It can provide analytical expressions for reflectance and transmittance of the layer under diffuse and direct illumination, given the asymmetry parameter g , optical thickness τ and single scattering albedo ω . Using the δ -Eddington approximation (Joseph et al., 1976) and the approach of Aquino and Varela (2005), transmittance and reflectance for a homogeneous cloud layer can be written as:

$$T = \frac{\Gamma K_1 e^{k\tau} + K_2 e^{-k\tau} + G^- e^{-\tau/\mu_0} + F_0 \mu_0 e^{-\tau/\mu_0}}{F_0 \mu_0}, \quad (\text{A1})$$

$$R = \frac{K_1 + \Gamma K_2 + G^+}{F_0 \mu_0}, \quad (\text{A2})$$

where the spectral dependence is omitted for sake of simplicity. The irradiance impinging on the top of the cloud is denoted with $F_0 \mu_0$, μ_0 being the cosine of the solar zenith angle (θ_0). The latter expressions hence correspond to direct illumination. This avoids the unrealistic negative values which can be obtained under diffuse illumination (Wiscombe, 1977). θ_0 was fixed to 50° which corresponds to standard illumination conditions. The parameters in Equations A1 and A2 are given by:

$$K_1 = \frac{\Gamma G^- e^{-k\tau^*} - G^+ e^{-\tau^*/\mu_0}}{e^{k\tau^*} - \Gamma^2 e^{-k\tau^*}} \quad (\text{A3})$$

$$K_2 = -(G^- + \Gamma K_1) \quad (\text{A4})$$

$$G^- = \frac{\mu_0^2 \omega F_0}{(\kappa \mu_0)^2 - 1} \left[\left(\gamma_1 + \frac{1}{\mu_0} \right) \gamma_4 + \gamma_2 \gamma_3 \right] \quad (\text{A5})$$

$$G^+ = \frac{\mu_0^2 \omega F_0}{(\kappa \mu_0)^2 - 1} \left[\left(\gamma_1 - \frac{1}{\mu_0} \right) \gamma_3 + \gamma_2 \gamma_4 \right] \quad (\text{A6})$$

$$\gamma_1 = \frac{1}{4} [7 - \omega^* (4 + 3g^*)], \quad \gamma_2 = -\frac{1}{4} [1 - \omega^* (4 - 3g^*)], \quad (\text{A7})$$

$$\gamma_3 = \frac{1}{4} (2 - 3g^* \mu_0), \quad \gamma_4 = \frac{1}{4} (2 + 3g^* \mu_0), \quad (\text{A8})$$

$$\kappa = \sqrt{\gamma_1^2 - \gamma_2^2}, \quad (\text{A9})$$

$$\Gamma = \frac{\gamma_1 - \kappa}{\gamma_2}, \quad (\text{A10})$$

and * refers to the δ -scaling such that:

$$g^* = \frac{1}{g + 1}, \quad \tau^* = (1 - \omega f)\tau, \quad \omega^* = \frac{(1 - f)\omega}{1 - \omega f}. \quad (\text{A11})$$

For the development of the SSPs parameterizations, the value of τ generally corresponds to the wavelength of $0.55 \mu\text{m}$. $\tau(\lambda)$ can be computed from the extinction efficiency $Q_{\text{ext}}(\lambda)$:

$$\tau(\lambda) = \tau(0.55) \frac{Q_{\text{ext}}(\lambda)}{Q_{\text{ext}}(0.55)}. \quad (\text{A12})$$

Data Availability Statement

The parameterizations coefficients and the reference values of SSPs are available in: <https://github.com/erfanjhn/liq-cloud-opt-param.git>. The experiments of CMIP-6 CNRM-CM6-1 are made available via the portal: <https://esgf-node.llnl.gov/search/cmip6>.

Acknowledgments

We would like to thank K.P. Nielsen for providing us his parameterization coefficients. We also acknowledge C. Strauss, D. Ricard and C. Lac who realized the LES of the congestus case and L. Ducongé who realized the LES of the fog case. We are grateful to the two anonymous reviewers who provided constructive feedbacks on this work. The research leading to this work is being carried out as a part of the Smart4RES project (European Union's Horizon 2020, No. 864337). The sole responsibility of this publication lies with the authors. The European Union is not responsible for any use that may be made of the information contained therein.

References

- Ahlgrimm, M., Forbes, R. M., Hogan, R. J., & Sandu, I. (2018). Understanding global model systematic shortwave radiation errors in subtropical marine boundary layer cloud regimes. *Journal of Advances in Modeling Earth Systems*, 10(8), 2042–2060. <https://doi.org/10.1029/2018MS001346>
- Aquino, J., & Varela, J. (2005). Two stream approximation to radiative transfer equation: An alternative method of solution. *Revista Mexicana de Física*, 51, 82–86.
- Bae, S. Y., Hong, S.-Y., & Lim, K.-S. S. (2016). Coupling WRF double-moment 6-class microphysics schemes to RRTMG radiation scheme in weather research forecasting model. *Advances in Meteorology*, 2016, 1–11. <https://doi.org/10.1155/2016/5070154>
- Baran, A. J., Hill, P., Furtado, K., Field, P., & Manners, J. (2014). A coupled cloud physics–radiation parameterization of the bulk optical properties of cirrus and its impact on the Met Office Unified Model Global Atmosphere 5.0 configuration. *Journal of Climate*, 27(20), 7725–7752. <https://doi.org/10.1175/JCLI-D-13-00700.1>
- Barker, H. W., Cole, J. N. S., Li, J., & von Salzen, K. (2016). A parametrization of 3-D subgrid-scale clouds for conventional GCMs: Assessment using A-Train satellite data and solar radiative transfer characteristics. *Journal of Advances in Modeling Earth Systems*, 8(2), 566–597. <https://doi.org/10.1002/2015MS000601>
- Barker, H. W., Pincus, R., & Morcrette, J. J. (2002). The Monte Carlo independent column approximation: Application within large-scale models. In *Proceedings of the gcss/arm workshop on the representation of cloud systems in large-scale models*.
- Baum, B. A., Yang, P., Heymsfield, A. J., Schmitt, C. G., Xie, Y., Bansemmer, A., & Zhang, Z. (2011). Improvements in shortwave bulk scattering and absorption models for the remote sensing of ice clouds. *Journal of Applied Meteorology and Climatology*, 50(5), 1037–1056. <https://doi.org/10.1175/2010JAMC2608.1>
- Boucher, O., & Lohmann, U. (1995). The sulfate-CCN-cloud albedo effect. *Tellus B: Chemical and Physical Meteorology*, 47(3), 281–300. <https://doi.org/10.1034/j.1600-0889.47.issue3.1.x>
- Brenguier, J. L., Burnet, F., & Geoffroy, O. (2011). Cloud optical thickness and liquid water path—does the k coefficient vary with droplet concentration? *Atmospheric Chemistry and Physics*, 11(18), 9771–9786. <https://doi.org/10.5194/acp-11-9771-2011>
- Brenguier, J.-L., Pawlowska, H., Schüller, L., Preusker, R., Fischer, J., & Fouquart, Y. (2000). Radiative properties of boundary layer clouds: Droplet effective radius versus number concentration. *Journal of the Atmospheric Sciences*, 57(6), 803–821. [https://doi.org/10.1175/1520-0469\(2000\)057<0803:RPOBLC>2.0.CO;2](https://doi.org/10.1175/1520-0469(2000)057<0803:RPOBLC>2.0.CO;2)
- Brient, F., Couvreux, F., Villefranque, N., Rio, C., & Honnert, R. (2019). Object-oriented identification of coherent structures in large Eddy simulations: Importance of downdrafts in stratocumulus. *Geophysical Research Letters*, 46(5), 2854–2864. <https://doi.org/10.1029/2018GL081499>
- Brown, A. R., Cederwall, R. T., Chlond, A., Duynkerke, P. G., Golaz, J. C., Khairoutdinov, M., et al. (2002). Large-eddy simulation of the diurnal cycle of shallow cumulus convection over land. *Quarterly Journal of the Royal Meteorological Society*, 128, 1075–1093. <https://doi.org/10.1256/003590002320373210>
- Cahalan, R. F., Oreopoulos, L., Marshak, A., Evans, K. F., Davis, A. B., Pincus, R., et al. (2005). The 13RC: Bringing together the most advanced radiative transfer tools for cloudy atmospheres. *Bulletin of the American Meteorological Society*, 86(9), 1275–1294. <https://doi.org/10.1175/BAMS-86-9-1275>
- Charlock, T. P., & Ramanathan, V. (1985). The Albedo field and cloud radiative forcing produced by a general circulation model with internally generated cloud optics. *Journal of the Atmospheric Sciences*, 42(13), 1408–1429. [https://doi.org/10.1175/1520-0469\(1985\)042<1408:tafacr>2.0.co;2](https://doi.org/10.1175/1520-0469(1985)042<1408:tafacr>2.0.co;2)
- Chou, M.-D., Suarez, M. J., Ho, C.-H., Yan, M. M.-H., & Lee, K.-T. (1998). Parameterizations for cloud overlapping and shortwave single-scattering properties for use in general circulation and cloud ensemble models. *Journal of Climate*, 11(2), 202–214. [https://doi.org/10.1175/1520-0442\(1998\)011<0202:PF0COAS>2.0.CO;2](https://doi.org/10.1175/1520-0442(1998)011<0202:PF0COAS>2.0.CO;2)
- Clough, S. A., Shephard, M. W., Mlawer, E. J., Delamere, J. S., Iacono, M. J., Cady-Pereira, K., & Brown, P. D. (2005). Atmospheric radiative transfer modeling: A summary of the AER codes. *Journal of Quantitative Spectroscopy and Radiative Transfer*, 91(2), 233–244. <https://doi.org/10.1016/j.jqsrt.2004.05.058>
- Costa, S., & Shine, K. (2006). An estimate of the global impact of multiple scattering by clouds on outgoing long-wave radiation. *Quarterly Journal of the Royal Meteorological Society*, 132(616), 885–895. <https://doi.org/10.1256/qj.05.169>

- Di Giuseppe, F., & Tompkins, A. M. (2015). Generalizing cloud overlap treatment to include the effect of wind shear. *Journal of the Atmospheric Sciences*, 72(8), 2865–2876. <https://doi.org/10.1175/JAS-D-14-0277.1>
- Dobbie, J. S., Li, J., & Chýlek, P. (1999). Two-and four-stream optical properties for water clouds and solar wavelengths. *Journal of Geophysical Research*, 104(D2), 2067–2079. <https://doi.org/10.1029/1998jd200039>
- Ducongé, L. (2019). *Étude du cycle de vie du brouillard radiatif durant la campagne LANFEX: Impact de la dynamique en terrain vallonné et des processus microphysiques*. Unpublished doctoral dissertation. University of Toulouse.
- Dudhia, J. (1989). Numerical study of convection observed during the winter monsoon experiment using a mesoscale two-dimensional model. *Journal of the Atmospheric Sciences*, 46(20), 3077–3107. [https://doi.org/10.1175/1520-0469\(1989\)046<3077:NSOCOD>2.0.CO;2](https://doi.org/10.1175/1520-0469(1989)046<3077:NSOCOD>2.0.CO;2)
- Duynkerke, P. G., de Roode, S. R., van Zanten, M. C., Calvo, J., Cuxart, J., Cheinet, S., et al. (2004). Observations and numerical simulations of the diurnal cycle of the EUROCS stratocumulus case. *Quarterly Journal of the Royal Meteorological Society*, 130C(604), 3269–3296. <https://doi.org/10.1256/qj.03.139>
- Edwards, J. M., Havemann, S., Thelen, J.-C., & Baran, A. J. (2007). A new parametrization for the radiative properties of ice crystals: Comparison with existing schemes and impact in a GCM. *Atmospheric Research*, 83(1), 19–35. <https://doi.org/10.1016/j.atmosres.2006.03.002>
- Edwards, J. M., & Slingo, A. (1996). Studies with a flexible new radiation code. I: Choosing a configuration for a large-scale model. *Quarterly Journal of the Royal Meteorological Society*, 122(531), 689–719. <https://doi.org/10.1002/qj.49712253107>
- Engström, A., Bender, F. A., & Karlsson, J. (2014). Improved representation of marine stratocumulus cloud shortwave radiative properties in the CMIP5 climate models. *Journal of Climate*, 27(16), 6175–6188. <https://doi.org/10.1175/JCLI-D-13-00755.1>
- Espinoza, R. C., Jr. (1996). Parameterization of solar near-infrared radiative properties of cloudy layers. *Journal of the Atmospheric Sciences*, 53(11), 1559–1568. [https://doi.org/10.1175/1520-0469\(1996\)053<1559:POSNIR>2.0.CO;2](https://doi.org/10.1175/1520-0469(1996)053<1559:POSNIR>2.0.CO;2)
- Eyring, V., Bony, S., Meehl, G. A., Senior, C. A., Stevens, B., Stouffer, R. J., & Taylor, K. E. (2016). Overview of the Coupled Model Inter-comparison Project Phase 6 (CMIP6) experimental design and organization. *Geoscientific Model Development*, 9(5), 1937–1958. <https://doi.org/10.5194/gmd-9-1937-2016>
- Fouquart, Y. (1988). Radiative transfer in climate models. In *Physically-based modelling and simulation of climate and climatic change* (pp. 223–283). Springer. https://doi.org/10.1007/978-94-009-3041-4_5
- Fouquart, Y., & Bonnel, B. (1980). Computations of solar heating of the earth's atmosphere: A new parameterization. *Beiträge zur Physik der Atmosphäre*, 53.
- Fouquart, Y., Bonnel, B., & Ramaswamy, V. (1991). Intercomparing shortwave radiation codes for climate studies. *Journal of Geophysical Research*, 96(D5), 8955–8968. <https://doi.org/10.1029/90jd00290>
- Freidenreich, S. M., & Ramaswamy, V. (2005). Refinement of the Geophysical Fluid Dynamics Laboratory solar benchmark computations and an improved parameterization for climate models. *Journal of Geophysical Research*, 110(D17), D17105. <https://doi.org/10.1029/2004JD005471>
- Geleyn, J. F., JF, G., & Others. (1979). An economical analytical method for the computation of the interaction between scattering and line absorption of radiation. *Beiträge zur Physik der Atmosphäre*, 52(1), 1–16.
- Geleyn, J. F., Mašek, J., Brožková, R., Kuma, P., Degrauwe, D., Hello, G., & Pristov, N. (2017). Single interval longwave radiation scheme based on the net exchanged rate decomposition with bracketing. *Quarterly Journal of the Royal Meteorological Society*, 143(704), 1313–1335. <https://doi.org/10.1002/qj.3006>
- Geoffroy, O., Brenguier, J. L., & Burnet, F. (2010). Parametric representation of the cloud droplet spectra for les warm bulk microphysical schemes. *Atmospheric Chemistry and Physics*, 10(10), 4835–4848. <https://doi.org/10.5194/acp-10-4835-2010>
- Grenfell, T. C., & Warren, S. G. (1999). Representation of a nonspherical ice particle by a collection of independent spheres for scattering and absorption of radiation. *Journal of Geophysical Research*, 104(D24), 31697–31709. <https://doi.org/10.1029/1999JD900496>
- Hale, G. M., & Querry, M. R. (1973). Optical constants of water in the 200-nm to 200- μ m wavelength region. *Applied Optics*, 12(3), 555–563. <https://doi.org/10.1364/AO.12.000555>
- Hansen, J. E. (1971). Multiple scattering of polarized light in planetary atmospheres part II. Sunlight reflected by terrestrial water clouds. *Journal of the Atmospheric Sciences*, 28(8), 1400–1426. [https://doi.org/10.1175/1520-0469\(1971\)028<1400:MSOPLI>2.0.CO;2](https://doi.org/10.1175/1520-0469(1971)028<1400:MSOPLI>2.0.CO;2)
- Hogan, R. J., & Bozzo, A. (2018). A flexible and efficient radiation scheme for the ECMWF model. *Journal of Advances in Modeling Earth Systems*, 10(8), 1990–2008. <https://doi.org/10.1029/2018MS001364>
- Hogan, R. J., & Illingworth, A. J. (2000). Deriving cloud overlap statistics from radar. *Quarterly Journal of the Royal Meteorological Society*, 126(569). <https://doi.org/10.1002/qj.49712656914>
- Hogan, R. J., Schäfer, S. A. K., Klinger, C., Chiu, J. C., & Mayer, B. (2016). Representing 3-D cloud radiation effects in two-stream schemes: 2. Matrix formulation and broadband evaluation. *Journal of Geophysical Research: Atmospheres*, 121(14), 8583–8599. <https://doi.org/10.1002/2016jd024875>
- Hourdin, F., Foujols, M. A., Codron, F., Guemas, V., Dufresne, J. L., Bony, S., & Bopp, L. (2013). Impact of the LMDZ atmospheric grid configuration on the climate and sensitivity of the IPSL-CM5A coupled model. *Climate Dynamics*, 40(9–10), 2167–2192. <https://doi.org/10.1007/s00382-012-1411-3>
- Hu, Y., & Stamnes, K. (1993). An accurate parameterization of the radiative properties of water clouds suitable for use in climate models. *Journal of Climate*, 6(4), 728–742. [https://doi.org/10.1175/1520-0442\(1993\)006<0728:aapotr>2.0.co;2](https://doi.org/10.1175/1520-0442(1993)006<0728:aapotr>2.0.co;2)
- Hu, Y., & Stamnes, K. (2000). Climate sensitivity to cloud optical properties. *Tellus Series B Chemical and Physical Meteorology*, 52(1), 81–93. <https://doi.org/10.3402/tellusb.v52i1.16084>
- Igel, A. L., & van den Heever, S. C. (2017). The importance of the shape of cloud droplet size distributions in shallow cumulus clouds. Part II: Bulk microphysics simulations. *Journal of the Atmospheric Sciences*, 74(1), 259–273. <https://doi.org/10.1175/jas-d-15-0383.1>
- Joseph, J. H., Wiscombe, W. J., & Weinman, J. A. (1976). The delta-Eddington approximation for radiative flux transfer. *Journal of the Atmospheric Sciences*, 33(12), 2452–2459. [https://doi.org/10.1175/1520-0469\(1976\)033<2452:TDEAFR>2.0.CO;2](https://doi.org/10.1175/1520-0469(1976)033<2452:TDEAFR>2.0.CO;2)
- Jouhaud, J., Dufresne, J. L., Madeleine, J. B., Hourdin, F., Couvreux, F., Villefranche, N., & Jam, A. (2018). Accounting for vertical sub-grid-scale heterogeneity in low-level cloud fraction parameterizations. *Journal of Advances in Modeling Earth Systems*, 10(11), 2686–2705. <https://doi.org/10.1029/2018MS001379>
- Kurucz, R. L. (1994). Synthetic infrared spectra. *Symposium - International Astronomical Union*, 154, 523–531. <https://doi.org/10.1017/S0074180900124805>
- Lac, C., Chaboureaud, J.-P., Masson, V., Pinty, J.-P., Tulet, P., Escobar, J., et al. (2018). Overview of the Meso-NH model version 5.4 and its applications. *Geoscientific Model Development*, 11(5), 1929–1969. <https://doi.org/10.5194/gmd-11-1929-2018>
- Liu, Y., Daum, P. H., Guo, H., & Peng, Y. (2008). Dispersion bias, dispersion effect, and the aerosol–cloud conundrum. *Environmental Research Letters*, 3(4), 45021. <https://doi.org/10.1088/1748-9326/3/4/045021>

- Loeb, N. G., Doelling, D. R., Wang, H., Su, W., Nguyen, C., Corbett, J. G., et al. (2018). Clouds and the Earth's radiant energy system (CERES) energy balanced and filled (EBAF) top-of-atmosphere (TOA) edition-4.0 data product. *Journal of Climate*, 31(2), 895–918. <https://doi.org/10.1175/JCLI-D-17-0208.1>
- Lu, P., Zhang, H., & Li, J. (2011). Correlated k-distribution treatment of cloud optical properties and related radiative impact. *Journal of the Atmospheric Sciences*, 68(11), 2671–2688. <https://doi.org/10.1175/jas-d-10-05001.1>
- Madeleine, J. B., Hourdin, F., Grandpeix, J. Y., Rio, C., Dufresne, J. L., Vignon, E., et al. (2020). Improved representation of clouds in the atmospheric component LMDZ6A of the IPSL-CM6A Earth system model. *Journal of Advances in Modeling Earth Systems*, 12(10), e2020MS002046. <https://doi.org/10.1029/2020MS002046>
- Manners, J. (2015). Socrates technical guide suite of community radiative transfer codes based on edwards and slingo. In *Tech. rep.* Met Office.
- Martin, G. M., Johnson, D. W., & Spice, A. (1994). The measurement and parameterization of effective radius of droplets in warm stratocumulus clouds. *Journal of the Atmospheric Sciences*, 51(13), 1823–1842. [https://doi.org/10.1175/1520-0469\(1994\)051<1823:tmapoe>2.0.co;2](https://doi.org/10.1175/1520-0469(1994)051<1823:tmapoe>2.0.co;2)
- Mätzler, C. (2002). *MATLAB functions for Mie scattering and absorption, version 2*. IAP Res. Rep (Vol. 8, p. 9).
- Meador, W. E., & Weaver, W. R. (1980). Two-stream approximations to radiative transfer in planetary atmospheres: A unified description of existing methods and a new improvement. *Journal of the Atmospheric Sciences*, 37(3), 630–643. [https://doi.org/10.1175/1520-0469\(1980\)037<0630:TSATRT>2.0.CO;2](https://doi.org/10.1175/1520-0469(1980)037<0630:TSATRT>2.0.CO;2)
- Miles, N. L., Verlinde, J., & Clothiaux, E. E. (2000). Cloud droplet size distributions in low-level stratiform clouds. *Journal of the Atmospheric Sciences*, 57(2), 295–311. [https://doi.org/10.1175/1520-0469\(2000\)057<0295:CDSDL>2.0.CO;2](https://doi.org/10.1175/1520-0469(2000)057<0295:CDSDL>2.0.CO;2)
- Mishchenko, M. I., Dlugach, J. M., Yanovitskij, E. G., & Zakharova, N. T. (1999). Bidirectional reflectance of flat, optically thick particulate layers: An efficient radiative transfer solution and applications to snow and soil surfaces. *Journal of Quantitative Spectroscopy and Radiative Transfer*, 63(2–6), 409–432. [https://doi.org/10.1016/S0022-4073\(99\)00028-X](https://doi.org/10.1016/S0022-4073(99)00028-X)
- Misumi, R., Uji, Y., Tobo, Y., Miura, K., Uetake, J., Iwamoto, Y., et al. (2018). Characteristics of droplet size distributions in low-level stratiform clouds observed from Tokyo Skytree. *Journal of the Meteorological Society of Japan. Ser. II*, 96(4), 405–413. <https://doi.org/10.2151/jmsj.2018-040>
- Mitchell, D. L. (2002). Effective diameter in radiation transfer: General definition, applications, and limitations. *Journal of the Atmospheric Sciences*, 59(15), 2330–2346. [https://doi.org/10.1175/1520-0469\(2002\)059<2330:EDIRTG>2.0.CO;2](https://doi.org/10.1175/1520-0469(2002)059<2330:EDIRTG>2.0.CO;2)
- Mlawer, E. J., Taubman, S. J., Brown, P. D., Iacono, M. J., & Clough, S. A. (1997). Radiative transfer for inhomogeneous atmospheres: RRTM, a validated correlated-k model for the longwave. *Journal of Geophysical Research*, 102(D14), 16663–16682. <https://doi.org/10.1029/97JD00237>
- Morcrette, J. J., Barker, H. W., Cole, J. N., Iacono, M. J., & Pincus, R. (2008). Impact of a new radiation package, McRad, in the ECMWF integrated forecasting system. *Monthly Weather Review*, 136(12), 4773–4798. <https://doi.org/10.1175/2008MWR2363.1>
- Nam, C., Bony, S., Dufresne, J.-L., & Chepfer, H. (2012). The ‘too few, too bright’ tropical low-cloud problem in CMIP5 models. *Geophysical Research Letters*, 39(21), L21801. <https://doi.org/10.1029/2012GL053421>
- Nielsen, K. P., Gleeson, E., & Rontu, L. (2014). Radiation sensitivity tests of the HARMONIE 37h1 NWP model. *Geoscientific Model Development*, 7(4), 1433–1449. <https://doi.org/10.5194/gmd-7-1433-2014>
- Pincus, R., Barker, H. W., & Morcrette, J.-J. (2003). A fast, flexible, approximate technique for computing radiative transfer in inhomogeneous cloud fields. *Journal of Geophysical Research*, 108(D13), 4376. <https://doi.org/10.1029/2002JD003322>
- Pincus, R., Hannay, C., Klein, S. A., Xu, K.-M., & Hemler, R. (2005). Overlap assumptions for assumed probability distribution function cloud schemes in large-scale models. *Journal of Geophysical Research*, 110(D15), D15S09. <https://doi.org/10.1029/2004jd005100>
- Pontikis, C., & Hicks, E. (1992). Contribution to the cloud droplet effective radius parameterization. *Geophysical Research Letters*, 19(22), 2227–2230. <https://doi.org/10.1029/92gl02283>
- Pope, V., Gallani, M., Rowntree, P., & Stratton, R. A. (2000). The impact of new physical parametrizations in the Hadley centre climate model: HadAM3. *Climate Dynamics*, 16, 123–146. <https://doi.org/10.1007/s003820050009>
- Price, J. D., Lane, S., Boutle, I. A., Smith, D. K., Bergot, T., Lac, C., et al. (2018). LANFEX: A field and modeling study to improve our understanding and forecasting of radiation fog. *Bulletin of the American Meteorological Society*, 99(10), 2061–2077. <https://doi.org/10.1175/BAMS-D-16-0299.1>
- Räisänen, P. (1999). Parameterization of water and ice cloud near-infrared single-scattering co-albedo in broadband radiation schemes. *Journal of the Atmospheric Sciences*, 56(4), 626–641. [https://doi.org/10.1175/1520-0469\(1999\)056<0626:powaic>2.0.co;2](https://doi.org/10.1175/1520-0469(1999)056<0626:powaic>2.0.co;2)
- Räisänen, P., Barker, H. W., Khairoutdinov, M. F., Li, J., & Randall, D. A. (2004). Stochastic generation of subgrid-scale cloudy columns for large-scale models. *Quarterly Journal of the Royal Meteorological Society*, 130(601), 2047–2067. <https://doi.org/10.1256/qj.03.99>
- Ritter, B., & Geleyn, J.-F. (1992). A comprehensive radiation scheme for numerical weather prediction models with potential applications in climate simulations. *Monthly Weather Review*, 120(2), 303–325. [https://doi.org/10.1175/1520-0493\(1992\)120<0303:acrsfn>2.0.co;2](https://doi.org/10.1175/1520-0493(1992)120<0303:acrsfn>2.0.co;2)
- Roehrig, R., Beau, I., Saint-Martin, D., Alias, A., Decharme, B., Guérémy, J. F., et al. (2020). The CNRM global atmosphere model ARPEGE-Climate 6.3: Description and evaluation. *Journal of Advances in Modeling Earth Systems*, 12(7), e2020MS002075. <https://doi.org/10.1029/2020MS002075>
- Rotstayn, L. D., & Liu, Y. (2003). Sensitivity of the first indirect aerosol effect to an increase of cloud droplet spectral dispersion with droplet number concentration. *Journal of Climate*, 16(21), 3476–3481. [https://doi.org/10.1175/1520-0442\(2003\)016<3476:SOTFIA>2.0.CO;2](https://doi.org/10.1175/1520-0442(2003)016<3476:SOTFIA>2.0.CO;2)
- Rotstayn, L. D., & Liu, Y. (2009). Cloud droplet spectral dispersion and the indirect aerosol effect: Comparison of two treatments in a GCM. *Geophysical Research Letters*, 36(10), L10801. <https://doi.org/10.1029/2009GL038216>
- Shonk, J. K. P., & Hogan, R. J. (2008). Tripleclouds: An efficient method for representing horizontal cloud inhomogeneity in 1D Radiation schemes by using three regions at each height. *Journal of Climate*, 21(11), 2352–2370. <https://doi.org/10.1175/2007JCLI1940.1>
- Sieron, S. B., Clothiaux, E. E., Zhang, F., Lu, Y., & Otkin, J. A. (2017). Comparison of using distribution-specific versus effective radius methods for hydrometeor single-scattering properties for all-sky microwave satellite radiance simulations with different microphysics parameterization schemes. *Journal of Geophysical Research*, 122(13), 7027–7046. <https://doi.org/10.1002/2017JD026494>
- Slingo, A., & Schrecker, H. M. (1982). On the shortwave radiative properties of stratiform water clouds. *Quarterly Journal of the Royal Meteorological Society*, 108(456), 407–426. <https://doi.org/10.1002/qj.49710845607>
- Stephens, G. L. (1978). Radiation profiles in extended water clouds. II: Parameterization schemes. *Journal of the Atmospheric Sciences*, 35, 2123–2132. [https://doi.org/10.1175/1520-0469\(1978\)035<2123:rpiewc>2.0.co;2](https://doi.org/10.1175/1520-0469(1978)035<2123:rpiewc>2.0.co;2)
- Stevens, B., Giorgetta, M., Esch, M., Mauritsen, T., Crueger, T., Rast, S., et al. (2013). Atmospheric component of the mpi-m earth system model: Echem6. *Journal of Advances in Modeling Earth Systems*, 5(2), 146–172. <https://doi.org/10.1002/jame.20015>
- Strauss, C. (2020). *Quelle turbulence sur les bords des nuages convectifs?* Unpublished doctoral dissertation. University of Toulouse.
- Sulak, A. M., Calabrese, W. J., Ryan, S. D., & Heus, T. (2020). The contributions of shear and turbulence to cloud overlap for cumulus clouds. *Journal of Geophysical Research: Atmospheres*, 125(10), e2019JD032017. <https://doi.org/10.1029/2019JD032017>

- Tas, E., Teller, A., Altaratz, O., Axisa, D., Bruintjes, R., Levin, Z., & Koren, I. (2015). The relative dispersion of cloud droplets: Its robustness with respect to key cloud properties. *Atmospheric Chemistry and Physics*, *15*(4), 2009–2017. <https://doi.org/10.5194/acp-15-2009-2015>
- Thompson, G., Tewari, M., Ikeda, K., Tessendorf, S., Weeks, C., Otkin, J., & Kong, F. (2016). Explicitly-coupled cloud physics and radiation parameterizations and subsequent evaluation in wrf high-resolution convective forecasts. *Atmospheric Research*, *168*, 92–104. <https://doi.org/10.1016/j.atmosres.2015.09.005>
- Twomey, S. (1974). Pollution and the planetary albedo. *Atmospheric Environment (1967)*, *8*(12), 1251–1256. [https://doi.org/10.1016/0004-6981\(74\)90004-3](https://doi.org/10.1016/0004-6981(74)90004-3)
- Van De Hulst, H. C. (1968). Radiative transfer in thick atmospheres with an arbitrary scattering function. *Bulletin of the Astronomical Institutes of the Netherlands*, *20*, 77–86.
- Vié, B., Pinty, J.-P., Berthet, S., & Leriche, M. (2016). LIMA (v1.0): A quasi two-moment microphysical scheme driven by a multimodal population of cloud condensation and ice freezing nuclei. *Geoscientific Model Development*, *9*(2), 567–586. <https://doi.org/10.5194/gmd-9-567-2016>
- Vignesh, P. P., Jiang, J. H., Kishore, P., Su, H., Smay, T., Brighton, N., & Velicogna, I. (2020). Assessment of cmip6 cloud fraction and comparison with satellite observations. *Earth and Space Science*, *7*(2), e2019EA000975. <https://doi.org/10.1029/2019ea000975>
- Voldoire, A., Saint-Martin, D., Sénési, S., Decharme, B., Alias, A., Chevallier, M., et al. (2019). Evaluation of CMIP6 DECK experiments with CNRM-CM6-1. *Journal of Advances in Modeling Earth Systems*, *11*(7), 2177–2213. <https://doi.org/10.1029/2019MS001683>
- Von Salzen, K., Scinocca, J. F., McFarlane, N. A., Li, J., Cole, J. N. S., Plummer, D., et al. (2013). The Canadian fourth generation atmospheric global climate model (CanAM4). Part I: Representation of physical processes. *Atmosphere - Ocean*, *51*(1), 104–125. <https://doi.org/10.1080/07055900.2012.755610>
- Wang, M., Peng, Y., Liu, Y., Liu, Y., Xie, X., & Guo, Z. (2020). Understanding cloud droplet spectral dispersion effect using empirical and semi-analytical parameterizations in NCAR CAM5.3. *Earth and Space Science*, *7*(8), e2020EA001276. <https://doi.org/10.1029/2020EA001276>
- Wang, Y., Zhao, C., McFarquhar, G. M., Wu, W., Reeves, M., & Li, J. (2021). Dispersion of droplet size distributions in supercooled non-precipitating stratocumulus from aircraft observations obtained during the southern ocean cloud radiation aerosol transport experimental study. *Journal of Geophysical Research: Atmospheres*, *126*(6), e2020JD033720. <https://doi.org/10.1029/2020JD033720>
- Wild, M. (2020). The global energy balance as represented in CMIP6 climate models. *Climate Dynamics*, *55*(3–4), 553–577. <https://doi.org/10.1007/s00382-020-05282-7>
- Wild, M., Hakuba, M. Z., Folini, D., Dörig-Ott, P., Schär, C., Kato, S., & Long, C. N. (2019). The cloud-free global energy balance and inferred cloud radiative effects: An assessment based on direct observations and climate models. *Climate Dynamics*, *52*(7–8). <https://doi.org/10.1007/s00382-018-4413-y>
- Wiscombe, W. J. (1977). The Delta-M method: Rapid yet accurate radiative flux calculations for strongly asymmetric phase functions. *Journal of the Atmospheric Sciences*, *34*(9), 1408–1422. [https://doi.org/10.1175/1520-0469\(1977\)034<1408:tdmrya>2.0.co;2](https://doi.org/10.1175/1520-0469(1977)034<1408:tdmrya>2.0.co;2)
- Xu, L.-S., Zhang, G.-T., & Cheng, H.-B. (1996). Parameterization of the shortwave radiative properties of water clouds for use in GCMs. *Theoretical and Applied Climatology*, *55*(1–4), 211–219. <https://doi.org/10.1007/BF00864717>
- Yang, P., Bi, L., Baum, B. A., Liou, K.-N., Kattawar, G. W., Mishchenko, M. I., & Cole, B. (2013). Spectrally consistent scattering, absorption, and polarization properties of atmospheric ice crystals at wavelengths from 0.2 to 100 μ m. *Journal of the Atmospheric Sciences*, *70*(1), 330–347. <https://doi.org/10.1175/jas-d-12-039.1>
- Zelinka, M. D., Myers, T. A., McCoy, D. T., Po-Chedley, S., Caldwell, P. M., Ceppi, P., & Taylor, K. E. (2020). Causes of Higher Climate Sensitivity in CMIP6 Models. *Geophysical Research Letters*, *47*(1), e2019GL085782. <https://doi.org/10.1029/2019GL085782>
- Zhao, C., Tie, X., Brasseur, G., Noone, K. J., Nakajima, T., Zhang, Q., et al. (2006). Aircraft measurements of cloud droplet spectral dispersion and implications for indirect aerosol radiative forcing. *Geophysical Research Letters*, *33*(16), L16809. <https://doi.org/10.1029/2006GL026653>
- Zhao, W., Peng, Y., Wang, B., Yi, B., Lin, Y., & Li, J. (2018). Comparison of three ice cloud optical schemes in climate simulations with community atmospheric model version 5. *Atmospheric Research*, *204*, 37–53. <https://doi.org/10.1016/j.atmosres.2018.01.004>

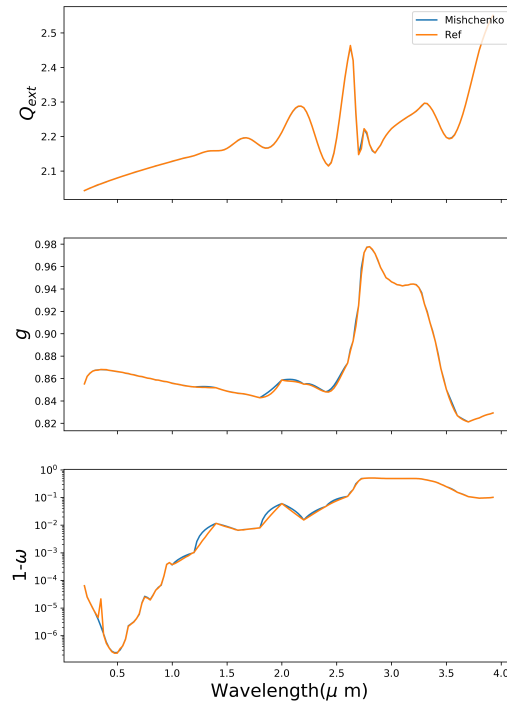


Figure 3.2: Average SSPs on a Log DSD calculated using Mishchenko (orange), and by the integrals used for this study (in blue) for the SW region using 10000 logarithmically spaced sub-intervals

3.3 Supplementary material of the article

This section further details some technical and numerical aspects of the parameterizations. The first subsection contains the validation of numerical integral calculations over DSD to derive average values of SSPs on analytical DSD functions. The second part is dedicated to adjusting numerical fits on the reference values of the SSPs to derive the coefficients of parameterizations.

3.3.1 Impact of the discretization of the droplet size distribution for SSP computation

As explained in Eqs 7-9 of the article, the SSPs must be integrated over the DSD functions. We have used a trapezoidal discretization method to solve these integrals. An example of a sensitivity test to the number of sub-intervals is explained briefly in this subsection. Here a log-normal function is used to describe the DSD. The SSPs are calculated for the radii range between 0.01-500 μm (upper and lower limits of integrals) for three different numbers of logarithmically-spaced sub-intervals with 1000, 10000, and 100000 intervals, respectively. The results were compared to the average SSPs over the same log-normal function using the Mie calculation method from Mishchenko et al. (1999) in ARTDECO. The comparison results for 10000 configuration are depicted in Figs. 3.2.

The 10000 points configuration is considered optimal because no improvement is observed when increasing to 100000, and deterioration is seen (more oscillations added) when it is decreased to 1000 points. This integration configuration has been chosen for all integrals over DSD.

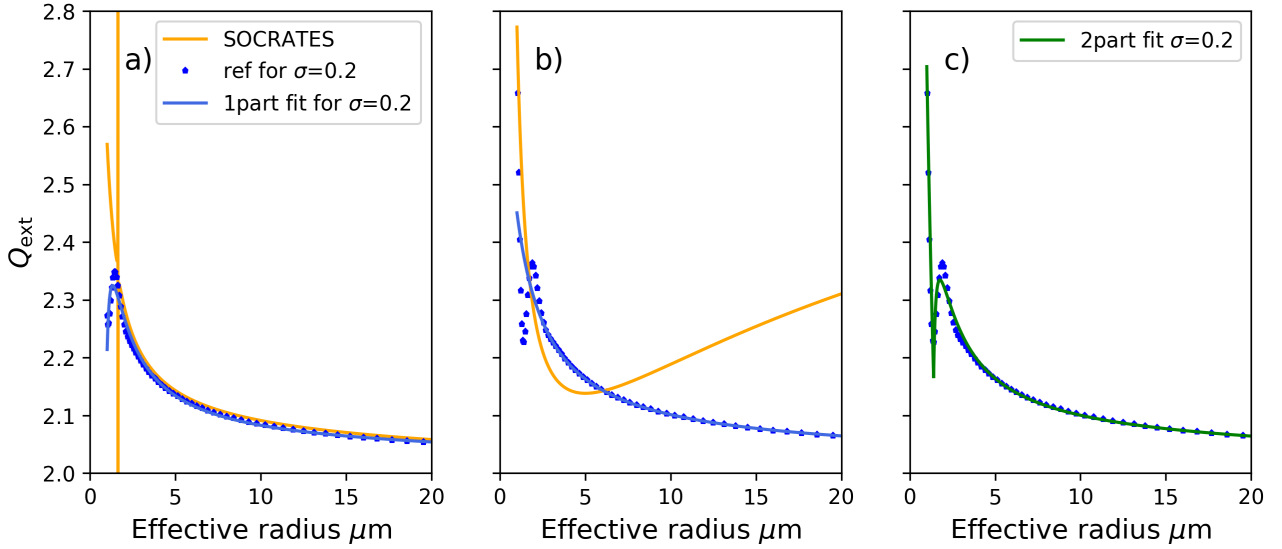


Figure 3.3: Blue points show Q_{ext} averaged over a Log DSD with $\sigma=0.2$. Blue curves show the improved version of SOCRATES fit called 1-part fit. The green curve shows the two part fit results. Orange curves indicate the SOCRATES parameterization. All these elements are illustrated for the 9th band of ecRad in *a* and for 8th band in *b* and *c*

3.3.2 Curve Fitting validation

As stated in the article, nine spectral methods exist for each of the four shapes of log-normal and Gamma-modified DSD functions. The same analytical functions of Padé (Eqs. 20-22 in the article), as employed in the SOCRATES parameterization of ecRad, are used to perform the fits on reference values of the SSPs against the effective radius for each of the nine spectral methods and eight DSD shapes. However, as we will discuss next, applying these functions may result in several issues. The reference SSPs for the ninth band of the ecRad, calculated for a cloud having a log-normal DSD shape with $\sigma=0.2$, is illustrated in blue spots in Fig 3.3-a. The orange curve is depicted using directly the SOCRATES parameterization coefficients in this band. A singularity is observed at about $1.6 \mu\text{m}$. For the eighth band, shown in Fig 3.3-b, the oscillation of reference SSPs is missed by SOCRATES parameterization and diverges from the reference points in larger effective radii. To handle this issue, we have first tried to attain an improved least-square fitting by choosing more intervals in the vicinity of oscillation points. As observable in the blue curves in Fig. 3.3, our method resolves the singularity problem in the ninth band but still can not capture the oscillations in the eighth band (between 1 and 3 microns).

This problem was predominant over most spectral bands and for all DSD shapes. To deal with this, we split the SSP- r_{ref} scatter-plots into two fractions on the point where the oscillations take place. We used the numerical functions of SOCRATES (Eqs 20-22 in the article) for each part and constrained the least-square method to ensure continuity between the two parts at the cut-point. Thereupon, 32 coefficients, instead of 16, are obtained for each band and DSD shape. To avoid the time-consuming method of deriving a cut-point visually and fitting coefficients separately for each SSP on each spectral band and a given DSD shape, we tried to generalize the 2-part fit method to a more automated one. The cut-points r_{ref} values derived visually for each spectral band for Q_{ext} present a linear dependency on the central wavelength of the bands shown in blue spots in Fig. 3.4. Dividing these cut point r_{ref} values by the central wavelengths gives red points, which approximate the constant value of 2. We

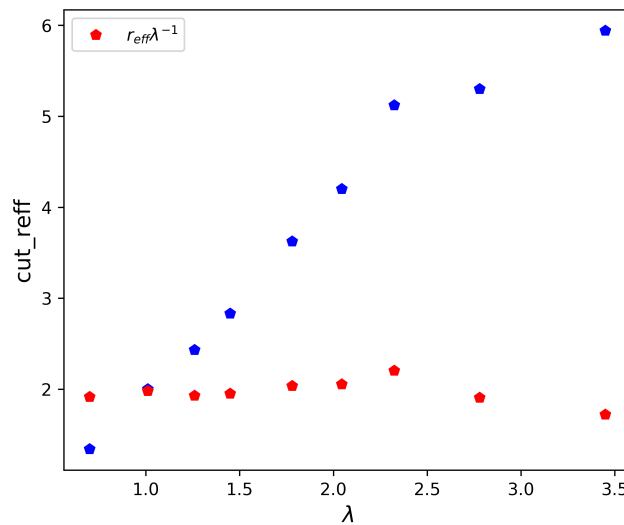


Figure 3.4: Optimum cut points against central wavelength of bands and threshold of 2

utilised this $r_{\text{effcut}}/\lambda_{\text{central}}=2$ threshold to derive cut-points for each band and all DSD shapes. However, this method does not work for the single scattering albedo (SSA). The r_{eff} values where the local minimum of SSA takes place were determined as the cut-points for SSA. A two-part fit example is illustrated with the green curve in Fig 3.3-c.

3.4 Discussion

In this section we will argue the validation of our two-stream method presented in section 3.2 of the article against a more detailed radiative code using ARTDECO. Then, a complementary study to the spectral averaging methods presented in section 3.2 of the article is presented. Further, the effect of number concentration, N , on the observed uncertainty behaviour in the article is assessed. Sensitivity of errors in bulk radiative properties to the number of spectral bands are studied in the last part of this section.

3.4.1 Evaluation of two-stream and Spectral averaging methods

Several spectral averaging methods were introduced in this study, as described in section 3.2 of the article. The two-stream approach used to develop these averaging methods is constrained to no-atmosphere condition and some other assumptions described in section 2.1.1. Having this in mind, the first goal of this section is to evaluate the two-stream estimates of the bulk radiative properties in high spectral resolution against that of a detailed RTE model in no atmosphere mode with the same spectral resolution. This allows identifying if there exists any systematic inherent error in the two-stream method. Once the two-stream's accuracy is ensured, the second objective is to assess the performance of SSA averaging methods in deriving broad band bulk radiative properties. A similar practice is carried out in section 3.2 of the paper (results are illustrated in Fig 5). The key difference with the latter is the reference high spectral resolution bulk radiative properties. In the article, these reference values were calculated based on the two-stream in no atmosphere condition. While here, the reference computations are performed with ARTDECO (described in the section 2.1.3) in the presence of an atmosphere containing the absorption of gases and Rayleigh scattering by air molecules.

To achieve the first objective, the SSPs are first averaged over a log-normal DSD with $\sigma=0.35$ and $r_{\text{eff}}=10 \mu\text{m}$ (as in Eqs 7 to 9 of the article) for 267 wavelengths in the SW. Subsequently, these SSPs should be fed into the ARTDECO and the two-stream models to calculate the reference fluxes. There are two ways to enter these SSPs in ARTDECO, as explained in section 2.1.3. In the first approach, average SSPs are replicated by ARTDECO based on Mie theory and relying on the provided information on the DSD and the refractive index of cloud droplets. This method was not applied since we could not achieve a good match between the configuration of integrals on the DSD in ARTDECO and our two-stream method. In the second approach, the Legendre expansion coefficients (described in section 2.1.3) must be defined manually to describe the phase function. This is feasible, as explained in section 2.1.3, having the asymmetry parameter, g , and using the Henyey-Greenstein volume scattering function. Ergo, the SSPs are calculated and introduced manually in the library of the ARTDECO in an acceptable format for the model. The only point to note here is that the SSPs are calculated on 207 wavelengths instead of 267 in the two-stream. The reason is the number of the g -points of the k -distribution model used in ARTDECO. Given this, we have chosen the closest wavelength configuration to our 267 wavelengths in the two-stream, which was 207 in ARTDECO. Accordingly, the two-stream flux calculations were adjusted to these 207 wavelengths. To deal with the RT equations in ARTDECO, the 4-stream DISORT 1D solver is activated, the solar zenith angle is set to 50 degrees (to match that of the two-stream), and the surface albedo is assumed to be zero. Atmospheric absorption and Rayleigh scattering are excluded in this test.

The transmittances from this run of ARTDECO and the two-stream are illustrated in Fig. 3.5-a, for three different optical thicknesses of 1, 10, and 15. The biases and the broad-band errors of the two-stream comparing the reference are shown in Fig. 3.5-b. Overall, the two-stream captures the variability of the reference transmittance from ARTDECO except for the absorbing wavelengths, 2.5-3.7 μm of the SW, where the transmittance is near zero. The bias is reduced for the lower optical thicknesses. The maximum broad-band error is around 1 %, which determines the maximum inherent error of the two-stream. This discrepancy can be explained by the difference between the number of directions used to deal with the RT equations in our two-stream and the 4-stream of DISORT-ARTDECO.

In order to reach our second objective, the averaged SSPs on the spectral bands using eight different spectral averaging methods, were applied as input to ARTDECO. The spectral resolution is the same as in the previous experiment. Though this time, the spectrally averaged SSPs over each band are used as the constant values through that band. Other configurations of the ARTDECO are similar to that described for the first test. Eight simulations corresponding to each of the SSA averaging methods were performed in the presence of the atmosphere (by activating the gas absorption) for four cloud optical thicknesses of 1, 5, 10, and 20.

The errors of Transmittance/Reflectance calculated with different spectral averaging methods, relative to the reference ARTDECO values of test 1, on broad-band, are illustrated in Fig. 3.6. The global error due to the spectral averaging and the presence of the atmosphere is lower than the systematic error of the two-stream method. These results are commensurate with the observed errors in Fig. 5 of the article (detailed in section 3.2 of the article). Also, the errors obtained with different spectral averaging methods are within 1%. These arguments propose that even the presence of atmosphere does not influence the two-stream results obtained in no-atmosphere conditions.

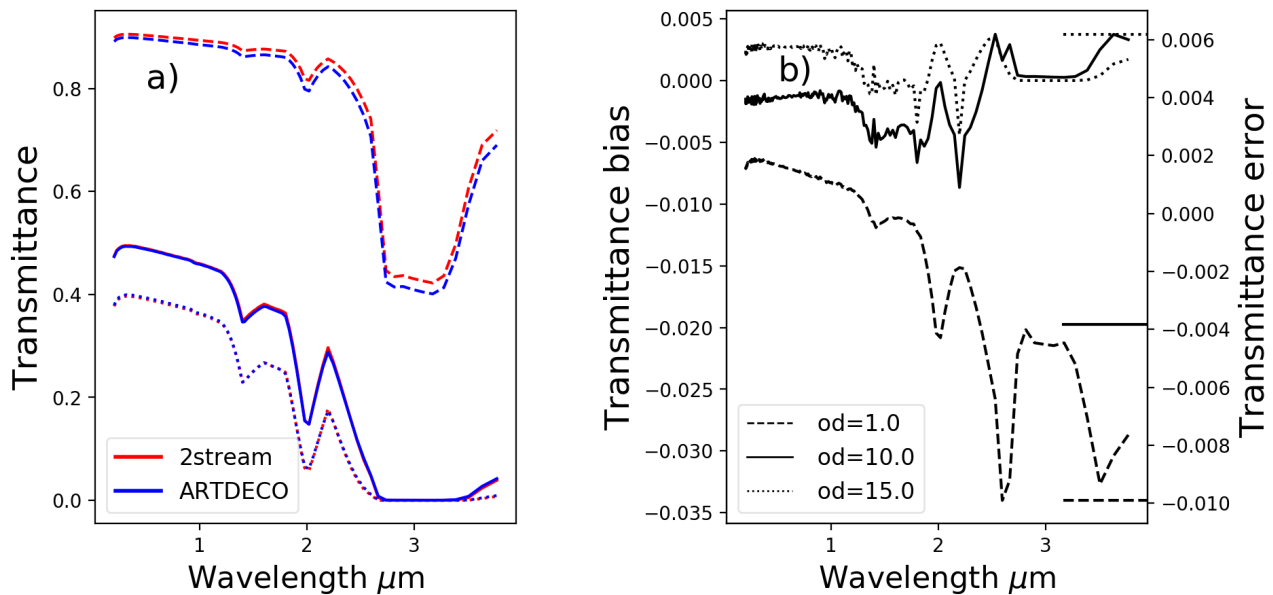


Figure 3.5: a) The transmittances calculated using two-stream (in red) and ARTDECO (blue) for 207 wavelengths in the SW range b) The spectral bias (curves and right side axis) and broad-band errors (horizontal bars and right side axis) of two-stream Transmittance relative to ARTDECO.

3.4.2 Sensitivity to the Number concentration

In all uncertainty assessing experiments of the article, the droplet number concentration was set to 200 cm^{-3} . As discussed in the conclusion of the paper, several studies have focused on N and its indirect impact on radiation through its interaction with microphysical processes (Igel and van den Heever, 2017; Wang et al., 2021). Here the focus is only on the direct radiative impact of N , excluding its interaction with other microphysical parameters such as evaporation and autoconversion. For this purpose, we extended the ideal case experiment of the paper to 100 cases with N values ranging between 10 to 450 cm^{-3} . The LWC spreads between $0.01\text{-}1 \text{ g}^{-3}$, and as the ideal case cloud of the article is used (the height of which is about 1400 m), this LWC range corresponds to LWP ranging from 0.014 to 1.4 kg m^{-2} . The outcome is depicted in Fig. 3.7 (middle column). For the same LWC- N pairs, the transmitted flux for just one shape ($\sigma = 0.9$) and the transmitted flux difference between two extreme shapes normalized by the transmitted flux of $\sigma = 0.9$ are also illustrated in the first and third columns of Fig. 3.7 respectively.

A global mean uncertainty of about 100 W m^{-2} is observed in the middle panel. This is in line with the results of the article for the ideal cloud.

For the N values between 400 and 80 cm^{-3} , the uncertainty of transmittance is maximum for the lower values and grows for higher values of LWC. Since the N value of the ideal cloud used in the article is within this mentioned range, the same behavior for the uncertainty is discernible in Fig 9 of the article. However outside of $400\text{-}80 \text{ cm}^{-3}$ range the trend of uncertainty is different. Thereafter, the uncertainty is lower for the smaller LWC values, reaches its maximum at around $0.1\text{-}0.2 \text{ g m}^{-3}$, and then diminishes for greater LWCs. To understand this behavior, we must focus on the transmittance variations for just one shape of the DSD. For instance, for Log DSD with $\sigma = 0.9$ depicted in Fig 3.7, it can be noted that the transmittance variations are aligned with the optical thickness isolines (full contour lines). Nevertheless, two points having the same transmittance may be placed on two highly different isolines of effective radius (dotted lines in

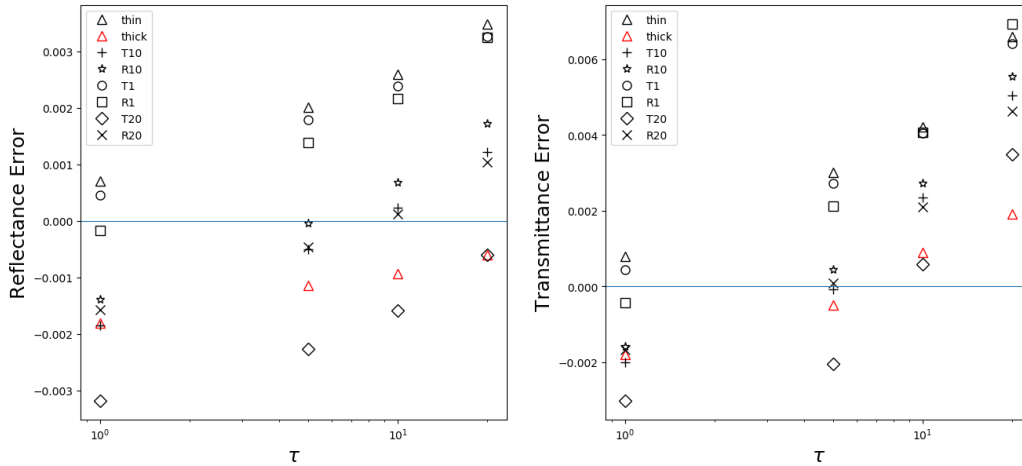


Figure 3.6: Errors of Transmittance/Reflectance obtained with different spectral averaging methods (illustrated with different geometrical shapes), relative to the reference ARTDECO values, for four clouds with optical thicknesses of 1, 5, 10 and 20, in the presence of an atmosphere.

Fig 3.7). This highlights the fact that the effective radius is not the only constraining factor of bulk radiative properties, even if the DSD shape is fixed. The isolines of optical thickness difference, $\Delta\tau$, between two extreme shapes (displayed in the middle and right-side of Fig. 3.7), indicate that both the absolute and relative differences of transmitted flux also correlate well with optical thickness variations.

Another noteworthy point is that the A and B spots highlighted in Fig. 3.7 present relatively similar transmittance differences, while they are not on the same optical thickness isoline and do not have similar effective radii either. To understand this, we look into the PDF shapes of these points provided in Fig. 3.8. In point A, switching the DSD from $\sigma=0.9$ to $\sigma=0.2$ shifts the peak position of PDF by a factor of 3, while the peak position changes by a factor of 9, in point B. This is why we get more relative difference error in B than in A as observable in the right-side column of Fig. 3.7. Although the transmitted flux in A is 70% higher than in B, the absolute difference or uncertainty obtained in both points is very close.

3.4.3 Sensitivity to spectral band resolution

The article studied how the spectral averaging methods of SSPs over the spectral bands can impact the bulk radiative properties. Nevertheless, no argument was made on the number of the bands that should be chosen since the radiative model presets it. Changing the number and layouts of the bands requires fundamental changes in the code's arrangement. Indeed, the 14 spectral bands in ecRad, are a compromise achieved considering gaseous absorption, Rayleigh scattering, the optical properties of aerosols, and the albedo of the surface. Therefore a slight change in band layouts means manipulation of all these components. To this end, this section aims to explore the effect of changing the number of the bands only in SSPs parameterization on the bulk radiative properties of clouds.

The two-stream method is employed for flexibility in creating new bands and focusing only on the SSPs of cloud droplets and their direct effect on bulk radiative properties. We begin by partitioning 280 equally-spaced wavelengths into n bands in SW. Then the mean reference and parameterization-based Transmittances/Reflectances are compared over each of these bands to derive absolute and relative differences. Parameterization-based mean Transmittances/Re-

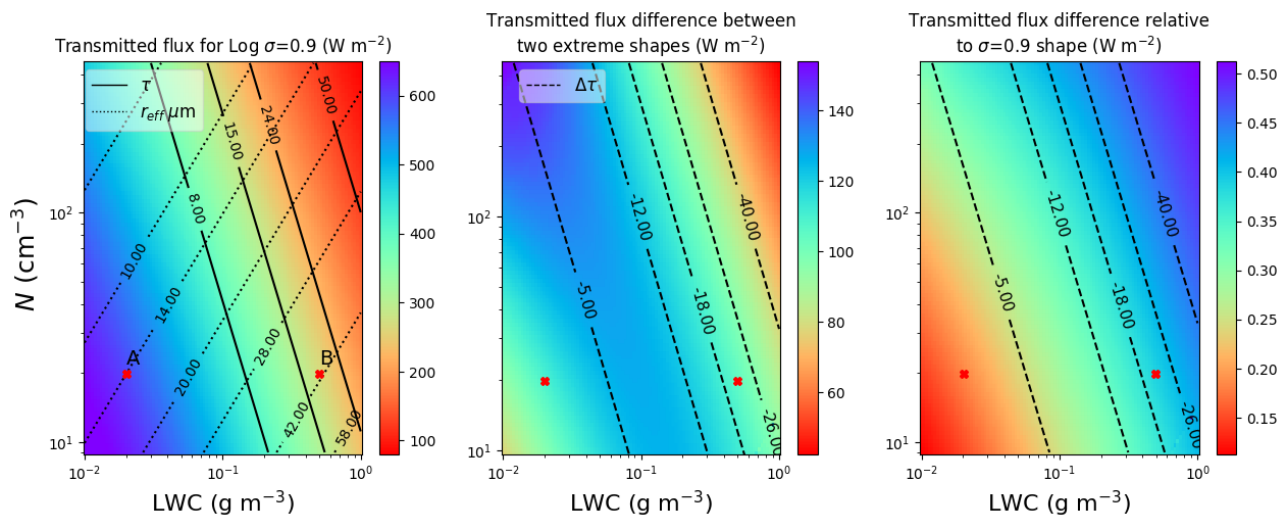


Figure 3.7: From left to right: Transmitted flux for a Log DSD with $\sigma = 0.9$, the transmitted flux difference between $\sigma=0.9$ and $\sigma=0.2$, transmittance relative difference with respect to $\sigma=0.9$. The dashed lines in the two right figures indicate the isolines of the optical depth difference between $\sigma=0.9$ and $\sigma=0.2$. The Full (dashed) lines on the first left column, shows the contour of the optical-depth (effective radius) for simulations of $\sigma=0.9$

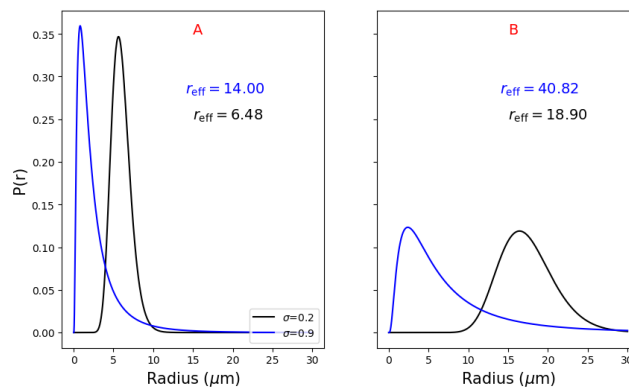


Figure 3.8: The PDF shapes of two points Highlighted in Fig 3.7

flectances are generated by adopting thin and thick spectral averaging methods. The reference mean transmittances are computed simply from the high-resolution reference transmittances calculated with the two-stream method (for more details on performing this kind of comparison with the two-stream method, please refer to section 3.2 of the article). For 19 values of n varying between 2 and 40 bands, Transmitted/reflected relative errors calculated for thin and thick averaging methods are tabulated in Fig. 3.9-a and b, respectively. All these computations have been carried out for a cloud of $\tau=10$, having a Log DSD shape of $\sigma=0.35$. The high-resolution cloud absorption ($1-\omega$) is also superposed in the figures (it is shown with cyan dashed lines, and the ordinate is on the right side of the graph).

It appears that the error is separable into two zones of wavelengths at about $2.1 \mu m$. After this point, the absorption increases, and a limited number of photons can escape the cloud. The transmittance drops, and the thin averaging method performance degrades. As more bands are generated, the overall performance is improved, but the error becomes concentrated in the bands where absorption rises or falls dramatically. Contrarily, error vanishes in the bands where

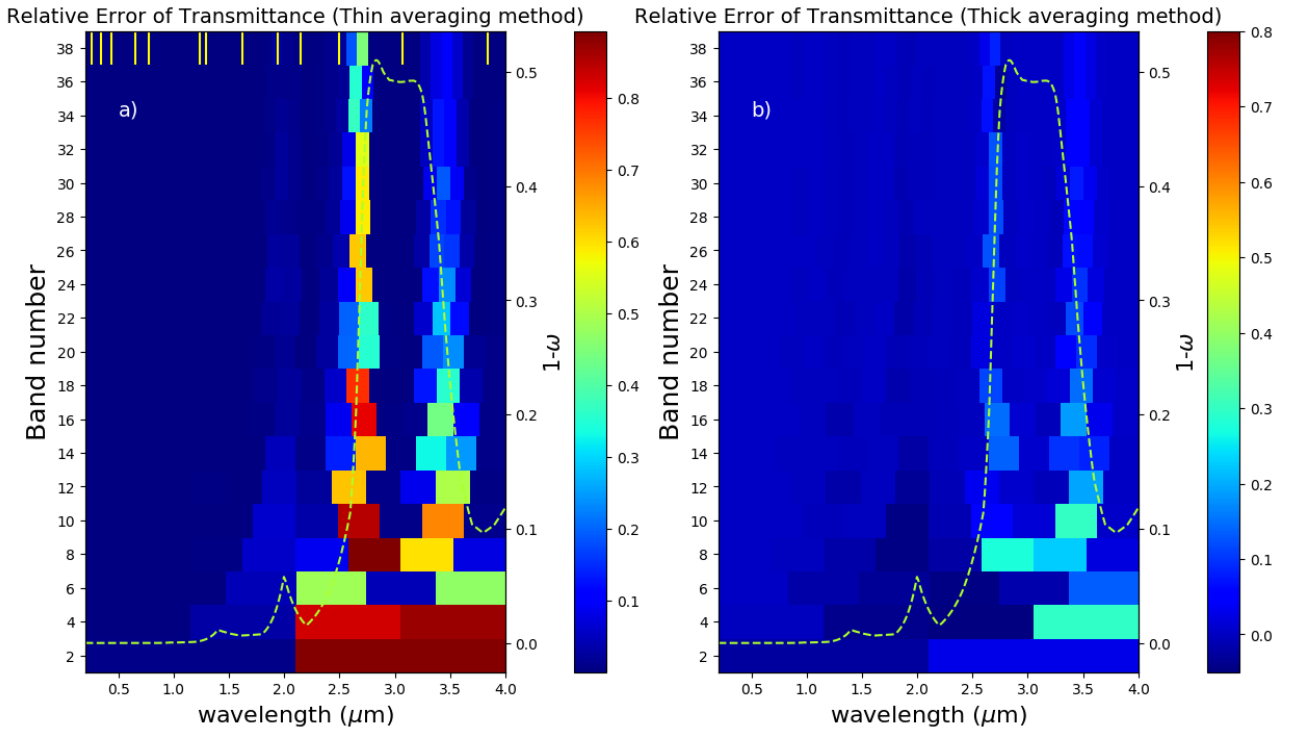


Figure 3.9: The error of transmittance calculated with a)Thin averaging and b)Thick averaging methods relative to the reference transmittance mean on each spectral band for 20 different band arrangements. Dashed-line presents the absorption calculated on 280 wavelengths. Yellow bars on upper side of *a* denote the ecRad bands

the absorption remains relatively constant. It can be noted that the use of the thick averaging method improves the results remarkably. This is also in line with the findings of Edwards and Slingo (1996) who recommends using the thick averaging method in the models with lower band numbers. However, it must be noted that the thick averaging method generates negative errors, especially in the first half of the SW region. To understand these error behaviors in Fig. 3.9 we provide a more in-depth vision by looking at the coincident trend of high-resolution transmittance and absorption over the SW region illustrated in Fig. 3.10-a and their relation depicted in Fig. 3.10-b.

As the optical thickness is fixed here, the spectral change rate of the transmittance on a given band depends on the spectral variation of the absorption and the sensitivity of transmittance to the absorption as follows:

$$\frac{dT}{d\lambda} = \frac{d(1-\omega)}{d\lambda} \frac{dT}{d(1-\omega)} \quad (3.1)$$

For $\lambda < 2.55 \mu\text{m}$ (shown with vertical blue dashed line in Fig. 3.10-b), regarding the exponential relation between T and absorption in Fig. 3.10-b, the transmittance is extremely sensitive to the absorption changes (meaning that the second right-side term of 3.1 is high). In this zone, any slight spectral fluctuation of absorption, the first term in Eq. 3.1, is amplified by the effect of the second term. This is how three main transmittance plunges occur at around 1.35, 2, and 2.6 μm as discernible in Fig. 3.10-a. These oscillations are the central zones of the thin averaging method error. This can be deduced from comparing the reference mean transmittance (blue lines) and thin averaging-related transmittance for two configurations of band arrangements, viz. 2 and 14 bands (shown with dashed and dotted lines, respectively) visible

in Fig. 3.10-c. After about $2.2 \mu\text{m}$, as can be seen in Fig. 3.10-a, the absorption marks a rapid surge towards its maximum. In this zone, because both terms of 3.1 indicate a rate greater than one, the thin averaging error is maximum until where $\frac{dT}{d(1-\omega)}$ drops to lower than one in the vicinity of $\lambda=2.55 \mu\text{m}$. Thereafter, transmittance becomes nearly zero and insensitive to the absorption variations.

It is observed in Fig. 3.9 that the thin averaging method constantly underestimates the transmittance for any number of band selections. To obtain a higher value of transmittance over a band, one of the right-side terms of Eq. 3.1 must be adjusted. The absorption rate can not be changed since it relies on the refractive index of the water droplet. On this account, to modify the absorption rate, one must alter the material from the water droplet to another hydro-meteor. This change is unreasonable because it will alter the extinction efficiency and the asymmetry parameter. The second term of 3.1 is more appropriate for our goal. The exponential relation of T and $1 - \omega$ is controlled mainly by the optical thickness. For instance, the T-absorption relation is illustrated for a cloud with an optical thickness of 30 in Fig. 3.10-b. In this thicker cloud, transmittance plummets and reaches its minimum at a lower absorption value compared to $\tau=10$. The lower absorption is what we need to achieve higher transmittance over a band. This gives the idea of using an optically infinite cloud to get a closer approximation to the reference mean transmittances, as explained in section 3.2 of the paper. The band-mean absorptions derived from the thick and thin averaging methods for the two band configuration are indicated along with thin averaging absorption, in Fig. 3.10-b with orange and black vertical lines, respectively. As expected, the shift from thin to thick averaging absorption generates higher transmittance closer to the reference value. However, since the T is susceptible to any minute variation in absorption, the thick averaging method in the first band of 2 band configuration leads to a slight overestimation of transmittance, as shown in the zoomed portion of Fig. 3.10-b. This explains the negative error values observed in Fig. 3.10-b when the thick averaging method is used.

The ecRad bands are indicated with yellow bars above the Fig. 3.10-a. Visually, ecRad bands incorporate the fluctuations of Transmittance and absorption in the near-infrared region. However, most of the ecRad bands are placed in the zone lower than $2 \mu\text{m}$ where no noticeable errors are observed. Later bands are mostly related to the absorption saturation bands of water vapor or other gases.

3.5 Conclusion

Simulating the cloud radiative effect is a challenging task for the atmospheric models. It is subject to significant spread between models. This spread originates to some extent from the high variability of cloud features in the sub-grid scales, e.g., cloud fraction, LWP distribution, and convection. Nevertheless, another side of the problem is related to how the model treats the cloud-radiation interactions. On the microscopic scale of a droplet in a cloud, the SSPs can describe the fate of the incoming light photons. Bulk radiative properties of clouds that modulate the cloud radiative effects are highly dependent on the SSPs. Further, SSPs are highly sensitive to the wavelength of incident light and the droplet size, the properties that could not be resolved in the grid-scale of a GCM. Instead, a parameterization is generally designed, which defines the SSPs, over settled spectral bands instead of wavelengths. SSPs are estimated for each spectral band in terms of the effective radius of DSD. A set of assumptions are made on the DSD to derive these parameterizations. We call any uncertainties generated in bulk radiative properties rising from these assumptions made in SSPs parameterization the SSP-related

uncertainties. On the other hand, the effective radius is generally estimated from LWC and N based on another set of assumptions on DSD, considered generally in the microphysics scheme before entering the radiative core. Uncertainties associated with these later assumptions are called r_{eff} -related uncertainties. To quantify mentioned uncertainties in the atmospheric simulations, at the first step, a new set of parameterizations were developed, allowing for the choice of the different DSD shapes based on observations. Establishing a parameterization requires calculating mean values of SSPs on the spectral bands and over the DSDs with diverse r_{eff} values. By fitting curves, these reference SSPs are then formulated in terms of r_{eff} . To retain the formalism of the SOCRATES parameterization, we have used the same analytical functions as SOCRATES to derive the least-square fitting. It has been demonstrated that deriving the fits using these functions was not straightforward. We have improved capturing the SSPs oscillations that happened in clouds with effective radii smaller than $5 \mu\text{m}$. Again for the small effective radii, we have addressed some singularity problems observed in specific spectral bands. The advantage of these modifications was to extend the validity range of parameterizations to cover the clouds bearing the droplets as small as $r_{\text{eff}}=1$. Such small values have been recorded in observations, especially in fog cases Dupont et al. (2018), despite being rarely generated during NWP simulations. It is advisable to apply and assess our parameterizations in such cases in further studies.

New parameterizations were implemented in the ecRad radiative code (section 2.1.2), and offline simulations were run on various ideal and real clouds. We have shown that the DSD shape choice in parameterizations leads to an important uncertainty comparable to the existing spread between models. This finding challenges the radiative forcing simulation by GCM models which fixes the DSD shape in their radiative scheme (e.g. IPSL (Madeleine et al., 2020), ECHAM6 Stevens et al. (2013), CNRM-CM6-1 Roehrig et al. (2020)). The presentation of DSD shape, however, might vary in GCMs. It is sometimes identified by the effective radius coefficient, k , which is the cubic root of the mean volumic radius of droplets to r_{eff} as introduced by Martin et al. (1994). Another representation of DSD shape is the relative dispersion coefficient, describing the ratio between DSD width to mean radius of DSD, as suggested in Rotstayn and Liu (2003). Numerous pieces of research found that the shape of DSD can also modulate N through dynamics and microphysical processes (Liu et al. (2008), Wang et al. (2020)) and that this change in N affects further the cloud radiative forcing in GCM simulations (Rotstayn and Liu (2009), Zhao et al. (2018)). This motivated us to extend our uncertainty study limited to a fixed N and variety of LWC in the article to more N values. Overall, uncertainty has a reducing trend versus LWC or LWP (since the geometrical thickness of the ideal cloud is constant through our experiments, any result of LWC is expandible to the LWP). Interestingly this is in accordance with the findings of (Tuononen et al., 2019) who demonstrated that in the overcast condition, the positive bias of global horizontal irradiance forecasts by IFS model is related to the clouds with lower LWP. They postulated that an under-prediction of LWP or misrepresenting the optical properties could be the reason for the bias. Our results corroborate the second theory. However, we showed that this behavior holds only for the N values larger than about 80 cm^{-3} . In general, it turns out that the combined effect of the LWC and N variation on the DSD-related uncertainties of bulk radiative properties is correlated with the optical thickness change.

The application of our parameterization on the outputs of CNRM-CM6.1 GCM model shows that the overall uncertainty can attain 35 W m^{-2} in tropical regions, being predominantly covered by low-level liquid clouds. Extracting the effect of DSD shape separately in the r_{eff} and SSPs estimation reveals that the overall uncertainty is ascribed primarily to r_{eff} -related

uncertainty, about ten % of which is offset by the SSP-related uncertainty. The global mean effect of SSP-related contribution at TOA is approximately 2 W m^{-2} . To better understand this magnitude, we may compare it to the effective radiative forcing of anthropogenic aerosols, which can rise to -0.54 W m^{-2} as estimated by Fiedler et al. (2019). It is worth mentioning that since the r_{eff} is diagnosed from microphysics, the r_{eff} -related uncertainty underlines indeed, the inconsistency of DSD shape assumptions between the microphysics and radiation. Numerous studies reported improvements in their surface irradiance simulations by addressing this inconsistency, especially in WRF model Bae et al. (2016); Thompson et al. (2016); Sieron et al. (2017). In the next chapter, we will detail how our new parameterizations provide a basis for creating such consistent couplings between microphysics and radiation in MesoNH model.

Another issue in the SSPs parameterizations is that the SSPs integration on the determined spectral bands is not trivial. It primarily influences the single scattering albedo (SSA), which controls the cloud absorption in the first order. It turns out that the linear averaging SSPs using weighting by the incoming light at the top of the cloud works well within the limit of optically thin clouds. The thicker the cloud becomes optically, the Transmittance/Reflectance relation with the absorption becomes highly exponential. After a specific wavelength (about $2.55 \mu\text{m}$), Transmittance/Reflectance becomes non-sensitive to the variation of the absorption. Analogous to this mechanism exists in gaseous absorption. After a concentration threshold, the absorption of gas marks no variation. This wavelength is where the gaseous absorption saturation happens (perceptible also in the Fig. 1.4). We have discussed that the absorption parameterization can be modulated by adjusting the optical thickness to generate a good match between the band averaged and the reference bulk radiative properties. This later reference quantity is the average of the bulk radiative properties derived from the two-stream or other detailed RT model in high spectral resolution. In the case of gaseous absorption, this can be generated by the line-by-line method) bulk radiative property. It is worth noting that this adjusting method can vary depending on the target bulk radiative property. For instance, Fouquart and Bonnel (1980) adjusts the optical thickness to get good absorption. Ritter and Geleyn (1992) focus on getting the appropriate transmission through the atmospheric layers. Edwards and Slingo (1996) parameterize the $1-\omega$ in a fashion that yields a good approximation of the reflectance for an optically infinite cloud. Since the last version parameterization of ecRad, SOCRATES (Manners, 2015), employs the precedent method, we lead our study based on this method. In this case, however, two questions can be outlined. First, if we target the reflectance, how much do we degrade in estimating the transmittance or absorptance of a cloud as a trade-off? Second, if the method is designed to deliver the reflectance of an optically thick cloud, how good is its performance for an optically thin or moderate cloud? To answer these questions, we have generalized the thick averaging strategy to create several methods based on Transmittance and Reflectance of the clouds with thin and relatively thick optical thicknesses. For this practice, we used a simplified two-stream method where no atmosphere exists. The evaluation of this method against a detailed RT code exhibits errors within one %. Assessment of the bulk radiative properties estimated with our introduced methods against the mentioned detailed RT code for clouds with different optical thicknesses demonstrates errors lower than 1%, even in the presence of the atmosphere. These new averaging methods were then implemented in ecRad and applied on the same ideal and real clouds used in DSD-uncertainty experiments. This test revealed that the uncertainty due to the spectral averaging method is extremely lower than DSD-related uncertainties, especially in estimating the transmitted and reflected fluxes. Although, when it comes to absorption of the cloud, the uncertainty was primarily ascribed to the spectral averaging method compared to the choice of DSD, especially in

clouds with higher LWP.

Another challenge in spectral averaging is the consideration of the overlapping between the water vapor absorption lines with that of droplets in the cloud. In the real atmosphere, a part of the envelope of incoming flux arriving at the top of the atmosphere (TOA) undergoes absorption by the water vapor above the cloud, especially in the near-infrared region, before reaching the top of the cloud. This is why we use the intact TOA incoming solar radiation for deriving our spectral averages. Moreover, the water vapor in the cloud can also impact the absorption by droplets, though our methods were based on the two-stream method in no-atmosphere and no-water vapor conditions. Several studies have suggested a variety of methods to deal with these issues. In the following, we mention the most promising among them. Espinoza Jr (1996); Lu et al. (2011); Masek et al. (2016) propose mimicking the correlated k -distribution method of the gaseous absorption (Lacis and Hansen, 1974) on both gases and droplets. This includes ordering the absorption of droplets from more to less absorbing on the same g-points (detailed in section 1.3.2) of gases and extracting the k -distribution function coefficients. These coefficients are then used as the weights to derive the spectral averages of cloud droplets instead of using the incoming solar radiation.

It is worth noting that all these spectral averaging methods aim to alleviate the number of the bands and thus the computation burden in the models but retain the robustness of a high spectral resolution computation. For instance, Espinoza Jr (1996); Masek et al. (2016) aimed at achieving high accuracy for a single band in SW. Edwards and Slingo (1996) suggested the thick-averaging method to modify the 24-band parameterization of Slingo (1989) to a four-band configuration. A study of the sensitivity of bulk radiative properties to the number of the bands was also fulfilled in this chapter using the two-stream method (in no-atmosphere conditions). It was observed that the estimated band-mean transmittance's precision correlates with the number of bands. However, as the number of the band increases, the errors become concentrated in the bands where saturation (Transmittance/Reflectance saturation) happens. We showed that the use of thick-averaging can significantly moderate these errors.

Finally, all the uncertainty experiments carried out in this chapter were focused on the offline ecRad simulations. To have a more real image of the uncertainties in atmospheric simulations, it will be interesting to allow for interaction with other components of the model, and analysing their possible feedbacks. This is the subject that will be explored in the next chapter by coupling our parameterization to the 2-moment scheme LIMA, in MesoNH model.

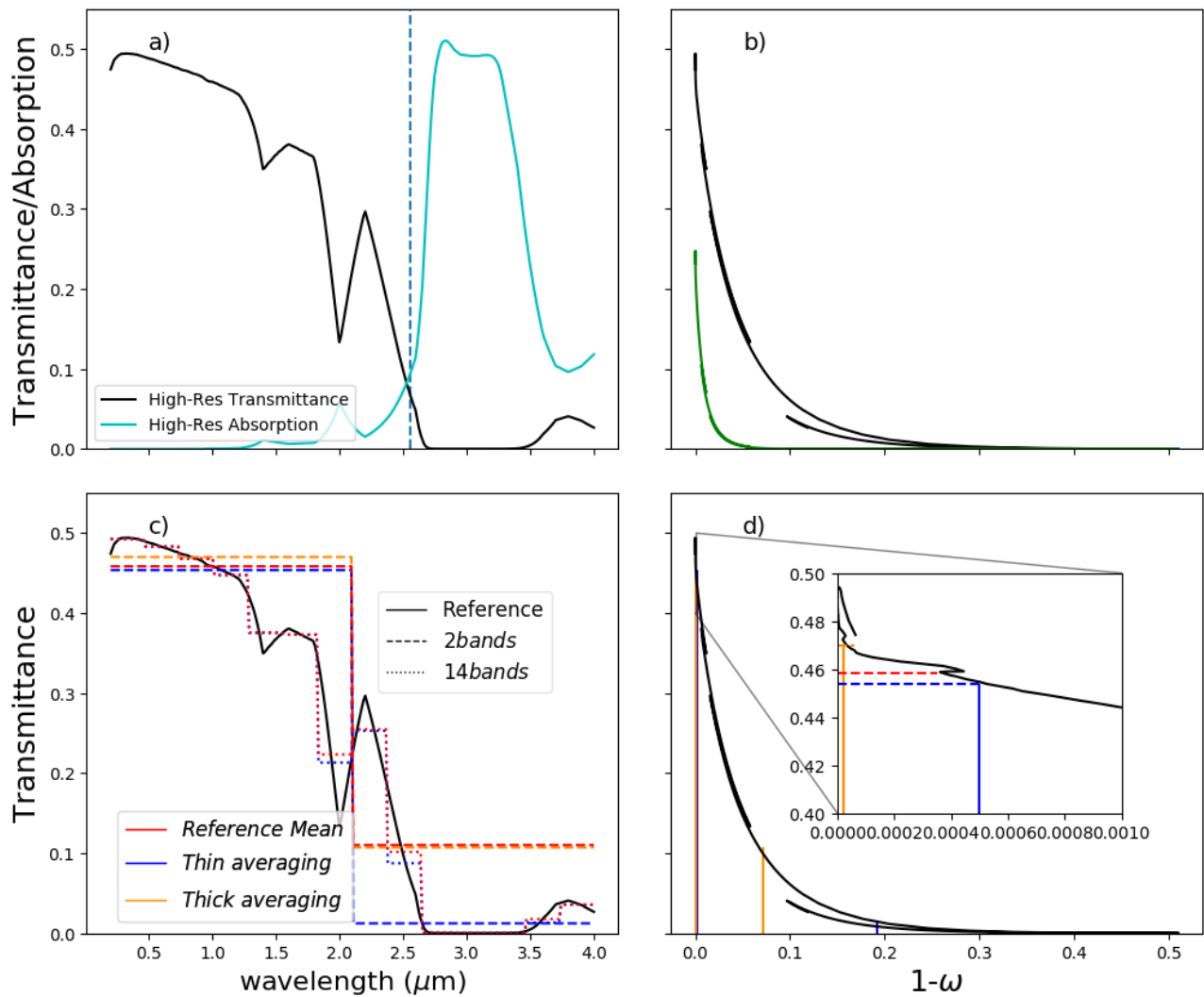


Figure 3.10: For a cloud with optical thickness of 10 having log-normal DSD with $\sigma=0.35$ are shown in a) The transmittance and absorption computed for 280 wavelengths (called high resolution) in SW. The dashed vertical line indicates where $\frac{dT}{d(1-\omega)}=1$. b) The high-resolution transmittance versus absorption for a cloud of $\tau=30$ in green and $\tau=10$ in black line c) The mean reference (in red) and thin averaging-related (in blue) transmittances for two and 14 bands configurations (illustrated with complete and dashed lines respectively) d) Same as b) with thin and thick averaged absorption for two bands configuration indicated in orange and blue vertical lines. In zoomed parcel, red, orange, and blue dashed horizontal lines represent the reference, the thick and thin averaging-related transmittances, respectively.

Chapter 4

Sensitivity of Meso-NH simulations to cloud optical properties

4.1 Introduction

In chapter 3, using offline radiative transfer simulations, we highlighted the impact of the DSD shape on the cloud radiative effect through the parameterization of cloud optical properties. Different LWC and N values were tested that could correspond to various microphysical conditions. However, since the simulations were offline, we could not outline any feedback of the radiative differences on the dynamics and microphysics of the cloud. In addition, it is worth noting that a temporal simulation has some memory. It means that a minute modification on the radiation (or other components of the cloud) resulting from a change of DSD shape at one point may not appear instantaneously but can develop in the following time steps of the simulation. To investigate this, we perform a series of 1D (single column) simulations with the Meso-NH atmospheric model in the present chapter. The radiative code used in Meso-NH is ecRad, as explained in Section 2.2, and the liquid cloud optical properties are computed with our new parameterizations. The advantage of using these parameterizations is two-fold. First, because the DSD shape is one of the input parameters of these parameterizations, the DSD shape assumed in the microphysics scheme can be directly prescribed to derive consistent optical properties. Furthermore, the new parameterizations allow the estimation of the uncertainty due to the DSD shape assumption, similar to what was done offline. Thereupon, we can trace the DSD shape uncertainty footprint on the cloud profile evolution throughout the simulations. The chapter is organized as follows. First, the real case on which the 1D Meso-NH simulations are based is presented. Next, the input parameters of our Meso-NH simulations are explained. The information on the main setups, based on the DSD shape choice in optical properties parameterizations and microphysics scheme, are also detailed. We then analyze the impact of changing the DSD shape in a reference simulation, excluding the effect of DSD shape on the LW optical properties. Thereafter, we allow the DSD shape to impact LW optical properties and highlight the differences with the reference simulation.

4.2 FIRE stratocumulus case

As highlighted in the literature, subtropical stratocumuli are one of the primary sources of uncertainties in climate modeling due to their substantial radiative impact (Bony et al., 2006;

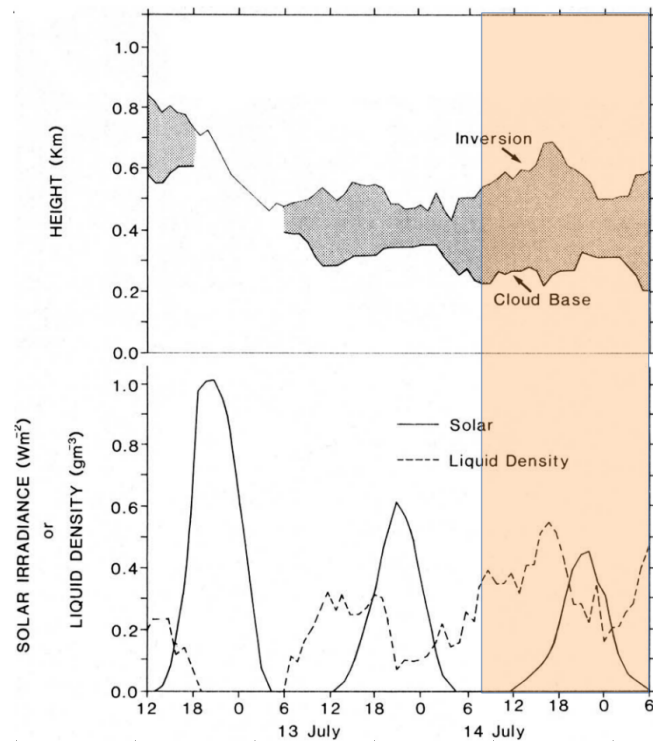


Figure 4.1: Observations for 13-14 July on San Nicolas Island. Upper panel: cloud height from ceilometer data and acoustic-sounder. Lower panel: solar irradiance from an Eppley pyranometer and cloud liquid-water path from a microwave radiometer. Figure reproduced from Albrecht et al. (1988). The orange shadow indicates the portion that will be simulated in this chapter. Time is in UTC.

Vial et al., 2013; Gettelman and Sherwood, 2016; Zelinka et al., 2020). In this chapter, we focus on an extensive stratocumulus deck persisting for several days in July 1988, off the coast of California. This cloud has robust in-situ and satellite observational support carried out during the First ICCP Regional Experiment FIRE Albrecht et al. (1988). The stratocumulus forms where moisture from the surface is already available through the well-mixed planetary boundary layer (PBL) by the turbulence (Wood, 2012), and it extends vertically up to the inversion layer at the top of the PBL. The cloud exhibits a remarkable diurnal cycle. The radiative cooling at the cloud top at night maintains the turbulence. This cooling is due to the LW emission of cloud droplets at the top of the cloud. After sunrise, the SW impinging on the cloud top offsets part of the LW cooling, destabilizing the cloud. In these conditions, the dry air from above the inversion layer is entrained into the cloud layer, and the evaporation accelerates, sagging the cloud top. SW penetrates the cloud and alters the heating rate profile. This gradually results in a stable and stratified layer beneath the cloud and decouples the moisture mixing from the surface. Figure 4.1 illustrates this diurnal cycle for three days acquired from the observations reported by Albrecht et al. (1988). In this study, we aim to simulate the July 14th cloud evolution (highlighted by the orange shadow in Fig. 4.1). In this figure, the time is in UTC and the local solar time is 7 hours behind the UTC.

4.3 1D Simulation Configurations

Although the Large-Eddy Simulations (LES) of the FIRE case are known to be closer to the observations than the 1D simulations (Duynderke et al., 2004; Brient et al., 2019), here we only use 1D simulations. Indeed, this chapter aims to carry out as many scenarios as possible to study the impact of the DSD shape in a real case simulation, which is hardly feasible in LES mode due to the computation time constraint.

4.3.1 Common setup of the simulations

The Meso-NH options common to all the simulations used in this chapter are detailed hereafter. The options which define the distinct scenarios are presented in Section 4.3.2. The time step is 120 seconds. To deal with the transport by advection, a 4th order scheme centered on space (just vertically because this is a 1D simulation) and time, named "CEN4TH" is applied. The 2-moment microphysics scheme LIMA (Vie et al., 2016), in the warm phase, is employed with CCN activation. The aerosol population is composed of continental aerosols, following a log-normal PSD (with a modal diameter of 40 nm and a spectral width of 3.19), and the concentration is fixed at 842 cm⁻³. The radiative cooling is not taken into account explicitly in the CCN activation parameterization, so the radiative effects will only be accounted for indirectly through temperature changes. The values of α and ν of the DSD (Eq. 2.35) can be adjusted in the input parameters of LIMA, as will be detailed in 4.3.2.

The Tripleclouds solver (Shonk and Hogan, 2008) is selected to handle the radiative transfer equations in both LW and SW. The SSPs in the SW and LW are computed using our new parameterizations and SOCRATES parameterization. In all our simulations, the surface temperature (the surface of the ocean, SST) is prescribed and fixed in time. It means that modifications of the downwelling SW flux will only affect the heating rate but will not affect the surface temperature, which limits the feedback.

4.3.2 Varying part of the setups

The DSD shape is the key parameter we aim to modify to create different simulation setups. It impacts the simulations at three levels: 1- The DSD used in LIMA; 2- The effective radius estimation; 3- The SSPs parameterization. The combination of the last two parameterizations determines the optical properties of the cloud. It should be recalled that our new parameterizations offer the possibility to define the DSD shape for the SW SSPs parameterization. In practice, a new option is added to the Meso-NH r_{eff} calculation methods that allow the user to choose the DSD. Then it reads the LWC and N directly from LIMA and computes the effective radius according to the Eq. 5 of the article (Chapter 3). It should be emphasized that, among the mentioned levels, we do not concentrate on the DSD shape changing in LIMA. As it will be shown later in section 4.4.3 activating the rain and sedimentation, which are the DSD shape-dependent microphysical processes in our 1D simulations, avoids the steady formation of the stratocumulus.

As mentioned before, in LIMA, only the Gamma distribution (Eq. 2.35) is available to describe the DSD shape. Setting the value of α to 1, Eq. 2.35 becomes the generalized Gamma function used in deriving SSPs parameterization (Eq. 4 of the article in Chapter 3). The λ in Eq. 2.35 being equivalent to $1/r_n$ in Eq. 4 of the article. On the other hand, as detailed in Chapter 3, eight DSD shape choices are available for the SSPs parameterizations where four of them

Table 4.1: Different Configurations based on the choice of DSD shape in LIMA, SSPs and R_{eff} parameterizations

	LIMA	R_{eff} for SW	R_{eff} for LW	SSP	Microphysics options
Consistent-LWOff	Consistent	Consistent	k from Martin et al. (1994) approach	Consistent	
Consistent	Consistent	Consistent	consistent with SW R_{eff}	Consistent	
Just-Reff	$\nu = 30$	$\nu = \{1, 5, 15, 30\}$	consistent with SW R_{eff}	$\nu = 30$	
Just-SSP	$\nu = 30$	$\nu = 30$	consistent with SW R_{eff}	$\nu = \{1, 5, 15, 30\}$	
Just-Lima	$\nu = \{1, 5, 15, 30\}$	$\nu = 30$	consistent with SW R_{eff}	$\nu = 30$	
Sed	$\nu = \{1, 5, 15, 30\}$	$\nu = 30$	consistent with SW R_{eff}	$\nu = 30$	Sedimentation activated
Rain+Sed	$\nu = \{1, 5, 15, 30\}$	$\nu = 30$	consistent with SW R_{eff}	$\nu = 30$	Rain and sedimentation activated

correspond to four shapes of the mentioned generalized Gamma function: $\nu=1,5,15,30$. Hence in the following, these four ν values are used as input in each of three aforementioned steps to document the sensitivity to the DSD shape.

The first setup employs the same ν in LIMA and for the optical properties. However, it must be noted that the change of r_{eff} via the DSD shape will also impact the LW optical properties. An additional modification is applied in Meso-NH code to avoid this side effect, which allows distinguishing the r_{eff} parameterization used in the LW and SW. For this reason, in the first setup, the r_{eff} used to compute LW SSPs is derived from the method proposed by Martin et al. (1994) (Eq. 5 of the article, using the k values proposed by Martin et al. (1994), independently of the k value used to compute r_{eff} for SW SSPs). This configuration is the reference model and is named *Consistent-LWOff*. The second experiment, called *Consistent* is similar to the reference but applies the same r_{eff} in both LW and SW SSPs.

One of the main objectives of Chapter 3 was to separate the SSP-related and r_{eff} -related uncertainties (see Section 4.1 of the article for more details). To complement these experiments, in this chapter we added two more sensitivity tests on the basis of the *Consistent* simulation, namely *JustReff* and *JustSSP*. The value of ν in *JustReff* simulations is fixed at $\nu = 30$ in the inputs of LIMA and SSPs parameterization, but varies in the r_{eff} estimation. In the *JustSSP* simulations, $\nu = 30$ in the LIMA and r_{eff} estimation, but varies in SSPs parameterization. The last simulation is called *JustLima*, where the focus is just on changing ν in LIMA but keeping $\nu = 30$ for r_{eff} and SSPs parameterizations. The details of all these setups are listed in Table 4.1.

4.4 Results

Four simulations corresponding to the four different ν values were performed for each setup. The results are detailed for the simulations *Consistent-LWOff*. Then only the differences between distinct simulations are outlined in Section 4.4.2.

4.4.1 Impact on LW r_{eff} estimation excluded

The 26-hour evolution of the vertical profiles of the liquid water mixing ratio, downwelling SW radiation, and potential temperature for the reference simulation *Consistent-LWOff* with $\nu = 1$ are shown in Fig. 4.2 (the time axis indicates the local solar time). Figure 4.2 demonstrates that the diurnal cycle pattern reported in the observations (Fig. 4.1) is roughly captured by the 1D simulation with the formation and maintenance of the cloud by thermal cooling at the top and strong potential temperature gradient during the night, resulting in maximum

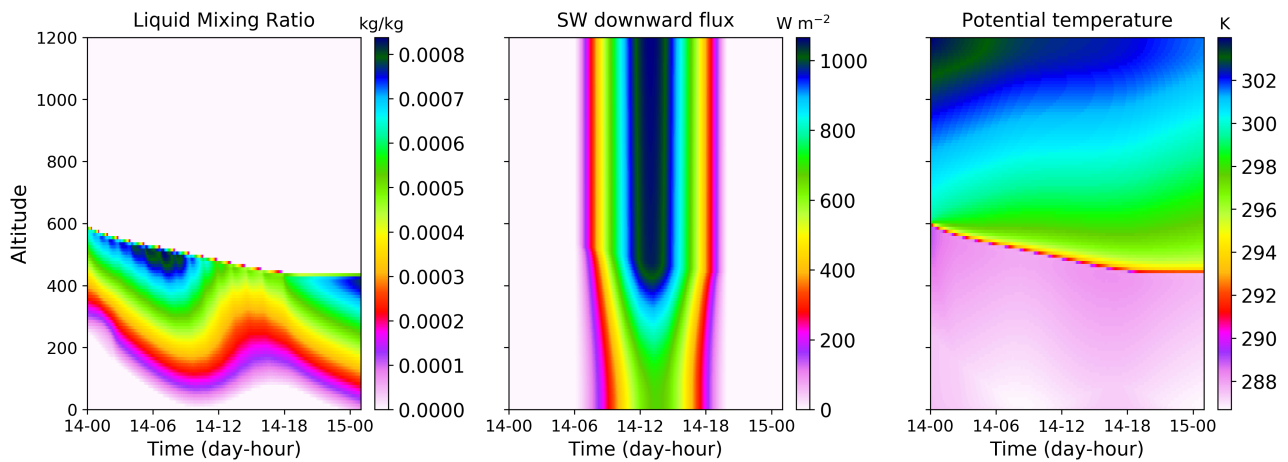


Figure 4.2: Time series of vertical profiles of liquid mixing ratio, SW_{\downarrow} flux and potential temperature, for the simulation '*Consistent-LwOff*' and $\nu=1$.

thickness just before the sunrise. Afterward, the cloud is the thinnest at about 13:00 when the SW down is maximum. For the water content time-series, the oscillatory behavior is detected in Fig. 4.2.

To understand how the DSD shape's choice changes the cloud's physics, we look at the hourly vertical profiles outputs for two extreme DSD shapes, $\nu = 1$ and $\nu = 30$ (Fig. 4.3). These profiles include the liquid water mixing ratio, the effective radius, SW downward fluxes, the SW/LW heating/cooling rates, and the temperature for nine consecutive hours beginning just before sunrise at 6:00 up to the maximum insolation at about 14:00.

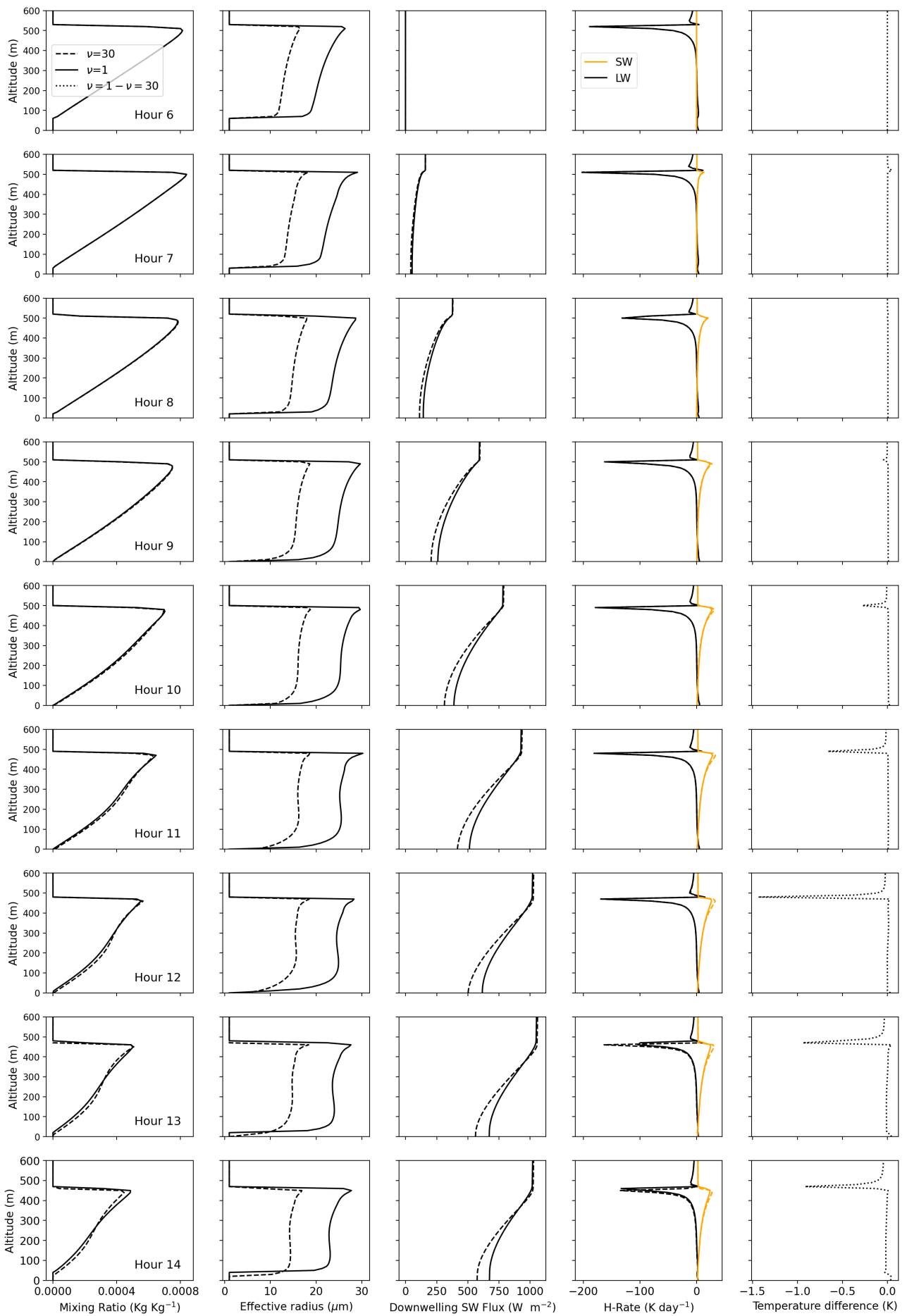


Figure 4.3: The evolution of liquid water content, r_{eff} , downwelling SW radiation, heating rate and temperature differences between $\nu = 1$ and $\nu = 30$ profiles four 9 hours of the *consistent-LwOff* simulations. For all the figures the dashed and full lines indicate the profiles obtained for $\nu = 30$ and $\nu = 1$, respectively, and dotted lines indicate the difference between both values of ν .

We first describe the variables that are directly affected by the change in DSD shape. Then we detail subsequent secondary effects and feedbacks.

Direct impacts

The first consequence of switching the DSD shape from $\nu = 1$ to $\nu = 30$ is to decrease r_{eff} by a factor of 2. This can be explained by looking at Fig. 4.6 (this is the extension of Fig. 1b of the article, which was created for the log-normal distribution case) where the r_{eff} -LWC relation is displayed based on Eq. 5 of the article, with k values corresponding to the four gamma functions ($\nu = 1, 5, 15, 30$), assuming $N=300 \text{ cm}^{-3}$ (the same result can be obtained for other values of N). It indicates that for a given liquid water content r_{eff} is smaller for $\nu = 30$ than for $\nu = 1$, and consequently, the optical depth of the cloud is higher, and hence, downwelling solar radiation is lower for $\nu = 30$ simulation. For the same reason, more absorbed SW, thus more significant heating rates, are observed for $\nu = 30$ after about 10:00. However, looking at the temporal evolution of the profiles, we realize that as the absolute values of the LWC decrease, the difference between 2 DSD shapes simulations in downwelling SW and heating rate grows. For the SW \downarrow this is consistent with the results of Fig. 9 of the article, which demonstrated the DSD-related uncertainties in transmitted, reflected, and absorbed flux for different values of LWC for an ideal case cloud. This figure inferred that the highest uncertainties in transmitted SW are obtained for the lowest LWC amounts. The heating-rate behavior is also aligned with what was observed in the 1D real case simulations in Fig. 10 of the article. It shows that more considerable heating rate uncertainties were observed for the clouds with lower values of LWC. However, the impact of the DSD shape on temperature, LWC and the LW cooling differences can not be explained directly by the differences in r_{eff} . Therefore, we further explore these variables below.

Secondary effects and feedbacks

Altering the ν value does not affect the LWC profiles until after 11:00. Thereafter, the upper and lower parts of the cloud exhibit distinct behaviors. Moreover, the cooling rate difference between the shapes reaches its maximum at the first upper layers of the cloud, at 13:00. To provide a more in-depth insight of this issue, the cloud top region above 400 m and the cloud base region, below 400 m are shown in Figs. 4.4 and 4.5, respectively, for the 11:00 to 14:00 time interval. Focusing on the cloud-top in Fig. 4.4 and comparing the LWC profile at 12:00 and 11:00, we realize that the liquid water content of both $\nu = 1$ and $\nu = 30$ cases are depleted simultaneously for the fourth layer from the top of the graph. At hour 13, though, the 5th layer from the top in $\nu = 30$ LWC profile becomes water-free while the $\nu = 1$ at the same level has lost only half of its water content. In other words, the cloud-top height becomes one model level lower in $\nu = 30$, a process that is delayed for the simulation with $\nu = 1$. This mechanism roughly persists at hour 14 at the 6th layer from the top, but this time a trace of water also remains in $\nu = 30$. The profile of LW cooling is tightly linked with this LWC change. Before detailing the LW cooling rate variability, it is worth recalling some basics. The emissivity, ϵ , of a cloud essentially depends on its optical depth τ as:

$$\epsilon = 1 - e^{-\tau}. \quad (4.1)$$

This relation holds up to a layer from the top, where the cloud becomes optically opaque. LW is totally absorbed, arriving at this layer. It can be assumed that the cloud in this layer emits approximately as a blackbody, $\epsilon \approx 1$ (Vaillant de Guélis et al., 2017) (which means the amount

of emitted radiation will depend only on the cloud temperature according to Planck’s law). As shown by Vaughan et al. (2009), this emitting layer’s cumulative SW optical depth is about 3 to 5. Looking at the integrated τ profiles (from cloud top), shown in the last column of Fig. 4.4, for our case, $\tau = 3$ is obtained at about 350 m. We denote this opaque layer with OP and the layer above it with $OP + 1$. The OP emits LW upward and downward as a blackbody. It receives roughly the same amount of energy from $OP - 1$ but receives less energy from $OP + 1$, since the emissivity of $OP + 1$ is lower. Hence overall, OP cools. It should be recalled that the value of τ indeed involves the total water content from the top to that layer. Therefore, going upward from OP , using Eq. 4.1, ϵ shrinks as τ decreases. This enhances the cooling, up to the first layer of the cloud, $OP + i$, where a certain amount of liquid water is available. This is why at 13:00, we do not observe the same cooling maximum of $\nu = 30$ profile in $\nu = 1$. The cloud in $\nu = 30$, having more liquid water in the top layer than $\nu = 1$, experiences considerably more cooling in this layer. While in the $\nu = 1$ case, the maximum cooling is distributed in the two topmost layers.

4.4.2 Impact on LW r_{eff} estimation included

Here we point out first the main differences between the two setups which include and exclude the DSD shape impact on the effective radius estimation in the LW optical properties estimation, namely *Consistent*, and *Consistent-LwOff*. Next, focusing on the *Consistent* setup, we highlight the effects of DSD shape in SSPs and r_{eff} separately as we did in chapter 3.

To provide a general vision of the contrast between *Consistent* and *Consistent-LwOff*, we illustrate in Fig. 4.7, the difference between the simulations of 2 DSD shapes in LWC, SW_{\downarrow} and potential temperature profiles time-series for both setups.

Comparing the setups reveals that for the *Consistent-LwOff* case, during the day (between 07:00 and 19:00), the LWC is removed in the lower portions of the cloud while added at the upper sides as we shift the DSD from $\nu = 30$ to $\nu = 1$. This behavior is reversed and enhanced for the *Consistent*. The differences between the two shapes at the cloud top for both setups are 2-3 times greater than the middle and lower parts of the cloud. This is because of the delayed cloud top height change for $\nu = 1$, as pointed out earlier. The number of vertical grids affected by the cloud change is always one in *Consistent-LwOff* and reaches up to 3 model grids in *Consistent* simulation.

To investigate the more detailed contrast between *Consistent* and *Consistent-LwOff* we show the differences between two DSD shapes ($\nu = 1 - \nu = 30$) for these two setups in terms of LWP and surface SW_{\downarrow} time series, in Fig. 4.8.

The first remarkable point is that the differences between the two DSD shapes are perceptible in LWP of *Consistent* during the night and hours before *Consistent-LwOff*. Just before sunrise, we observe 0.03 kg m^{-2} more LWP difference in *Consistent*, which indicates that the purely LW effect is significant. This is equivalent to 10 % of the $\nu = 1$ simulation LWP value. The residual LWP differences that remain after 19:00 in *Consistent-LwOff* setup quantifies indeed the purely SW effect on the LWP of the cloud, which is about 4% of the $\nu = 1$ LWP. Similarly, the residual for *Consistent* case reaches up to 20%, combining both LW and SW effects.

After the sunrise, the LWP difference trends are opposite in the two setups. The oscillations are present in both setups, being larger in *Consistent-LwOff*, but characterized by a lower fre-

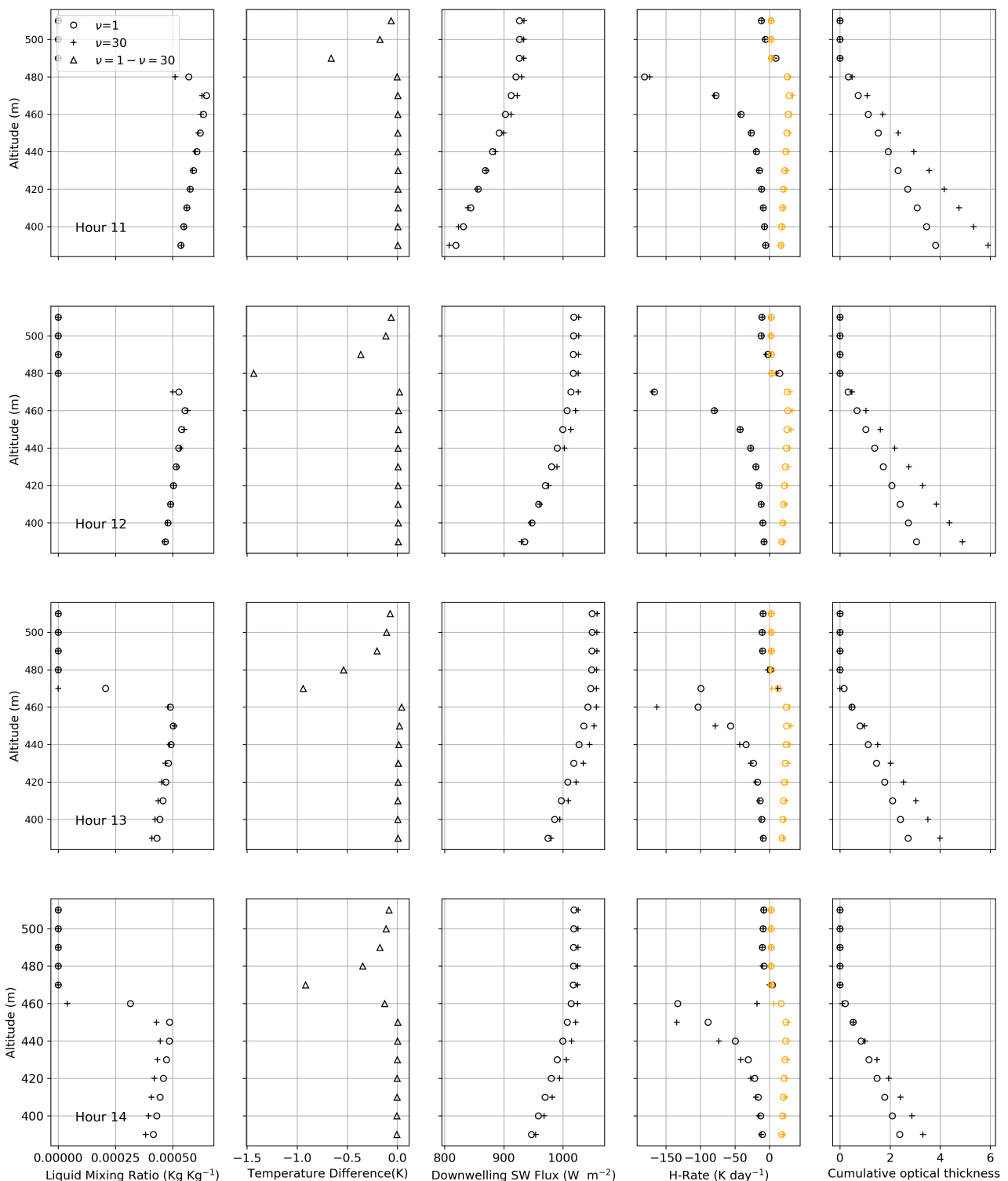


Figure 4.4: Same as 4.3, for the upper part of the cloud above 400 m. The last column shows the integrated optical depth from cloud top, and second column indicates the temperature differences between the clouds of two DSD shapes.

quency than *Consistent*. It is speculated that the fluctuations observed in *Consistent-LwOff*, which are solely SW-related effects, offset a part of the LW effect in the *Consistent* setup.

Interestingly *Consistent* indicating more LWP difference, has lower surface SW_{\downarrow} irradiance

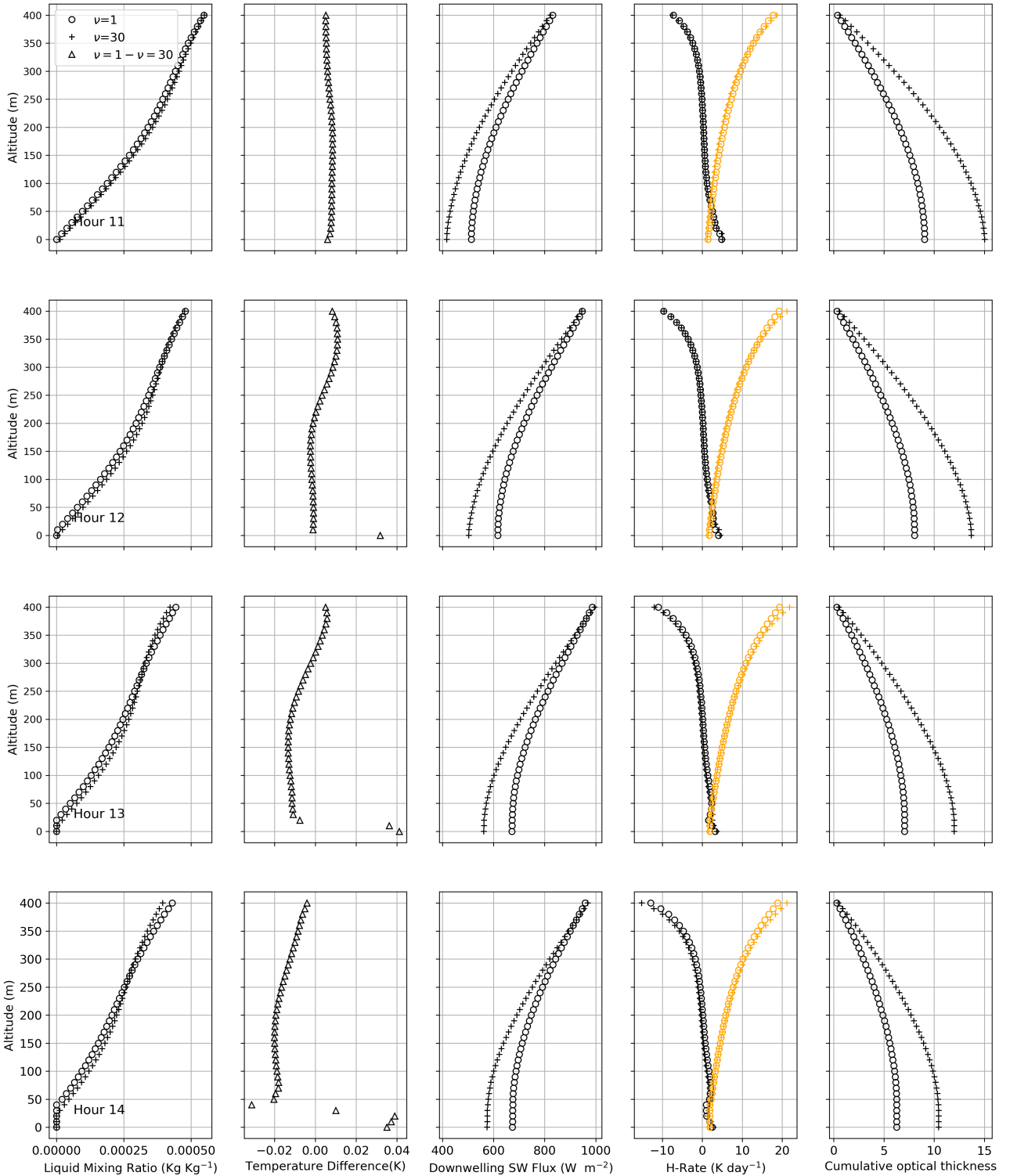


Figure 4.5: Same as 4.4, but for the lower part of the cloud below 400 m.

differences. To understand this issue, we have extracted and illustrated in Fig. 4.9 the vertical profiles of LWC, r_{eff} , the number concentration, N , and the SW_{\downarrow} at 14:00 where the differences of the surface SW_{\downarrow} is maximum.

From the LWC amounts, it is discernible that the LWP does not change notably in *Consistent-LwOff*, but the profile varies as the result of DSD shape changes. As pointed out earlier, generally, for both setups, the cloud with $\nu = 30$ is more opaque since it has smaller droplets than

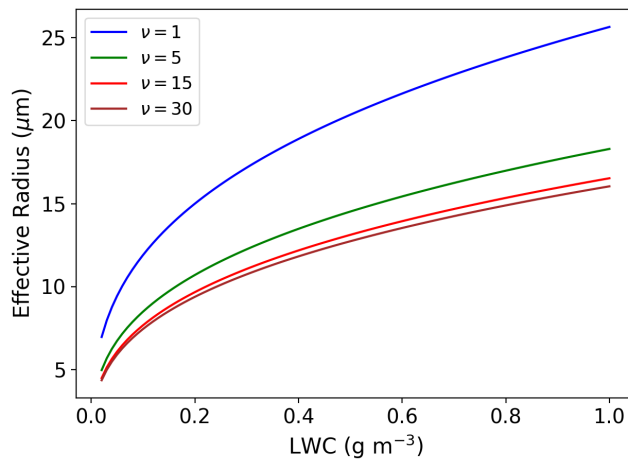


Figure 4.6: r_{eff} -LWC relation derived for 4 gamma distribution shapes: $\nu = 1, 5, 15, 30$, derived from Eq. 5. of the article

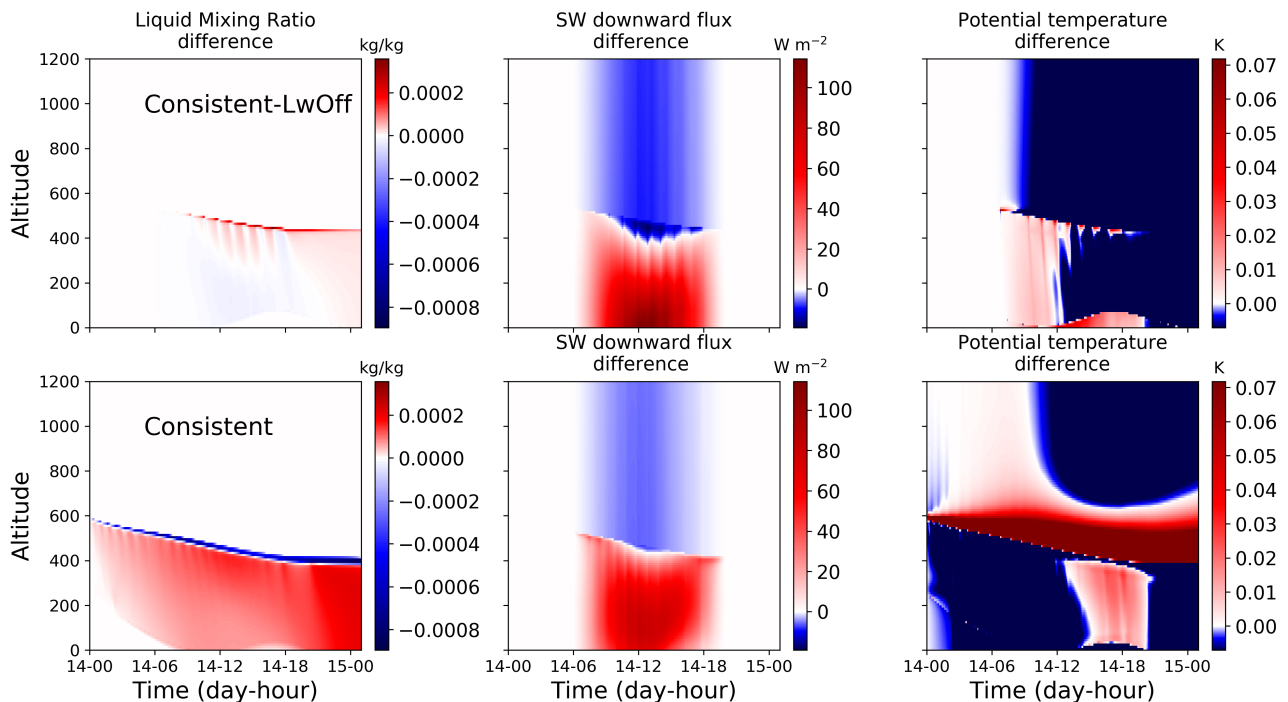


Figure 4.7: Difference between $\nu = 1$ and $\nu = 30$ for time-series of LWC, SW_{\downarrow} , and the potential temperature of *Consistent* and *Consistent-LwOff* setups.

the cloud with $\nu = 1$, letting a lower amount of SW_{\downarrow} reach the surface. The main question of more differences in surface SW_{\downarrow} in *Consistent-LwOff* despite its lower LWP difference is once again highlighted. It can be realized that most of this SW_{\downarrow} contrast stems from the difference of SW_{\downarrow} for $\nu = 1$ simulation between both setups. Hence we will focus on analyzing only the $\nu = 1$ cloud profiles for both setups. r_{eff} profiles do not show the same size pattern in both setups for the cloud. The size reduces toward the bottom of the cloud in *Consistent* while it remains roughly constant through the cloud in *Consistent-LwOff*, being approximately equivalent to the mean value of the r_{eff} of *Consistent*. Therefore we expect the radiation to be impeded more in lower regions of $\nu = 1$ cloud in *Consistent* than *Consistent-LwOff*. This behavior is further intensified regarding the N profiles. The number of smaller particles in the lower part

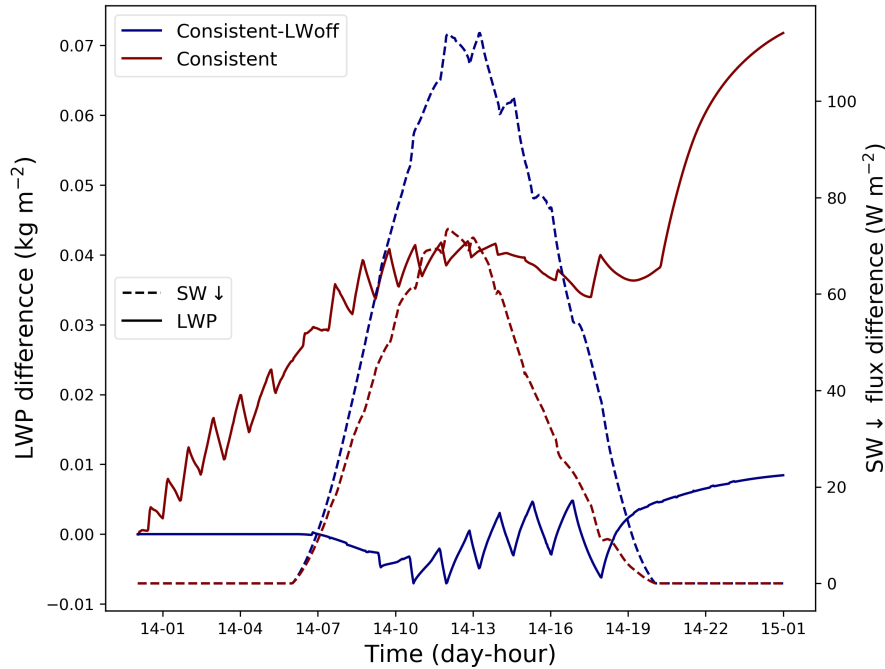


Figure 4.8: Differences between $\nu = 1$ and $\nu = 30$ for time-series of LWP and surface SW_{\downarrow} of *Consistent* and *Consistent-LwOff* setups.

of $\nu = 1$ cloud in *Consistent* is drastically greater than its counterpart in *Consistent-LwOff*. Consequently, more differences between two DSD shapes are obtained for the surface SW_{\downarrow} in *Consistent-LwOff*.

Finally, to distinguish the effects of DSD shape in SSPs and r_{eff} , we demonstrate the results of the *JustReff* and *JustSSP* setups which are the derivatives of *Consistent* experiment respectively in Figs. 4.10 and 4.11. The features of the simulations are detailed in section 4.3.2 and can be found in Table 4.1. The figures illustrate the difference between the simulations corresponding to $\nu = 1$ and $\nu = 30$ for the time series of the liquid mixing ratio, SW_{\downarrow} flux, and potential temperature profiles for each setup.

The oscillatory behavior for the mixing ratio is in accordance with what was found for the 'Consistent-LwOff' simulations. The impact on the simulation outputs is detectable from the beginning of the simulation at night. Comparing Figs. 4.7-lower row, 4.10 and 4.11 reveal that a substantial part of the differences in the *Consistent* simulations are due to the DSD shape effect in r_{eff} estimation. The DSD shape impact in SSPs, as shown in Fig. 4.11 offsets about 10 to 20% of r_{eff} related impact, respectively in SW_{\downarrow} and water content profiles. These findings are consistent with the results of the offline study in Chapter 3.

4.4.3 Perspective: Impact on microphysics activated

Until here, we have studied how the DSD shape's choice can alter the cloud's temporal profiles without accounting for any direct impact of the DSD change on microphysics. To ensure this, we fulfilled the simulations for *JustLIMA* setup. The outputs confirmed zero differences between two DSD shapes for this setup. This section provides preliminary results of activating the sedimentation and rain in our *JustLIMA* setup. In these simulations, the DSD shape choice

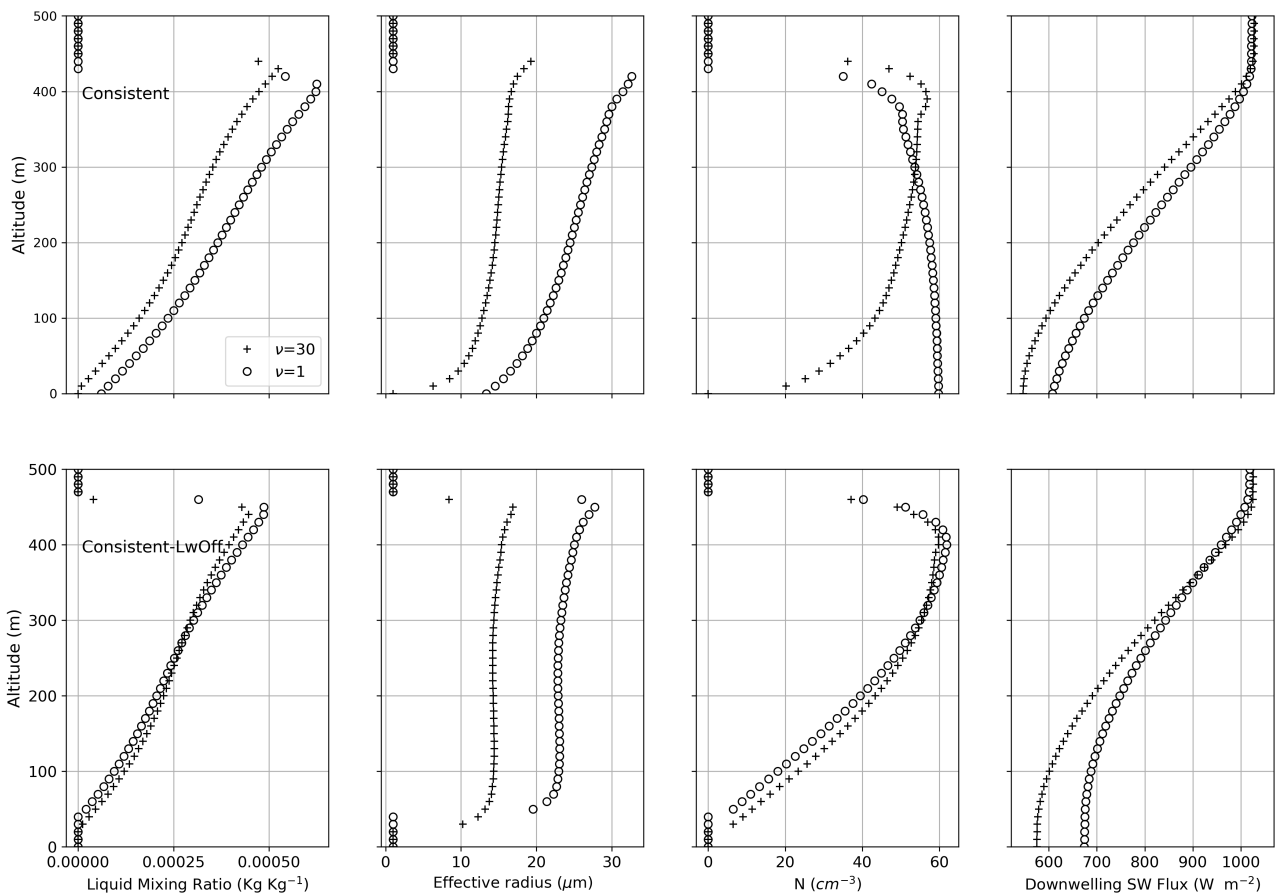


Figure 4.9: The profiles of LWC, r_{eff} , the number concentration, N , and the SW_{\downarrow} output from two simulations associated to $\nu = 1$ and $\nu = 30$ for *Consistent-LwOff* and *Consistent* setup extracted at 14:00

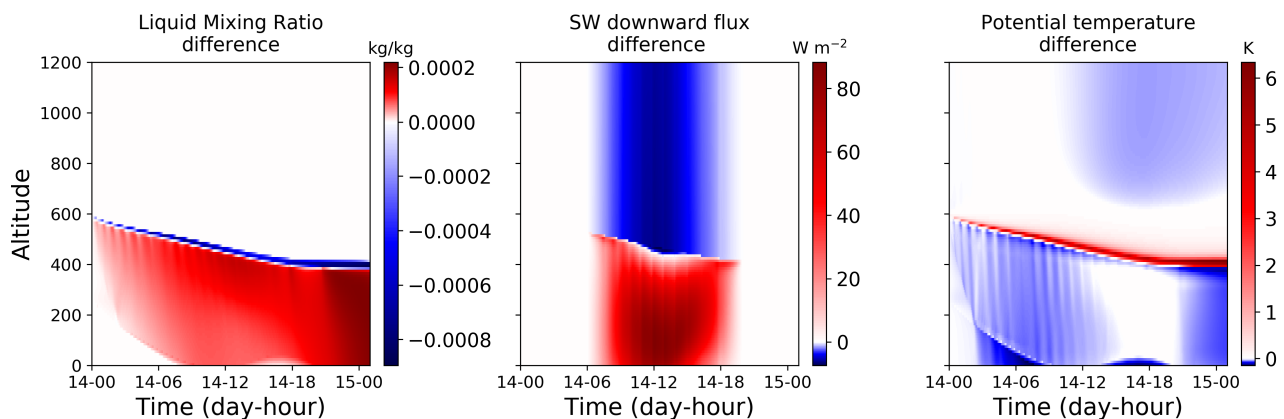


Figure 4.10: Difference between $\nu = 1$ and $\nu = 30$ for time-series of liquid mixing ratio, SW_{\downarrow} flux and potential temperature profiles, for 'JustReff' setup

($\nu = 1, 5, 15, 30$) only affects the microphysics, and ν is fixed in the optical properties estimation. Figures 4.12 and 4.13 illustrate respectively the evolution of time series of the vertical profiles outputs, for the simulations where only the sedimentation (*Sed*), and both sedimentation and rain (*Sed+rain*) are activated. As observed, activating sedimentation causes the narrowing and dissipation of the cloud. This dissipation gradually shifts toward the first hours

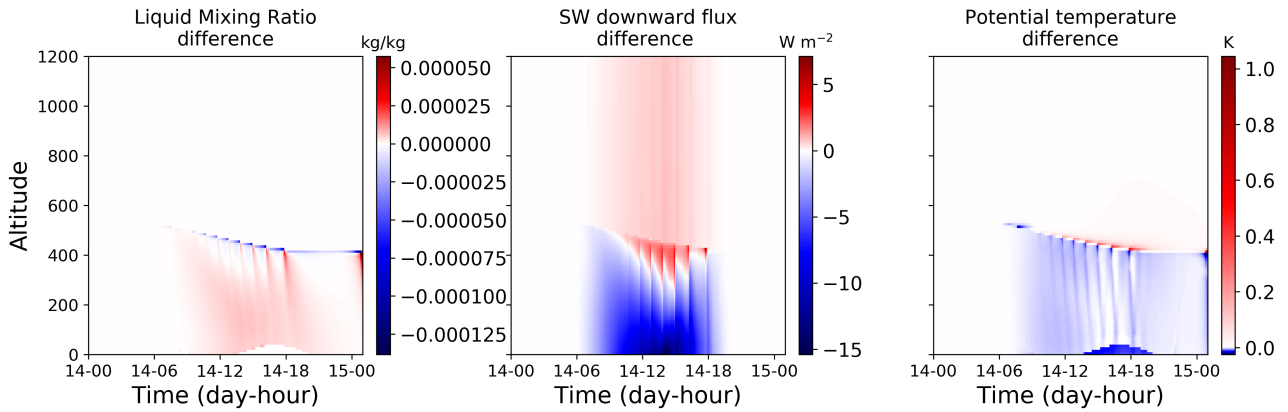


Figure 4.11: Same as 4.10 but for 'JustSSP' Setup

of the simulation as we move from $\nu = 1$ to $\nu = 30$. Adding rain to the sedimentation will remove the gradual change. The cloud dissipates an hour after sunrise for all ν values.

These results are the motivation to foster this study of the DSD shape impact on microphysics. Furthermore, tests must be carried out by activating the radiative-related direct impacts on the microphysics, such as considering the effect of the radiative cooling on condensational growth of the cloud droplets and supersaturation profiles. These studies can uncover more aspects of the microphysics-radiation interaction and feedback resulting from the DSD change.

4.5 Conclusion

In the previous chapter, offline radiation simulations were carried out to assess the impact of DSD shape choice on cloud optical properties (effective radius and SSPs parameterization). In the present chapter, this offline study is extended to full 1D online simulations.

In the previous chapter, offline radiation simulations were carried out to assess the impact of DSD shape choice on cloud optical properties (effective radius and SSPs parameterization). In the present chapter, this offline study is extended to full 1D online simulations.

The advantage of such a study is to assess the possible feedback of purely radiative DSD-related uncertainty on the other model components, such as microphysics or turbulence. For this purpose, the new SSPs parameterizations were implemented in Meso-NH, and several configurations were designed to simulate a real stratocumulus case. This allowed coupling of the DSD shape from the microphysics scheme LIMA to the SSPs and effective radius (r_{eff}) parameterization of the radiation scheme. However, the microphysical processes which depend on the DSD shape were deactivated in LIMA. Due to time constraints, we use the Meso-NH in 1D mode instead of LES mode. This decision, however, has a drawback. It has been demonstrated in this chapter that activating the sedimentation and rainfall in LIMA, which are DSD-related microphysical processes, avoids the formation of the stratocumulus cloud in our 1D simulations. That being said, we can still trace the footprint of DSD shape through radiative on the microphysics or turbulence. In other words, modifications in radiative fluxes and heating rates resulting from the DSD shape change can modify the vertical temperature profile, surface fluxes, and perhaps the turbulence and cloud evolution.

The simulations were performed, accounting or not, for the change of r_{eff} in the LW. The

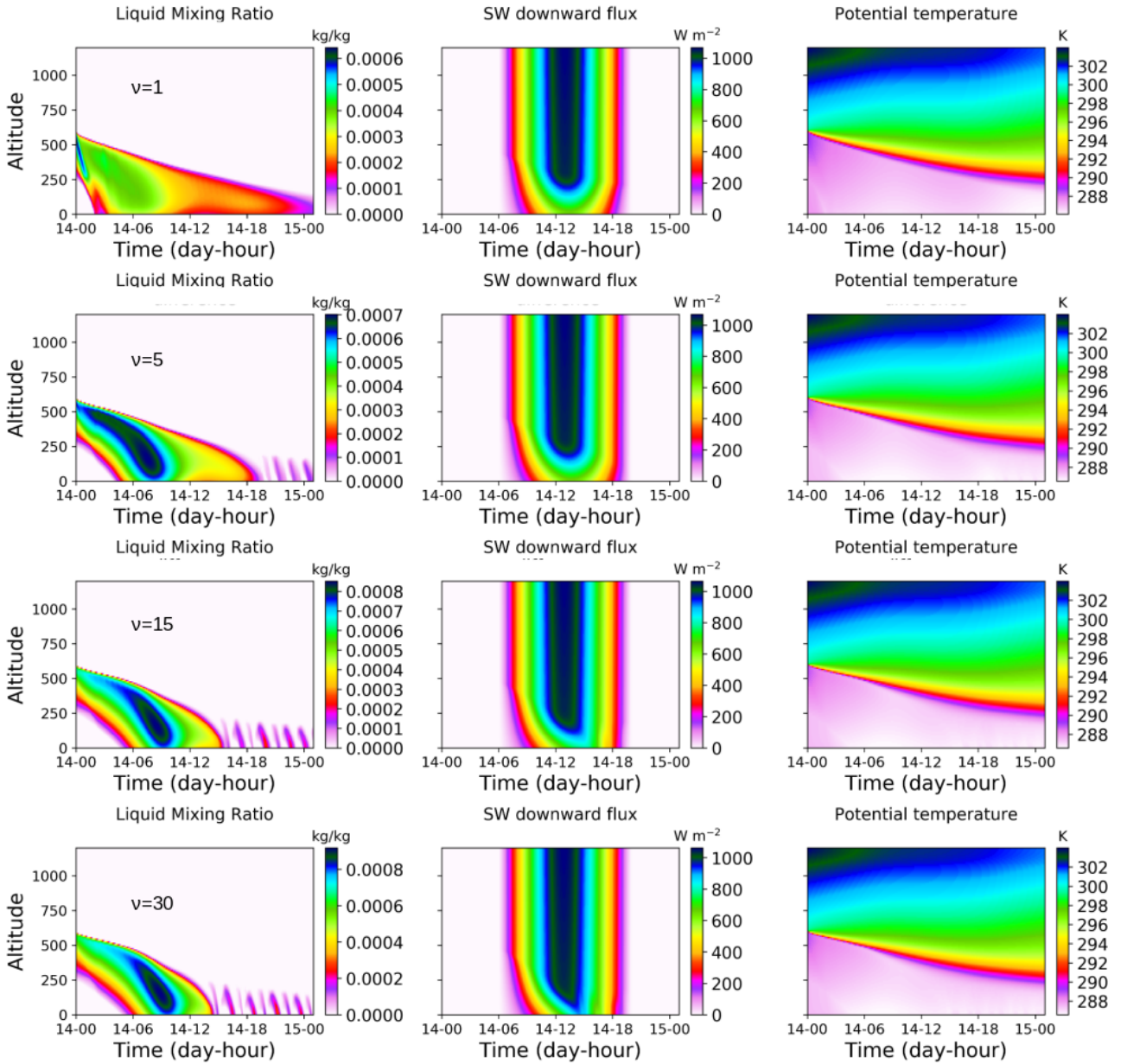


Figure 4.12: Vertical profiles time-series of liquid mixing ratio, SW_{\downarrow} flux and potential temperature, for *sed* setup for all four values of the ν

direct impacts of the DSD shape on r_{eff} , hence on the optical depth and SW_{\downarrow} fluxes, are in line with the results of Chapter 3. Regarding the indirect effects, it is revealed that, generally, the change of DSD can displace the cloud-top height by one model-grid in the absence of the LW- r_{eff} effect, and up to several vertical pixels when considering r_{eff} changes in the LW. For the latter setup, the results also highlighted that the liquid water path difference between simulations associated with two DSD shapes could reach up to 10 %, or 4% for the case where the LW- r_{eff} effect is not activated. Interestingly the latter setup, despite having a lower difference in terms of LWP, manifests higher differences of SW_{\downarrow} at the surface. The reason for this was the fact that as we shifted the DSD, smaller (larger) droplets were added at the bottom of the cloud in LW- r_{eff} allowed (not-allowed) setup. Smaller droplets mean higher optical depth and lower SW_{\downarrow} at the surface.

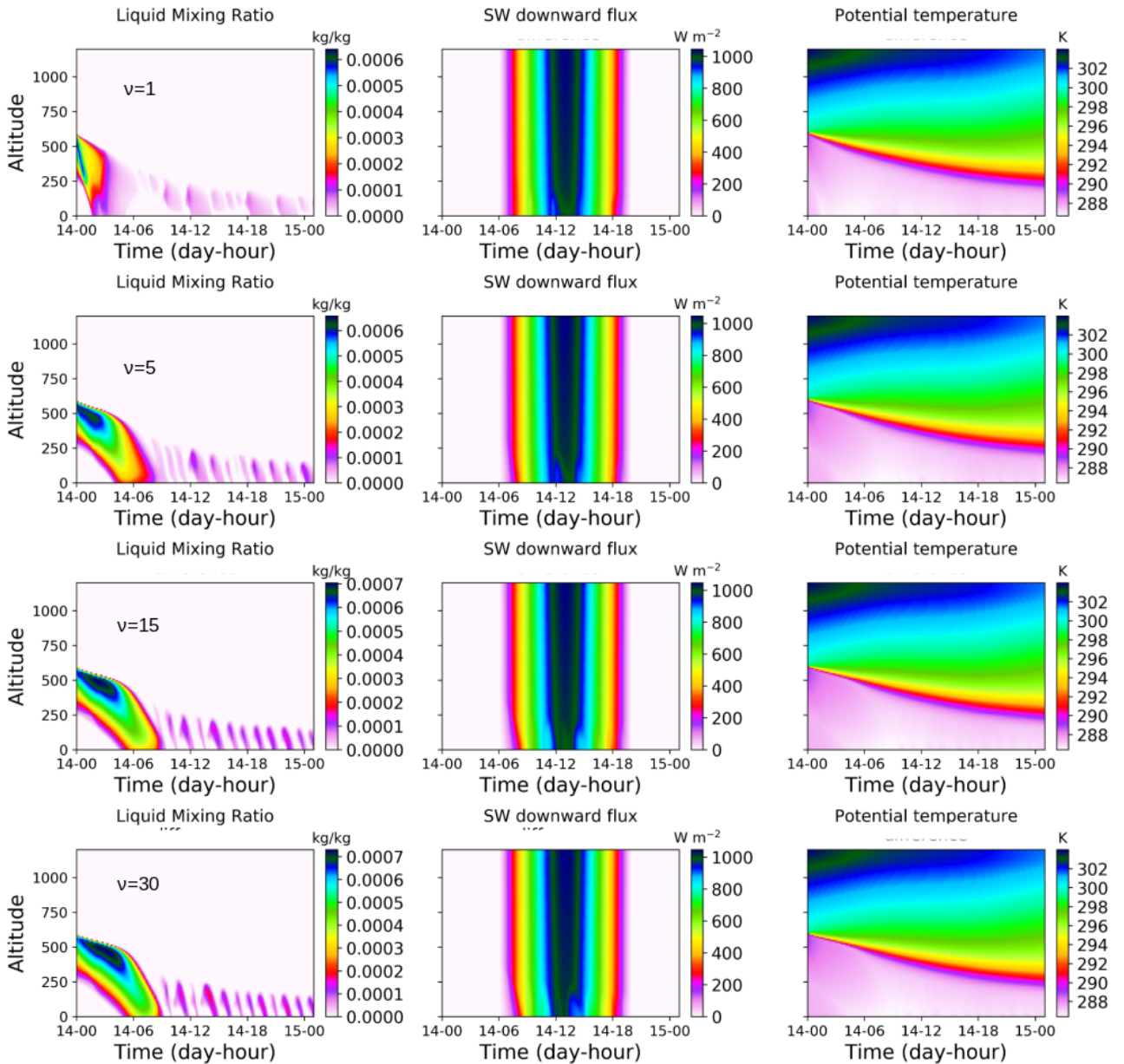


Figure 4.13: Same as 4.12 but for *sed+rain* Setup

The outcomes of this chapter propose further studies concerning several issues. As we mentioned earlier, all possible microphysical effects related to the DSD shape change were excluded in this study. In future works, a case should be chosen where the DSD shape is allowed to impact microphysics as well.

As explained, any direct radiative effect in microphysics was excluded from our study. Ackerman et al. (1995) and Mazoyer et al. (2022) highlighted the importance of the radiative impact on the supersaturation rate in activation of the aerosols to form the droplets and subsequent change in the DSD of particles in stratocumulus and fog (42 observation cases), respectively. Therefore it would be interesting to replicate the results of this chapter in future studies activating the effect of the radiation in supersaturation estimation. Regarding the two mentioned references, this may cause feedback by changing the DSD shape. In addition, as we noticed, the effective radius drives the DSD shape impact not only on the shortwave but also on the LW. This suggests that our parameterization of SSPs should be extended to the LW region of

radiation. Ultimately it is essential to understand the oscillatory pattern observed in all our simulations, especially in the LWC and LWP. Bott et al. (1990), studying a fog case, manifested that these oscillations are associated with the growth of larger droplets by radiative cooling, which leads to their gravitational settling. This can not be the reason in our case since we have deactivated the sedimentation. We speculate that changing the vertical and temporal resolution of the 1D simulations can alter the oscillatory behavior, which can be a motivation for the next investigations.

Chapter 5

Conclusion and perspectives

In climate studies, the estimation of the cloud radiative effect significantly differs between global circulation models (GCMs). In addition, in numerical weather prediction models, the surface irradiance simulations in cloudy conditions are fraught with errors. This is to some extent because clouds are not predicted at the right place and the right time compared to the observations. However, uncertainties and errors can also arise from the complex and highly variable radiative properties of clouds which can not be resolved at the grid level of an atmospheric model. This includes all radiative assumptions related to: the subgrid distribution of water or ice in a cloud, the overlap between cloudy layers, horizontal heterogeneity of the cloud fraction, the estimation of cloud optical properties. In this thesis, we focused on the parameterization of liquid clouds optical properties, which has not been revisited for about two decades. The emphasis is on the SW region, due to the significant radiative forcing of clouds in the SW, its stronger sensitivity to cloud microphysics and radiative assumptions, and its larger contribution to inter-model spread compared to the LW.

Cloud-radiation interactions take place at the droplet scale. The amount of radiation absorbed and scattered by the droplet is quantified by its single scattering properties (SSPs). These properties highly depend on the droplet size and the wavelength of the incoming light. However, this dependence can not be resolved in the grid of the model. To deal with this issue, atmospheric models rely on parameterizations that estimate SSPs following three steps: 1- For a given wavelength, the average SSPs are derived over a droplet size distribution (DSD), given its effective radius (r_{eff}) and based on an assumption on the shape of the DSD. 2- These SSPs are then averaged over the spectral bands of the radiative model. 3- Repeating these 2 steps for a range of r_{eff} , and fitting an analytical function to the results, leads to compact formulations of the SSPs in terms of r_{eff} for each spectral band. Preceding these 2 steps, the r_{eff} is usually derived from LWC and N . The computation of r_{eff} also requires assuming a DSD shape, through the parameter k , known as effective radius coefficient, which is the cubic root of mean volumic radius of droplets to r_{eff} (Martin et al., 1994). The optical properties parameterization overall involves the SSPs parameterization and the r_{eff} estimation. It is worth mentioning that the DSD shape assumptions in both steps are independent and may not correspond to the same DSD. Another assumption on the DSD shape is considered in the microphysics scheme, upon which relies the LWC prognostic. In addition to these possible inconsistencies of the DSD shape at different levels, the widely used linear averaging of the SSPs over spectral bands, where they may vary non-linearly, introduces an additional challenge to the optical properties parameterization.

The objective of this thesis was thus to investigate the uncertainty in simulated atmospheric

radiative fluxes due to the DSD shape and spectral averaging method used in the optical properties parameterization. For this purpose, a series of new parameterizations was designed, that explicitly accounts for the DSD shape. Moreover, the new parameterizations include several spectral averaging strategies. In addition, we have improved the fitting method to capture the oscillatory features of SSPs occurring for effective radii smaller than $5 \mu\text{m}$ which were missed in the most recent parameterization available in ecRad, namely SOCRATES Manners (2015). Another advantage of the latter modification was the extension of the r_{eff} validity range down to $1 \mu\text{m}$.

In the first part of the thesis the focus was on the DSD shape choice in SSPs and r_{eff} estimation and the choice of spectral averaging methods. The new parameterizations were implemented in ecRad. Then offline radiative transfer simulations were performed on various 1D profiles and outputs of a GCM, choosing different DSD shapes, and spectral averaging methods. The ideal case experiments covered clouds with various vertically uniform LWC and N values. The real cases included the horizontally averaged outputs of 4 LES simulations of case studies of fog, stratocumulus, cumulus and a congestus, having realistic non-uniform LWC profiles contrarily to the ideal case clouds. Fluxes differences between simulations associated with two DSD shapes corresponding to the 5th and 95th percentiles of the observed DSD shape values reported in Miles et al. (2000), were interpreted as the DSD-related uncertainty.

Our findings for the ideal case clouds revealed that the uncertainties in transmitted and reflected fluxes increase up to 20 and 16% respectively, as the LWP gets lower. However, this was limited to the cases where the value of N is in $80\text{-}400 \text{ cm}^{-3}$ range. The real case results however reveal that clouds with similar LWP can exhibit different uncertainties. This stems from the fact that the LWC is inhomogeneously distributed within the cloudy layer in real case, and the detailed vertical distribution is key in determining the uncertainty. In all cases, the impact of the Spectral averaging methods choice is more discernible on the absorption of the cloud than the transmittance and reflectance.

The application of our parameterization on the outputs of CNRM-CM6.1 GCM model illustrated that the overall DSD shape-related uncertainty of the TOA SW cloud radiative effect (CRE) can reach 15 W m^{-2} in the Tropics, where low-level liquid clouds are ubiquitous. The mean overall uncertainty in SW CRE is about 6.2 W m^{-2} , which is about 13 % of the observational reference value. This uncertainty is primarily due to the r_{eff} -related uncertainty, about 10 % of which is offset by the SSP-related uncertainty. The global mean effect of SSP-related contribution to CRE uncertainty is approximately -1.6 W m^{-2} .

The second part of this thesis focused on the coupling of the DSD shape between the optical properties used in the radiative code and the microphysics scheme of the atmospheric model. For this purpose, the upgraded version of ecRad embedding our new parameterizations was implemented in the Meso-NH atmospheric model. 1D simulations of the *FIRE* stratocumulus cas, which has a marked diurnal cycle, were performed by ensuring the same DSD shape is assumed in both steps of the optical properties parameterization and in the microphysics scheme LIMA. The aim was to study the possible feedbacks resulting from the interactions of DSD-related uncertainty with other components of the atmospheric model.

The results of these 1D simulations pointed out that the r_{eff} -related uncertainty is the main source of differences among simulations with distinct DSD assumption as in the offline test.

Moreover it was shown that r_{eff} -related uncertainty impact was largely generated by differences in the longwave (LW) SSPs. Therefore, for the rest of the simulations, we excluded this effect by fixing the r_{eff} used for the LW optical properties. Consequently, we obtain quantitatively the same differences between two distinct DSD shapes as in the offline tests. This holds up to a time step where no noticeable change is detected in the LWC profiles before the sunrise. After the sunrise, the DSD shape gradually affects the profiles of LWC and N and the LW cooling rate. Since r_{eff} calculation depends on N and LWC, their modification will generate a feedback on the optical properties parameterization, and consequently on the radiation. The mechanism through which these indirect effects have been generated are not trivial and would deserve further investigation.

The simulations where DSD shape also affected the LW SSPs indicated stronger effects on LWC, LW cooling and N profiles. This suggests to extend our SW optical parameterizations to the LW. IN addition we limited ourselves to the liquid clouds. To be able to explore more cloudy conditions such as ice or mixed-phase clouds it would be relevant to replicate the methodology to develop new parameterizations for ice clouds.

Concerning the irradiance simulations, we recommend the framework for a future study: 1- Choosing the DSD regarding the existing studies in this field (Brenquier et al., 2011; Tas et al., 2015; Wang et al., 2021) appropriate to the case of interest for the simulation. For example to simulate a fog case the observations based on the studies of Mazoyer et al. (2022) or Dupont et al. (2018) would be valuable. 2- Performing Meso-NH simulations using our new parameterizations, in cloudy conditions, by the chose of the DSD details from last step. 3- Evaluating the performance of the previsions of surface irradiance against observations to assess the potential improvements.

Another recommended practice for future studies would be to consider new microphysical mechanism to have the DSD shape as a third prognostic value of the model. This can be fulfilled in LIMA turning it to a 3-moment microphysics scheme. Then by the use of our new parameterization, in each time-step, this prognosticated value would be passed to the radiative model.

The consistency of the DSD shape in the SSPs parameterization, the estimation of r_{eff} and the microphysics pave the way for further couplings between the radiative scheme ecRad and the host atmospheric model. As Di Giuseppe and Tompkins (2015) manifests, the wind shear can effect considerably the overlapping of the clouds by replacing a segment of the cloud. Accounting for the wind shear parameters from e.g. Meso-NH in the cloud overlap parameterization of ecRad is an interesting subject for further studies.

Finally, it is worth noting that the aerosols are tightly related to the DSD shape and the number concentration of clouds particles (Martin et al., 1994; Igel and van den Heever, 2017), two quantities that modulate the radiative forcing of clouds as was highlighted in this thesis. The effects of aerosols on the radiative forcing of clouds is known as aerosols indirect effect, or Twomey effect Twomey (1974). We speculate that coupling LIMA and our parameterizations can also improve the study of the aerosols indirect effects in the climate studies.

Conclusions et perspectives

Dans les études sur le climat, l'estimation de l'effet radiatif des nuages diffère considérablement entre d'un modèle de circulation générale (GCM) à l'autre. Par ailleurs, dans les modèles de prévision numérique du temps, les prévisions de rayonnement solaire en surface en conditions nuageuses sont entachées d'erreurs. Cela est dû, dans une certaine mesure, au fait que les nuages ne sont pas prévus au bon endroit et au bon moment. Cependant, les erreurs peuvent également provenir des propriétés radiatives complexes et très variables des nuages, qui ne peuvent être résolues au niveau du point de grille d'un modèle atmosphérique. Ceci inclut toutes les hypothèses radiatives liées à : la distribution sous-maille de l'eau ou de la glace dans un nuage, le recouvrement entre les couches nuageuses, l'hétérogénéité horizontale de la fraction nuageuse, l'estimation des propriétés optiques des nuages. Dans cette thèse, nous nous sommes concentrés sur la paramétrisation des propriétés optiques des nuages liquides, qui n'a pas été revisitée depuis une vingtaine d'années. L'accent est mis sur le spectre solaire (SW), en raison de l'importance du forçage radiatif des nuages dans le SW, de sa plus grande sensibilité à la microphysique des nuages et aux hypothèses radiatives, et de sa plus grande contribution à l'écart entre les modèles par rapport au spectre infrarouge (LW).

Les interactions entre les nuages et le rayonnement ont lieu à l'échelle des gouttelettes. La quantité de rayonnement absorbée et diffusée par la gouttelette est quantifiée par ses propriétés de diffusion simple (SSP). Ces propriétés dépendent fortement de la taille de la gouttelette et de la longueur d'onde de la lumière incidente. Cependant, cette dépendance ne peut pas être prise en compte à l'échelle de la grille du modèle. Pour remédier à ce problème, les modèles atmosphériques reposent sur des paramétrisations qui estiment les SSPs en suivant trois étapes : 1- Pour une longueur d'onde donnée, les SSP moyennes sont calculées pour une distribution de taille de gouttelettes (DSD), en tenant compte du rayon effectif (r_{eff}) et sur la base d'une hypothèse sur la forme de la DSD. 2- Ces SSPs sont ensuite moyennées sur les bandes spectrales du modèle radiatif. 3- Ces 2 étapes sont répétées pour une gamme de r_{eff} , afin d'ajuster une fonction analytique aux résultats, ce qui conduit à des formulations compactes des SSPs en termes de r_{eff} pour chaque bande spectrale. Avant ces deux étapes, les r_{eff} sont généralement dérivés de LWC et de N . Le calcul de r_{eff} nécessite également de supposer une forme de DSD, à travers le paramètre k , connu sous le nom de coefficient de rayon effectif, qui est la racine cubique du ratio entre rayon volumique moyen des gouttelettes et r_{eff} (Martin et al., 1994). La paramétrisation des propriétés optiques implique au final la paramétrisation des SSPs et l'estimation de r_{eff} . Il est important de mentionner que les DSD dans les deux étapes peuvent ne pas correspondre. Une autre hypothèse sur la forme de la DSD est faite dans le schéma microphysique, dont dépend le pronostic de LWC. En plus de ces incohérences éventuelles de la forme de la DSD à différents niveaux, la méthode largement utilisée qui consiste à moyennner linéairement les SSPs sur les bandes spectrales, alors que les SSPs peuvent varier de manière non linéaire, introduit un défi supplémentaire pour la paramétrisation des propriétés optiques.

L'objectif de cette thèse était donc d'étudier l'incertitude des flux radiatifs atmosphériques simulés liée à la forme de la DSD et à la méthode de moyennage spectral utilisée dans la paramétrisation des propriétés optiques. Dans cette optique, de nouvelles paramétrisations ont été développées, qui tiennent explicitement compte de la forme de la DSD. De plus, les nouvelles paramétrisations incluent plusieurs stratégies de moyennage spectral. En outre, nous avons amélioré la méthode d'ajustement afin de bien représenter les caractéristiques oscillatoires des SSPs obtenues pour des rayons effectifs inférieurs à $5 \mu\text{m}$, qui ne sont pas bien représentées dans la paramétrisation la plus récente disponible dans ecRad, SOCRATES Manners (2015). Un autre avantage de cette dernière modification est l'extension du domaine de validité de r_{eff} jusqu'à $1 \mu\text{m}$.

Dans la première partie de la thèse, l'accent a été mis sur le choix de la forme de la DSD dans les SSPs et l'estimation de r_{eff} ainsi que sur le choix des méthodes de moyennage spectral. Les nouvelles paramétrisations ont été implémentées dans ecRad. Ensuite, des simulations de transfert radiatif hors ligne ont été effectuées sur divers profils 1D et sorties de GCM, en choisissant différentes formes de DSD et méthodes de moyennage spectral. Les expériences sur le cas idéal ont porté sur des nuages présentant diverses valeurs de LWC et de N , verticalement uniformes. Les cas réels comprenaient des sorties de 4 simulations LES de cas de brouillard, de stratocumulus, de cumulus et de congestus, moyennées horizontalement et présentant des profils réalistes de LWC non uniformes, contrairement aux nuages du cas idéal. Les différences de flux entre les simulations associées à deux formes de DSD correspondant aux 5^{ème} et 95^{ème} percentiles des valeurs de forme de DSD rapportées dans Miles et al. (2000), ont été interprétées comme l'incertitude liée au DSD.

Nos résultats pour les nuages du cas idéal ont révélé que les incertitudes dans les flux transmis et réfléchis atteignent jusqu'à 20 et 16% respectivement, lorsque le LWP devient faible. Toutefois, ces résultats sont limités aux cas où la valeur de N est comprise entre 80 et 400 cm^{-3} . Les résultats des cas réels révèlent que des nuages ayant un LWP similaire peuvent présenter des incertitudes différentes. Cela provient du fait que le LWC est distribué de manière hétérogène dans la couche nuageuse dans les cas réels, et la distribution verticale détaillée est essentielle pour déterminer l'incertitude. Dans tous les cas, la méthode choisie pour la moyenne spectrale impacte plus l'absorption du nuage que la transmittance et la réflectance.

L'application de notre paramétrisation sur les sorties du CGM CNRM-CM6.1 a montré que l'incertitude de l'effet radiatif SW des nuages (CRE) au sommet de l'atmosphère (TOA) liée à la forme de la DSD peut atteindre 15 W m^{-2} dans les Tropiques, où les nuages liquides de basse altitude sont omniprésents. En moyenne globale l'incertitude sur l'effet radiatif SW des nuages est d'environ 6.2 W m^{-2} , ce qui représente environ 13 % de la valeur de référence observée. Cette incertitude est principalement due à l'incertitude liée à r_{eff} , dont environ 10 % sont compensés par l'incertitude liée aux SSPs. La contribution des SSPs à l'incertitude sur le CRE est ainsi de $-1,6 \text{ W m}^{-2}$.

La deuxième partie de cette thèse s'est concentrée sur la mise en cohérence de la forme de la DSD entre les propriétés optiques utilisées dans le code radiatif et le schéma microphysique du modèle atmosphérique. A cet effet la version améliorée d'ecRad intégrant nos nouvelles paramétrisations a été implémentée dans le modèle atmosphérique Meso-NH. Des simulations 1D du cas de stratocumulus *FIRE*, caractérisé par un cycle diurne marqué, ont été réalisées en s'assurant que la même forme de DSD est supposée dans les deux étapes de la paramétrisation

des propriétés optiques et dans le schéma microphysique LIMA. L'objectif était d'étudier les éventuelles rétroactions résultant des interactions entre l'incertitude liée à la DSD et les autres composantes du modèle atmosphérique.

Les résultats de ces simulations 1D ont mis en évidence que l'incertitude liée à r_{eff} est la principale source de différences entre les simulations utilisant des DSD distinctes, en accord avec les simulations hors ligne. De plus, il a été démontré que l'impact de l'incertitude liée à r_{eff} provenait en grande partie de différences entre les SSPs dans le LW. Par conséquent, pour le reste des simulations, nous avons exclu cet effet en fixant le r_{eff} utilisé pour les propriétés optiques dans le LW. Nous obtenons quantitativement les mêmes différences entre deux formes distinctes de DSD que dans les tests hors ligne. Ceci est valable jusqu'à un pas de temps où aucune différence notable n'est détectée dans les profils LWC, avant le lever du soleil. Après le lever du soleil, la forme de la DSD affecte progressivement les profils de LWC et de N ainsi que le taux de refroidissement dans le LW. Comme le calcul de r_{eff} dépend de N et de LWC, leur modification va générer une rétroaction sur la paramétrisation des propriétés optiques, et par conséquent sur le rayonnement. Les mécanismes par lesquels ces effets indirects se mettent en place ne sont pas triviaux et mériteraient une étude plus approfondie.

Les simulations dans lesquelles la forme de la DSD affecte également les SSPs dans le LW ont indiqué des effets plus importants sur le LWC, le refroidissement LW et les profils de N . Cela suggère d'étendre nos paramétrisations optiques SW au LW. En outre, nous nous sommes limités aux nuages liquides. Pour pouvoir explorer d'autres conditions nuageuses telles que les nuages de glace ou de phase mixte, il serait pertinent d'étendre la méthodologie afin de développer de nouvelles paramétrisations pour les nuages de glace.

Concernant les simulations d'irradiance, nous donnons des recommandations pour une étude future : 1- Choisir la DSD en s'appuyant sur les études existantes (Brenguier et al., 2011; Tas et al., 2015; Wang et al., 2021), de manière approprié au cas d'étude. Par exemple pour simuler un cas de brouillard, les observations basées sur les études de Mazoyer et al. (2022) ou Dupont et al. (2018) seraient pertinentes. 2- Effectuer des simulations Mésos-NH en utilisant nos nouvelles paramétrisations correspondant à la DSD choisie à l'étape précédente. 3- Évaluer la performance des prévisions de rayonnement à la surface par rapport aux observations pour évaluer les éventuelles améliorations.

Une autre piste pour les études futures serait d'envisager un nouveau mécanisme microphysique pour que la forme du DSD soit une troisième valeur pronostique du modèle. Ceci peut être réalisé dans LIMA en le transformant en un schéma microphysique à 3 moments. Ensuite, par l'utilisation de notre nouvelle paramétrisation, à chaque pas de temps, cette valeur pronostiquée serait transférée au modèle radiatif.

La cohérence de la forme de la DSD dans la paramétrisation des SSPs, l'estimation de r_{eff} et la microphysique, ouvrent la voie à d'autres couplages entre le schéma radiatif ecRad et le modèle atmosphérique hôte. Comme le montre Di Giuseppe and Tompkins (2015), le cisaillement du vent peut affecter considérablement le recouvrement des nuages en remplaçant un segment du nuage. La prise en compte des paramètres de cisaillement du vent provenant par exemple de Meso-NH dans la paramétrisation du chevauchement des nuages d'ecRad est un sujet intéressant pour des études ultérieures.

Enfin, il faut souligner que les aérosols sont étroitement liés à la forme du DSD et à la concentration en nombre de particules de nuages (Martin et al., 1994; Igel and van den Heever, 2017), deux quantités qui modulent le forçage radiatif des nuages comme cela a été mis en évidence dans cette thèse. Les effets des aérosols sur le forçage radiatif des nuages sont connus sous le nom d'effet indirect des aérosols, ou effet Twomey Twomey (1974). Nous pensons que le couplage de LIMA et de nos paramétrisations peut également améliorer l'étude des effets indirects des aérosols dans les études climatiques.

Bibliography

- Ackerman, A. S., Hobbs, P. V., and Toon, O. B. (1995). A model for particle microphysics, turbulent mixing, and radiative transfer in the stratocumulus-topped marine boundary layer and comparisons with measurements. *Journal of Atmospheric Sciences*, 52(8):1204 – 1236.
- Ahlgrimm, M., Forbes, R. M., Hogan, R. J., and Sandu, I. (2018). Understanding Global Model Systematic Shortwave Radiation Errors in Subtropical Marine Boundary Layer Cloud Regimes. *Journal of Advances in Modeling Earth Systems*, 10(8).
- Albrecht, B. A., Randall, D. A., and Nicholls, S. (1988). Observations of marine stratocumulus clouds during fire. *Bulletin of the American Meteorological Society*, 69(6):618 – 626.
- Anderson, G. P., Clough, S. A., Kneizys, F., Chetwynd, J. H., and Shettle, E. P. (1986). Afl atmospheric constituent profiles (0.120 km). Technical report, Air Force Geophysics Lab Hanscom AFB MA.
- Aquino, J. and Varela, J. (2005). Two stream approximation to radiative transfer equation: An alternative method of solution. *Revista Mexicana De Fisica*, 51:82–86.
- Bae, S. Y., Hong, S.-Y., and Lim, K.-S. S. (2016). Coupling WRF double-moment 6-class microphysics schemes to RRTMG radiation scheme in weather research forecasting model. *Advances in Meteorology*, 2016.
- Bohren, C. F. and Clothiaux, E. (2006). *Fundamentals of atmospheric radiation*, volume 25. Wiley Online Library.
- Bony, S., Musat, I., Li, B., Webb, M., Senior, C., Sexton, D., Ingram, W., Williams, K., Ringer, M., McAvaney, B., Colman, R., Soden, B., Gudgel, R., Knutson, T., Emori, S., Ogura, T., Tsushima, Y., Andronova, N., and Taylor, K. (2006). On the contribution of local feedback mechanisms to the range of climate sensitivity in two GCM ensembles. *Climate Dynamics*, 27.
- Bott, A., Sievers, U., and Zdunkowski, W. (1990). A radiation fog model with a detailed treatment of the interaction between radiative transfer and fog microphysics. *Journal of Atmospheric Sciences*, 47(18):2153 – 2166.
- Brenguier, J. L., Burnet, F., and Geoffroy, O. (2011). Cloud optical thickness and liquid water path—does the k coefficient vary with droplet concentration? *Atmospheric Chemistry and Physics*, 11(18).
- Brient, F., Couvreux, F., Villefranque, N., Rio, C., and Honnert, R. (2019). Object-Oriented Identification of Coherent Structures in Large Eddy Simulations: Importance of Downdrafts in Stratocumulus. *Geophysical Research Letters*, 46(5).
- Cahalan, R. F., Ridgway, W., Wiscombe, W. J., Bell, T. L., and Snider, J. B. (1994a). The albedo of fractal stratocumulus clouds. *Journal of Atmospheric Sciences*, 51(16):2434 – 2455.

- Cahalan, R. F., Ridgway, W., Wiscombe, W. J., and Gollmer, S. (1994b). Independent pixel and monte carlo estimates of stratocumulus albedo. *Journal of Atmospheric Sciences*, 51(24):3776–3790.
- Carlin, B., Fu, Q., Lohmann, U., Mace, G. G., Sassen, K., and Comstock, J. M. (2002). High-cloud horizontal inhomogeneity and solar albedo bias. *Journal of Climate*, 15(17):2321 – 2339.
- Carrier, L. W., Cato, G. A., and Von Essen, K. J. (1967). The backscattering and extinction of visible and infrared radiation by selected major cloud models. *Applied Optics*, 6(7):1209–1216.
- Choudhury, B. J. (1981). Radiative properties of snow for clear sky solar radiation. *Cold Regions Science and Technology*, 4:103–120.
- Cohard, J.-M. and Pinty, J.-P. (2000). A comprehensive two-moment warm microphysical bulk scheme. i: Description and tests. *Quarterly Journal of the Royal Meteorological Society*, 126(566):1815–1842.
- Cohard, J.-M., Pinty, J.-P., and Bedos, C. (1998). Extending twomey’s analytical estimate of nucleated cloud droplet concentrations from ccn spectra. *Journal of the Atmospheric Sciences*, 55(22):3348 – 3357.
- Cros, S., Liandrat, O., Sébastien, N., and Schmutz, N. (2014). Extracting cloud motion vectors from satellite images for solar power forecasting. In *2014 IEEE Geoscience and Remote Sensing Symposium*, pages 4123–4126.
- Cuxart, J., Bougeault, P., and Redelsperger, J.-L. (2000). A turbulence scheme allowing for mesoscale and large-eddy simulations. *Quarterly Journal of the Royal Meteorological Society*, 126(562):1–30.
- de Lozar, A. and Muessle, L. (2016). Long-resident droplets at the stratocumulus top. *Atmospheric Chemistry and Physics*, 16(10):6563–6576.
- Di Giuseppe, F. and Tompkins, A. M. (2015). Generalizing cloud overlap treatment to include the effect of wind shear. *Journal of the Atmospheric Sciences*, 72(8).
- Diagne, M., David, M., Lauret, P., Boland, J., and Schmutz, N. (2013). Review of solar irradiance forecasting methods and a proposition for small-scale insular grids. *Renewable and Sustainable Energy Reviews*, 27:65–76.
- Driemel, A., Augustine, J., Behrens, K., Colle, S., Cox, C., Cuevas-Agulló, E., Denn, F. M., Duprat, T., Fukuda, M., Grobe, H., Haeffelin, M., Hodges, G., Hyett, N., Ijima, O., Kallis, A., Knap, W., Kustov, V., Long, C. N., Longenecker, D., Lupi, A., Maturilli, M., Mimouni, M., Ntsangwane, L., Ogihara, H., Olano, X., Olfes, M., Omori, M., Passamani, L., Pereira, E. B., Schmithüsen, H., Schumacher, S., Sieger, R., Tamlyn, J., Vogt, R., Vuilleumier, L., Xia, X., Ohmura, A., and König-Langlo, G. (2018). Baseline surface radiation network (bsrn): structure and data description (1992–2017). *Earth System Science Data*, 10(3):1491–1501.
- Dupont, J.-C., Haeffelin, M., Wærsted, E., Delanoë, J., Renard, J.-B., Preissler, J., and O’Dowd, C. (2018). Evaluation of Fog and Low Stratus Cloud Microphysical Properties Derived from In Situ Sensor, Cloud Radar and SYRSOC Algorithm. *Atmosphere*, 9(5):169.
- Duynkerke, P. G., de Roode, S. R., van Zanten, M. C., Calvo, J., Cuxart, J., Cheinet, S., Chlond, A., Grenier, H., Jonker, P. J., Köhler, M., Lenderink, G., Lewellen, D., Lappen, C. L., Lock, A. P., Moeng, C. H., Müller, F., Olmeda, D., Piriou, J. M., Sánchez, E., and Sednev, I. (2004). Observations and numerical simulations of the diurnal cycle of the EUROCS stratocumulus case. *Quarterly Journal of the Royal Meteorological Society*, 130 C(604).

- Edwards, J. M. and Slingo, A. (1996). Studies with a flexible new radiation code. I: Choosing a configuration for a large-scale model. *Quarterly Journal of the Royal Meteorological Society*, 122(531):689–719.
- Engström, A., Bender, F. A., and Karlsson, J. (2014). Improved representation of marine stratocumulus cloud shortwave radiative properties in the CMIP5 climate models. *Journal of Climate*, 27(16).
- Espinoza Jr, R. C. (1996). Parameterization of solar near-infrared radiative properties of cloudy layers. *Journal of the atmospheric sciences*, 53(11):1559–1568.
- Fiedler, S., Stevens, B., Gidden, M., Smith, S. J., Riahi, K., and van Vuuren, D. (2019). First forcing estimates from the future cmip6 scenarios of anthropogenic aerosol optical properties and an associated twomey effect. *Geoscientific Model Development*, 12(3):989–1007.
- Fouquart, Y. and Bonnel, B. (1980). Computations of solar heating of the earth’s atmosphere: A new parameterization. *Beitr. Phys. Atmos.*, 53.
- Geleyn, J.-F. and Hollingsworth, A. (1979). An economical analytical method for the computation of the interaction between scattering and line absorption of radiation. *BEITR. PHYS. ATMOSPHER.*, 52(1):1–16.
- Geoffroy, O., Brenguier, J.-L., and Sandu, I. (2008). Relationship between drizzle rate, liquid water path and droplet concentration at the scale of a stratocumulus cloud system. *Atmospheric Chemistry and Physics*, 8(16):4641–4654.
- Gottelman, A. and Sherwood, S. (2016). Processes responsible for cloud feedback. *Current Climate Change Reports*, 2.
- Gordon, I., Rothman, L., Hargreaves, R., Hashemi, R., Karlovets, E., Skinner, F., Conway, E., Hill, C., Kochanov, R., Tan, Y., Wcisło, P., Finenko, A., Nelson, K., Bernath, P., Birk, M., Boudon, V., Campargue, A., Chance, K., Coustenis, A., Drouin, B., Flaud, J., Gamache, R., Hodges, J., Jacquemart, D., Mlawer, E., Nikitin, A., Perevalov, V., Rotger, M., Tennyson, J., Toon, G., Tran, H., Tyuterev, V., Adkins, E., Baker, A., Barbe, A., Canè, E., Császár, A., Dudaryonok, A., Egorov, O., Fleisher, A., Fleurbaey, H., Foltynowicz, A., Furtenbacher, T., Harrison, J., Hartmann, J., Horne- man, V., Huang, X., Karman, T., Karns, J., Kass, S., Kleiner, I., Kofman, V., Kwabia-Tchana, F., Lavrentieva, N., Lee, T., Long, D., Lukashovskaya, A., Lyulin, O., Makhnev, V., Matt, W., Massie, S., Melosso, M., Mikhailenko, S., Mondelain, D., Müller, H., Naumenko, O., Perrin, A., Polyansky, O., Raddaoui, E., Raston, P., Reed, Z., Rey, M., Richard, C., Tóbiás, R., Sadiek, I., Schwenke, D., Starikova, E., Sung, K., Tamassia, F., Tashkun, S., Vander Auwera, J., Vasilenko, I., Vigasin, A., Villanueva, G., Vispoel, B., Wagner, G., Yachmenev, A., and Yurchenko, S. (2022). The hitran2020 molecular spectroscopic database. *Journal of Quantitative Spectroscopy and Radiative Transfer*, 277:107949.
- Hanna, R., Kleissl, J., Nottrott, A., and Ferry, M. (2014). Energy dispatch schedule optimization for demand charge reduction using a photovoltaic-battery storage system with solar forecasting. *Solar Energy*, 103:269–287.
- Harshvardhan and King, M. D. (1993). Comparative accuracy of diffuse radiative properties computed using selected multiple scattering approximations. *Journal of Atmospheric Sciences*, 50(2):247 – 259.
- Harshvardhan and Randall, D. A. (1985). Comments on “the parameterization of radiation for numerical weather prediction and climate models”. *Monthly Weather Review*, 113(10):1832 – 1833.

- Hess, M., Koepke, P., and Schult, I. (1998). Optical properties of aerosols and clouds: The software package opac. *Bulletin of the American Meteorological Society*, 79(5):831 – 844.
- Hogan, R. J. and Bozzo, A. (2018). A flexible and efficient radiation scheme for the ECMWF model. *Journal of Advances in Modeling Earth Systems*, 10(8):1990–2008.
- Hogan, R. J. and Illingworth, A. J. (2000). Deriving cloud overlap statistics from radar. *Quarterly Journal of the Royal Meteorological Society*, 126(569).
- Hogan, R. J., Schäfer, S. A. K., Klinger, C., Chiu, J. C., and Mayer, B. (2016). Representing 3-D cloud radiation effects in two-stream schemes: 2. Matrix formulation and broadband evaluation. *Journal of Geophysical Research: Atmospheres*, 121(14):8583–8599.
- Hogan, R. J., Schäfer, S. A. K., Klinger, C., Chiu, J. C., and Mayer, B. (2016). Representing 3-D cloud radiation effects in two-stream schemes: 2. Matrix formulation and broadband evaluation. *Journal of Geophysical Research (Atmospheres)*, 121(14):8583–8599.
- Hu, Y. and Stamnes, K. (2000). Climate sensitivity to cloud optical properties. *Tellus, Series B: Chemical and Physical Meteorology*, 52(1).
- Hu, Y. X. and Stamnes, K. (1993). An accurate parameterization of the radiative properties of water clouds suitable for use in climate models. *Journal of climate*, 6(4):728–742.
- Huang, G., Li, Z., Li, X., Liang, S., Yang, K., Wang, D., and Zhang, Y. (2019). Estimating surface solar irradiance from satellites: Past, present, and future perspectives. *Remote Sensing of Environment*, 233:111371.
- Igel, A. L. and van den Heever, S. C. (2017). The importance of the shape of cloud droplet size distributions in shallow cumulus clouds. Part II: Bulk microphysics simulations. *Journal of the Atmospheric Sciences*, 74(1):259–273.
- Joseph, J. H., Wiscombe, W. J., and Weinman, J. A. (1976). The delta-Eddington approximation for radiative flux transfer. *Journal of the Atmospheric Sciences*, 33(12):2452–2459.
- Khairoutdinov, M. and Kogan, Y. (2000). A new cloud physics parameterization in a large-eddy simulation model of marine stratocumulus. *Monthly Weather Review*, 128(1):229 – 243.
- Kim, S., Jeong, H., Park, J. Y., Baek, S. Y., Lee, A., and Choi, S.-H. (2019). Innovative flat-plate solar collector (fpc) with coloured water flowing through a transparent tube. *RSC Adv.*, 9:24192–24202.
- Klinger, C., Feingold, G., and Yamaguchi, T. (2019). Cloud droplet growth in shallow cumulus clouds considering 1-d and 3-d thermal radiative effects. *Atmospheric Chemistry and Physics*, 19(9):6295–6313.
- Kokhanovsky, A. (2004). Optical properties of terrestrial clouds. *Earth-Science Reviews*, 64(3):189–241.
- Krisna, T. C., Wendisch, M., Ehrlich, A., Jäkel, E., Werner, F., Weigel, R., Borrmann, S., Mahnke, C., Pöschl, U., Andreae, M. O., Voigt, C., and Machado, L. A. T. (2018). Comparing airborne and satellite retrievals of cloud optical thickness and particle effective radius using a spectral radiance ratio technique: two case studies for cirrus and deep convective clouds. *Atmospheric Chemistry and Physics*, 18(7):4439–4462.

- Lac, C., Chaboureau, J. P., Masson, V., Pinty, J. P., Tulet, P., Escobar, J., Leriche, M., Barthe, C., Aouizerats, B., Augros, C., Aumond, P., Auguste, F., Bechtold, P., Berthet, S., Bielli, S., Bosseur, F., Caumont, O., Cohard, J. M., Colin, J., Couvreux, F., Cuxart, J., Delautier, G., Dauhut, T., Ducrocq, V., Filippi, J. B., Gazen, D., Geoffroy, O., Gheusi, F., Honnert, R., Lafore, J. P., Brossier, C. L., Libois, Q., Lunet, T., Mari, C., Maric, T., Mascart, P., Mogé, M., Molinié, G., Nuissier, O., Pantillon, F., Peyrillé, P., Pergaud, J., Perraud, E., Pianezze, J., Redelsperger, J. L., Ricard, D., Richard, E., Riette, S., Rodier, Q., Schoetter, R., Seyfried, L., Stein, J., Suhre, K., Taufour, M., Thouron, O., Turner, S., Verrelle, A., Vié, B., Visentin, F., Vionnet, V., and Wautelet, P. (2018). Overview of the Meso-NH model version 5.4 and its applications. *Geoscientific Model Development*, 11(5).
- Lacis, A. A. and Hansen, J. (1974). A parameterization for the absorption of solar radiation in the earth's atmosphere. *Journal of Atmospheric Sciences*, 31(1):118 – 133.
- Lacis, A. A. and Oinas, V. (1991). A description of the correlated k distribution method for modeling nongray gaseous absorption, thermal emission, and multiple scattering in vertically inhomogeneous atmospheres. *Journal of Geophysical Research: Atmospheres*, 96(D5):9027–9063.
- Lapo, K. E., Hinkelman, L. M., Sumargo, E., Hughes, M., and Lundquist, J. D. (2017). A critical evaluation of modeled solar irradiance over california for hydrologic and land surface modeling. *Journal of Geophysical Research: Atmospheres*, 122(1):299–317.
- Lauret, P., Voyant, C., Soubdhan, T., David, M., and Poggi, P. (2015). A benchmarking of machine learning techniques for solar radiation forecasting in an insular context. *Solar Energy*, 112:446–457.
- Letu, H., Shi, J., Li, M., Wang, T., Shang, H., Lei, Y., Ji, D., Wen, J., Yang, K., and Chen, L. (2020). A review of the estimation of downward surface shortwave radiation based on satellite data: Methods, progress and problems. *Science China Earth Sciences*, 63.
- Libois, Q. (2014). *Evolution des propriétés physiques de neige de surface sur le plateau Antarctique. Observations et modélisation du transfert radiatif et du métamorphisme*. Theses, Université de Grenoble.
- Liu, Y., Daum, P. H., Guo, H., and Peng, Y. (2008). Dispersion bias, dispersion effect, and the aerosol–cloud conundrum. *Environmental Research Letters*, 3(4):45021.
- Loeb, N. G., Doelling, D. R., Wang, H., Su, W., Nguyen, C., Corbett, J. G., Liang, L., Mitrescu, C., Rose, F. G., and Kato, S. (2018). Clouds and the earth's radiant energy system (CERES) energy balanced and filled (EBAF) top-of-atmosphere (TOA) edition-4.0 data product. *Journal of Climate*, 31(2):895–918.
- Lu, P., Zhang, H., and Li, J. (2011). Correlated k-distribution treatment of cloud optical properties and related radiative impact. *Journal of the atmospheric sciences*, 68(11):2671–2688.
- Madeleine, J. B., Hourdin, F., Grandpeix, J. Y., Rio, C., Dufresne, J. L., Vignon, E., Boucher, O., Konsta, D., Cheruy, F., Musat, I., Idelkadi, A., Fairhead, L., Millour, E., Lefebvre, M. P., Mellul, L., Rochetin, N., Lemonnier, F., Touzé-Peiffer, L., and Bonazzola, M. (2020). Improved Representation of Clouds in the Atmospheric Component LMDZ6A of the IPSL-CM6A Earth System Model. *Journal of Advances in Modeling Earth Systems*, 12(10).
- Manners, J. (2015). Socrates technical guide suite of community radiative transfer codes based on edwards and slingo. In *Tech. Rep., Met Office, FitzRoy Rd, Exeter EX1 3PB*.
- Martin, G. M., Johnson, D. W., and Spice, A. (1994). The measurement and parameterization of effective radius of droplets in warm stratocumulus clouds. *Journal of the Atmospheric Sciences*, 51(13):1823–1842.

- Masek, J., Geleyn, J., Brozková, R., Giot, O., Achom, H. O., and Kuma, P. (2016). Single interval shortwave radiation scheme with parameterized optical saturation and spectral overlaps. *Quarterly Journal of the Royal Meteorological Society*, 142:304–326.
- Mazoyer, M., Burnet, F., and Denjean, C. (2022). Experimental study on the evolution of droplets size distribution during the fog life cycle. *Atmospheric Chemistry and Physics Discussions*, 2022:1–28.
- Meador, W. E. and Weaver, W. R. (1980). Two-stream approximations to radiative transfer in planetary atmospheres: A unified description of existing methods and a new improvement. *Journal of the atmospheric sciences*, 37(3):630–643.
- Mihalas, D. and Mihalas, B. W. (1984). *Foundations of radiation hydrodynamics*.
- Miles, N. L., Verlinde, J., and Clothiaux, E. E. (2000). Cloud droplet size distributions in low-level stratiform clouds. *Journal of the atmospheric sciences*, 57(2):295–311.
- Mishchenko, M. I., Dlugach, J. M., Yanovitskij, E. G., and Zakharova, N. T. (1999). Bidirectional reflectance of flat, optically thick particulate layers: an efficient radiative transfer solution and applications to snow and soil surfaces. *Journal of Quantitative Spectroscopy and Radiative Transfer*, 63(2-6):409–432.
- Mishchenko, M. I., Travis, L. D., and Lacis, A. A. (2002). *Scattering, absorption, and emission of light by small particles*. Cambridge university press.
- Mlawer, E. J., Taubman, S. J., Brown, P. D., Iacono, M. J., and Clough, S. A. (1997). Radiative transfer for inhomogeneous atmospheres: RRTM, a validated correlated-k model for the longwave. *Journal of Geophysical Research: Atmospheres*, 102(D14):16663–16682.
- Montornes, A., Codina, B., and Zack, J. (2015). A discussion about the role of shortwave schemes on real wrf-arw simulations. two case studies: cloudless and cloudy sky. *TETHYS-JOURNAL OF MEDITERRANEAN METEOROLOGY & CLIMATOLOGY*, (12):13–31.
- Morcrette, J.-J. (1991). Radiation and cloud radiative properties in the european centre for medium range weather forecasts forecasting system. *Journal of Geophysical Research: Atmospheres*, 96(D5):9121–9132.
- Morcrette, J. J., Barker, H. W., Cole, J. N., Iacono, M. J., and Pincus, R. (2008). Impact of a new radiation package, McRad, in the ECMWF integrated forecasting system. *Monthly Weather Review*, 136(12).
- Morcrette, J. J., Smith, L., and Fouquart, Y. (1986). Pressure and temperature dependence of the absorption in longwave radiation parametrizations. *Beiträge zur Physik der Atmosphäre*, 59(4):455–469.
- Nam, C., Bony, S., Dufresne, J.-L., and Chepfer, H. (2012). The ‘too few, too bright’ tropical low-cloud problem in CMIP5 models. *Geophysical Research Letters*, 39(21).
- Pattelli, L. (2018). *Imaging light transport at the femtosecond scale: A walk on the wild side of diffusion*. Published by Firenze University Press.
- Pergaud, J., Masson, V., Malardel, S., and Couvreux, F. (2009). A parameterization of dry thermals and shallow cumuli for mesoscale numerical weather prediction. *Boundary-layer meteorology*, 132(1):83–106.

- Pincus, R., Barker, H. W., and Morcrette, J.-J. (2003). A fast, flexible, approximate technique for computing radiative transfer in inhomogeneous cloud fields. *Journal of Geophysical Research: Atmospheres*, 108(D13).
- Pinty, J.-P. and Jabouille, P. (1998). A mixed-phase cloud parameterization for use in a mesoscale non-hydrostatic model: simulations of a squall line and of orographic precipitations. In *Conference on cloud Physics*, pages 217–220, Everett, Washington.
- Quéno, L., Karbou, F., Vionnet, V., and Dombrowski-Etchevers, I. (2020). Satellite-derived products of solar and longwave irradiances used for snowpack modelling in mountainous terrain. *Hydrology and Earth System Sciences*, 24(4):2083–2104.
- Ramanathan, V., Cess, R. D., Harrison, E. F., Minnis, P., Barkstrom, B. R., Ahmad, E., and Hartmann, D. (1989). Cloud-radiative forcing and climate: Results from the earth radiation budget experiment. *Science*, 243(4887):57–63.
- Ritter, B. and Geleyn, J.-F. (1992). A comprehensive radiation scheme for numerical weather prediction models with potential applications in climate simulations. *Monthly weather review*, 120(2):303–325.
- Rockel, B., Raschke, E., and Weyres, B. (1991). A parameterization of broad band radiative transfer properties of water, ice, and mixed clouds. *Beiträge zur Physik der Atmosphäre*, 64:1–12.
- Roehrig, R., Beau, I., Saint-Martin, D., Alias, A., Decharme, B., Guérémy, J. F., Voldoire, A., Abdel-Lathif, A. Y., Bazile, E., Belamari, S., Blein, S., Bouniol, D., Bouteloup, Y., Cattiaux, J., Chauvin, F., Chevallier, M., Colin, J., Douville, H., Marquet, P., Michou, M., Nabat, P., Oudar, T., Peyrillé, P., Piriou, J. M., Salas y Mélia, D., Séférian, R., and Sénési, S. (2020). The CNRM Global Atmosphere Model ARPEGE-Climat 6.3: Description and Evaluation. *Journal of Advances in Modeling Earth Systems*, 12(7).
- Rontu, L. and Lindfors, A. V. (2018). Comparison of radiation parametrizations within the harmonie-
arome nwp model. *Advances in Science and Research*, 15:81–90.
- Rotstayn, L. D. and Liu, Y. (2003). Sensitivity of the first indirect aerosol effect to an increase of cloud droplet spectral dispersion with droplet number concentration. *Journal of Climate*, 16(21).
- Rotstayn, L. D. and Liu, Y. (2009). Cloud droplet spectral dispersion and the indirect aerosol effect: Comparison of two treatments in a GCM. *Geophysical Research Letters*, 36(10).
- Savijärvi, H. and Räisänen, P. (1998). Long-wave optical properties of water clouds and rain. *Tellus A: Dynamic Meteorology and Oceanography*, 50(1):1–11.
- Seity, Y., Brousseau, P., Malardel, S., Hello, G., B?nard, P., Bouttier, F., Lac, C., and Masson, V. (2011). The arome-france convective-scale operational model. *Monthly Weather Review*, 139(3):976 – 991.
- Shettle, E. P. and Weinman, J. A. (1970). The transfer of solar irradiance through inhomogeneous turbid atmospheres evaluated by eddington’s approximation. *Journal of Atmospheric Sciences*, 27(7):1048 – 1055.
- Shonk, J. K. and Hogan, R. J. (2008). Tripleclouds: An efficient method for representing horizontal cloud inhomogeneity in 1D Radiation schemes by using three regions at each height. *Journal of Climate*, 21(11).

- Sieron, S. B., Clothiaux, E. E., Zhang, F., Lu, Y., and Otkin, J. A. (2017). Comparison of using distribution-specific versus effective radius methods for hydrometeor single-scattering properties for all-sky microwave satellite radiance simulations with different microphysics parameterization schemes. *Journal of Geophysical Research*, 122(13).
- Slingo, A. (1989). A GCM parameterization for the shortwave radiative properties of water clouds. *Journal of the Atmospheric Sciences*, 46(10):1419–1427.
- Slingo, A. and Schrecker, H. M. (1982). On the shortwave radiative properties of stratiform water clouds. *Quarterly Journal of the Royal Meteorological Society*, 108(456):407–426.
- Smith, E. A. and Shi, L. (1992). Surface forcing of the infrared cooling profile over the tibetan plateau. part i: Influence of relative longwave radiative heating at high altitude. *Journal of Atmospheric Sciences*, 49(10):805 – 822.
- Stephens, G. L. (1978). Radiation Profiles in Extended Water Clouds. II: Parameterization Schemes. *Journal of Atmospheric Sciences*, 35:2123–2132.
- Stephens, G. L. (1979). Optical properties of eight water cloud types. *Division of Atmospheric Physics technical paper Series Volume Id*, (36).
- Stevens, B., Giorgetta, M., Esch, M., Mauritsen, T., Crueger, T., Rast, S., Salzmann, M., Schmidt, H., Bader, J., Block, K., et al. (2013). Atmospheric component of the mpi-m earth system model: Echem6. *Journal of Advances in Modeling Earth Systems*, 5(2):146–172.
- Sukhodolov, T., Rozanov, E., Ball, W. T., Bais, A., Tourpali, K., Shapiro, A. I., Telford, P., Smyshlyaev, S., Fomin, B., Sander, R., Bossay, S., Bekki, S., Marchand, M., Chipperfield, M. P., Dhomse, S., Haigh, J. D., Peter, T., and Schmutz, W. (2016). Evaluation of simulated photolysis rates and their response to solar irradiance variability. *Journal of Geophysical Research: Atmospheres*, 121(10):6066–6084.
- Szczap, F., Isaka, H., Saute, M., Guillemet, B., and Ioltukhovski, A. (2000). Effective radiative properties of bounded cascade nonabsorbing clouds: Definition of the equivalent homogeneous cloud approximation. *Journal of Geophysical Research: Atmospheres*, 105(D16):20617–20633.
- Tas, E., Teller, A., Altaratz, O., Axisa, D., Brient, R., Levin, Z., and Koren, I. (2015). The relative dispersion of cloud droplets: Its robustness with respect to key cloud properties. *Atmospheric Chemistry and Physics*, 15(4).
- Thompson, G., Tewari, M., Ikeda, K., Tessoro, S., Weeks, C., Otkin, J., and Kong, F. (2016). Explicitly-coupled cloud physics and radiation parameterizations and subsequent evaluation in wrf high-resolution convective forecasts. *Atmospheric Research*, 168:92–104.
- Tiedtke, M. (1996). An extension of cloud-radiation parameterization in the ecmwf model: The representation of subgrid-scale variations of optical depth. *Monthly Weather Review*, 124(4):745 – 750.
- Topaloglou, C., Kazadzis, S., Bais, A. F., Blumthaler, M., Schallhart, B., and Balis, D. (2005). NO₂ and HCHO photolysis frequencies from irradiance measurements in Thessaloniki, Greece. *Atmospheric Chemistry and Physics*, 5(6):1645–1653.
- Tulet, P., Crassier, V., Cousin, F., Suhre, K., and Rosset, R. (2005). Orilam, a three-moment lognormal aerosol scheme for mesoscale atmospheric model: Online coupling into the meso-nh-c model and validation on the escompte campaign. *Journal of Geophysical Research: Atmospheres*, 110(D18).

- Tuononen, M., O'Connor, E. J., and Sinclair, V. A. (2019). Evaluating solar radiation forecast uncertainty. *Atmospheric Chemistry and Physics*, 19(3):1985–2000.
- Turner, D. D., Shupe, M. D., and Zwink, A. B. (2018). Characteristic atmospheric radiative heating rate profiles in arctic clouds as observed at barrow, alaska. *Journal of Applied Meteorology and Climatology*, 57(4):953 – 968.
- Twomey, S. (1974). Pollution and the planetary albedo. *Atmospheric Environment (1967)*, 8(12).
- Vaillant de Guélis, T., Chepfer, H., Noel, V., Guzman, R., Dubuisson, P., Winker, D. M., and Kato, S. (2017). The link between outgoing longwave radiation and the altitude at which a spaceborne lidar beam is fully attenuated. *Atmospheric Measurement Techniques*, 10(12):4659–4685.
- Van Weverberg, K., Morcrette, C. J., Petch, J., Klein, S. A., Ma, H.-Y., Zhang, C., Xie, S., Tang, Q., Gustafson Jr, W. I., Qian, Y., Berg, L. K., Liu, Y., Huang, M., Ahlgrimm, M., Forbes, R., Bazile, E., Roehrig, R., Cole, J., Merryfield, W., Lee, W.-S., Cheruy, F., Mellul, L., Wang, Y.-C., Johnson, K., and Thieman, M. M. (2018). Causes: Attribution of surface radiation biases in nwp and climate models near the u.s. southern great plains. *Journal of Geophysical Research: Atmospheres*, 123(7):3612–3644.
- Vaughan, M. A., Powell, K. A., Winker, D. M., Hostetler, C. A., Kuehn, R. E., Hunt, W. H., Getzewich, B. J., Young, S. A., Liu, Z., and McGill, M. J. (2009). Fully automated detection of cloud and aerosol layers in the calipso lidar measurements. *Journal of Atmospheric and Oceanic Technology*, 26(10):2034 – 2050.
- Vial, J., Dufresne, J.-L., and Bony, S. (2013). On the interpretation of inter-model spread in CMIP5 climate sensitivity estimates. *Climate Dynamics*, 41(11-12):3339–3362.
- Vie, B., Pinty, J. P., Berthet, S., and Leriche, M. (2016). LIMA (v1.0): A quasi two-moment microphysical scheme driven by a multimodal population of cloud condensation and ice freezing nuclei. *Geoscientific Model Development*, 9(2).
- Vionnet, V., Dombrowski-Etchevers, I., Lafaysse, M., Qu?no, L., Seity, Y., and Bazile, E. (2016). Numerical weather forecasts at kilometer scale in the french alps: Evaluation and application for snowpack modeling. *Journal of Hydrometeorology*, 17(10):2591 – 2614.
- Voigt, A., Albern, N., Ceppi, P., Grise, K., Li, Y., and Medeiros, B. (2021). Clouds, radiation, and atmospheric circulation in the present-day climate and under climate change. *WIREs Climate Change*, 12(2):e694.
- Wang, M., Peng, Y., Liu, Y., Liu, Y., Xie, X., and Guo, Z. (2020). Understanding Cloud Droplet Spectral Dispersion Effect Using Empirical and Semi-Analytical Parameterizations in NCAR CAM5.3. *Earth and Space Science*, 7(8).
- Wang, Y., Zhao, C., McFarquhar, G. M., Wu, W., Reeves, M., and Li, J. (2021). Dispersion of Droplet Size Distributions in Supercooled Non-precipitating Stratocumulus from Aircraft Observations Obtained during the Southern Ocean Cloud Radiation Aerosol Transport Experimental Study. *Journal of Geophysical Research: Atmospheres*, 126(6).
- Wild, M. (2020). The global energy balance as represented in CMIP6 climate models. *Climate Dynamics*, 55(3-4).
- Wild, M., Hakuba, M. Z., Folini, D., Dörig-Ott, P., Schär, C., Kato, S., and Long, C. N. (2019). The cloud-free global energy balance and inferred cloud radiative effects: an assessment based on direct observations and climate models. *Climate Dynamics*, 52(7-8).

- Wiscombe, W. J. (1977). The Delta-M method: Rapid yet accurate radiative flux calculations for strongly asymmetric phase functions. *Journal of the atmospheric sciences*, 34(9):1408–1422.
- Wiscombe, W. J. (1980). Improved mie scattering algorithms. *Appl. Opt.*, 19(9):1505–1509.
- Wood, R. (2012). Stratocumulus clouds. *Monthly Weather Review*, 140(8):2373–2423.
- Zelinka, M. D., Myers, T. A., McCoy, D. T., Po-Chedley, S., Caldwell, P. M., Ceppi, P., Klein, S. A., and Taylor, K. E. (2020). Causes of Higher Climate Sensitivity in CMIP6 Models. *Geophysical Research Letters*, 47(1).
- Zhao, W., Peng, Y., Wang, B., Yi, B., Lin, Y., and Li, J. (2018). Comparison of three ice cloud optical schemes in climate simulations with community atmospheric model version 5. *Atmospheric research*, 204:37–53.